J. Fluid Mech. (1996), *vol.* 328, *pp.* 345–407

Three-dimensional wake transition

By C. H. K. WILLIAMSON
Mechanical and Aerospace Engineering, Upson Hall, Cornell University, Ithaca, NY 14853, USA

(Received 25 October 1995 and in revised form 16 May 1996)

It is now well-known that the wake transition regime for a circular cylinder involves two modes of small-scale three-dimensional instability (modes A and B), depending on the regime of Reynolds number (Re), although almost no understanding of the physical origins of these instabilities, or indeed their effects on near-wake formation, have hitherto been made clear. We address these questions in this paper. In particular, it is found that the two different modes A and B scale on different physical features of the flow. Mode A has a larger spanwise wavelength of around 3–4 diameters, and scales on the larger physical structure in the flow, namely the primary vortex core. The wavelength for mode A is shown to be the result of an 'elliptic instability' in the near-wake vortex cores. The subsequent nonlinear growth of vortex loops is due to a feedback from one vortex to the next, involving spanwise-periodic deformation of core vorticity, which is then subject to streamwise stretching in the braid regions. This mode gives an out-of-phase streamwise vortex pattern.

In contrast, mode-B instability has a distinctly smaller wavelength (1 diameter) which scales on the smaller physical structure in the flow, the braid shear layer. It is a manifestation of an instability in a region of hyperbolic flow. It is quite distinct from other shear flows, in that it depends on the reverse flow of the bluff-body wake; the presence of a fully formed streamwise vortex system, brought upstream from a previous half-cycle, in proximity to the newly evolving braid shear layer, leads to an in-phase streamwise vortex array, in strong analogy with the 'Mode 1' of Meiburg & Lasheras (1988) for a forced unseparated wake. In mode B, we also observe amalgamation of streamwise vortices from a previous braid with like-sign vortices in the subsequent braid.

It is deduced that the large scatter in previous measurements concerning mode A is due to the presence of vortex dislocations. Dislocations are triggered at the sites of some vortex loops of mode A, and represent a natural breakdown of the periodicity of mode A instability. By minimizing or avoiding the dislocations which occur from end contamination or which occur during wake transition, we find an excellent agreement of both critical Re and spanwise wavelength of mode A with the recent secondary stability analysis of Barkley & Henderson (1996).

Wake transition is further characterized by velocity and pressure measurements. It is consistent that, when mode-A instability and large-scale dislocations appear, one finds a reduction of base suction, a reduction of (two-dimensional) Reynolds stress level, a growth in size of the formation region, and a corresponding drop in Strouhal frequency. Finally, the present work leads us to a new clarification of the possible flow states through transition. Right through this regime of Re, there exist two distinct and continuous Strouhal frequency curves: the upper one corresponds with purely small-scale instabilities (e.g. denoted as mode A), while the lower curve corresponds with a combination of small-scale plus dislocation structures (e.g. mode A*). However, some of the flow states are transient or 'unstable', and the natural transitioning wake appears to follow the scenario: (2D → A* → B).

1. Introduction

There has been a great deal of work recently investigating three-dimensional aspects of wake flows behind cylinders. Most of the recent advances are comprehensively discussed in a review paper (Williamson 1996*a*), with a more general review to be found in Roshko (1993). It is now well known that end boundary conditions (at the ends of the span of a cylinder) are important in controlling wake patterns across the complete span (Williamson 1988*a*, 1989; Eisenlohr & Eckelmann 1989; Hammache & Gharib 1989, 1991; and several others), and indeed in influencing whether the vortex shedding is parallel or oblique to the cylinder axis, in the laminar vortex shedding regime (in the range of Reynolds numbers, $Re = 49$–190). Some of the three-dimensional phenomena that have been discovered over the last eight years, for example oblique and parallel shedding, 'phase expansions' and 'phase shocks' (Miller & Williamson 1994; Monkewitz, Williamson & Miller 1996), cellular shedding and 'vortex dislocations' (Williamson 1989, 1992; König, Eisenlohr & Eckelmann 1990, 1992), are also found to occur under suitable conditions, at much higher Reynolds numbers, of the order of 10^4 (Prasad & Williamson 1997*b*). Such three-dimensional wake phenomena at high Re have an important impact on the unsteady forces on a long structure, by influencing the phase and correlation of these forces along the span. However, only surprisingly few investigations have focused on the wake transition regime (in the approximate range, $Re = 190$–260). From these studies, we at present have almost no understanding of the physical origin of the three-dimensional small-scale instabilities that are fundamental to wake transition, despite the effective use of modern experimental techniques (for example particle image velocimetry, or PIV) and several recent and ongoing direct numerical simulations. Possibly this is partly because of the sensitivity of this regime to experimental conditions and to the difficulty in determining flow structure because of the intermittent nature of the flow. The present paper addresses directly the character and origin of these small-scale instabilities in 'wake' transition.

The first definition of flow regimes based on measurements of velocity fluctuation, spectra and frequency was given by Roshko (1954). He found a 'stable' (periodic) laminar vortex shedding regime for $Re = 40$–150, a transition regime in the range $Re = 150$–300, with an 'irregular' regime for $Re = 300$–$10000+$, where velocity fluctuations showed distinct irregularities. Similar regimes were confirmed by Bloor (1964). A surge of recent work has shed further light on phenomena occurring in these regimes and their precise Reynolds number ranges. The cylinder wake as a whole involves the following three shear flows: a wake flow, a mixing layer flow separating from the sides of the body, and a boundary layer flow on the body surface. Each of these distinct shear layers becomes unstable as Reynolds numbers increase. In this paper, we are concerned with 'wake' transition around $Re \approx 200$, rather than with 'shear layer' or 'boundary layer' transition which occur at $Re \approx 1200$, and at $Re \approx 200000$ respectively.

In this introduction to the small-scale instabilities in wake transition, we shall make reference to the measurements of Strouhal–Reynolds number in figure 1, taken from Williamson (1988*b*, 1992), and to the velocity spectral measurements of figure 2. It may be observed that this wake transition, originally described by Roshko (1954), actually involves two discontinuous changes (Williamson 1988*b*). At the first discontinuity the Strouhal frequency drops from the laminar curve (which is influenced by whether the shedding is parallel or oblique) to one corresponding to a 'mode A' three-dimensional shedding, at around $Re = 180$–194. This discontinuity is hysteretic, and the exact

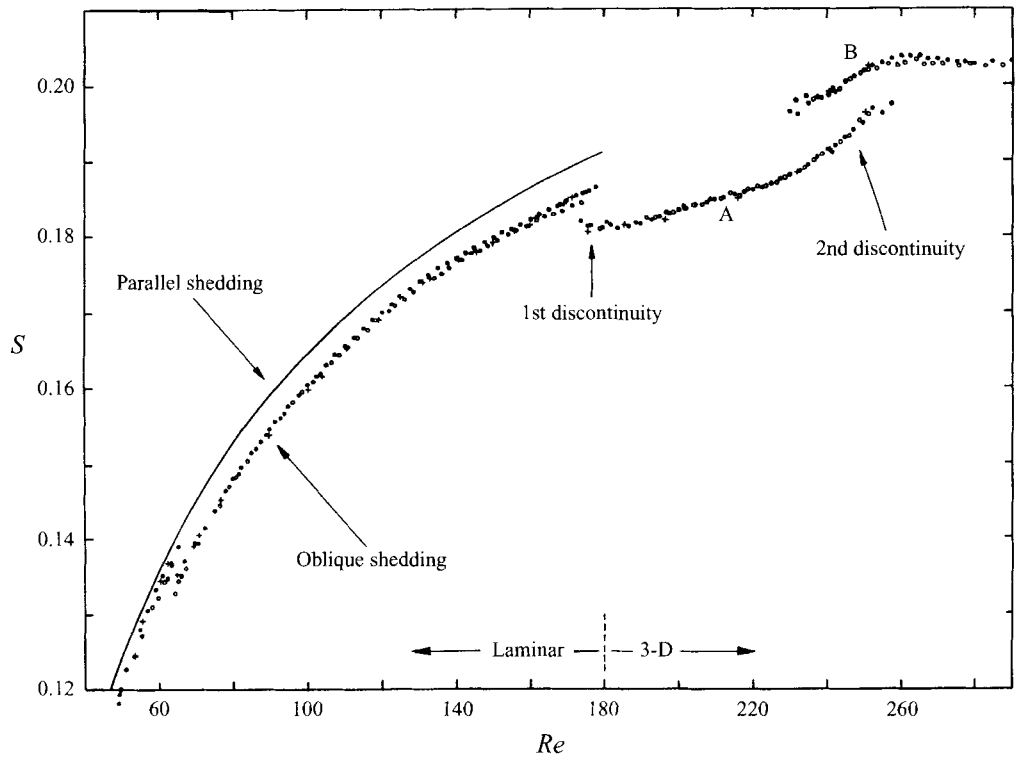

FIGURE 1. Strouhal–Reynolds number relationship over laminar and three-dimensional transition regimes. The transition regime is characterized by two distinct discontinuities in the measured wake parameters, as *Re* is increased, and may be conveniently interpreted with reference to this *S*–*Re* plot.

critical *Re* depends on whether the flow speed is increased or decreased, and on the experimental arrangements, as we shall see below. As *Re* is increased up to the range *Re* = 230–260, there is a further discontinuity in Strouhal number *S*, indicating a further 'mode B'. This discontinuity may be contrasted with the first in that it is not hysteretic, and instead involves a gradual transfer of energy from mode A to mode B, as one increases *Re*. Interestingly, if one refers to the original *S*–*Re* data of Roshko (1954), one finds that most of his scatter is centred around Reynolds numbers corresponding to these two discontinuities. It will be seen later that each of these three-dimensional shedding modes corresponds to a spanwise instability in the wake.

The definition of such Strouhal discontinuities is clearly only possible if one takes long time-averages of the spectra of wake velocity fluctuations. Such spectra are shown in figure 2, where the first discontinuity in (*a*) exhibits two possible spectra at the same *Re* due to the hysteresis effect. At the second discontinuity in (*b*), the spectra are twin-peaked. The lower-frequency peak corresponding to mode A gradually gives way to the peak at mode B, as *Re* is increased. This is due to an intermittent swapping between modes, rather than the simultaneous existence of both modes, and this point will be discussed later in this paper. One might suspect that these two modes are artifacts of the end conditions and are associated with an insufficiently long cylinder (around 200 diameters long in *b*). However, the results of C. Norberg (personal communication, 1989) shown in (*c*) for a length/diameter ratio, $L/D = 2000$, confirms the existence of the two modes A and B at large L/D.

Although there have been surprisingly few measurements made in the transition

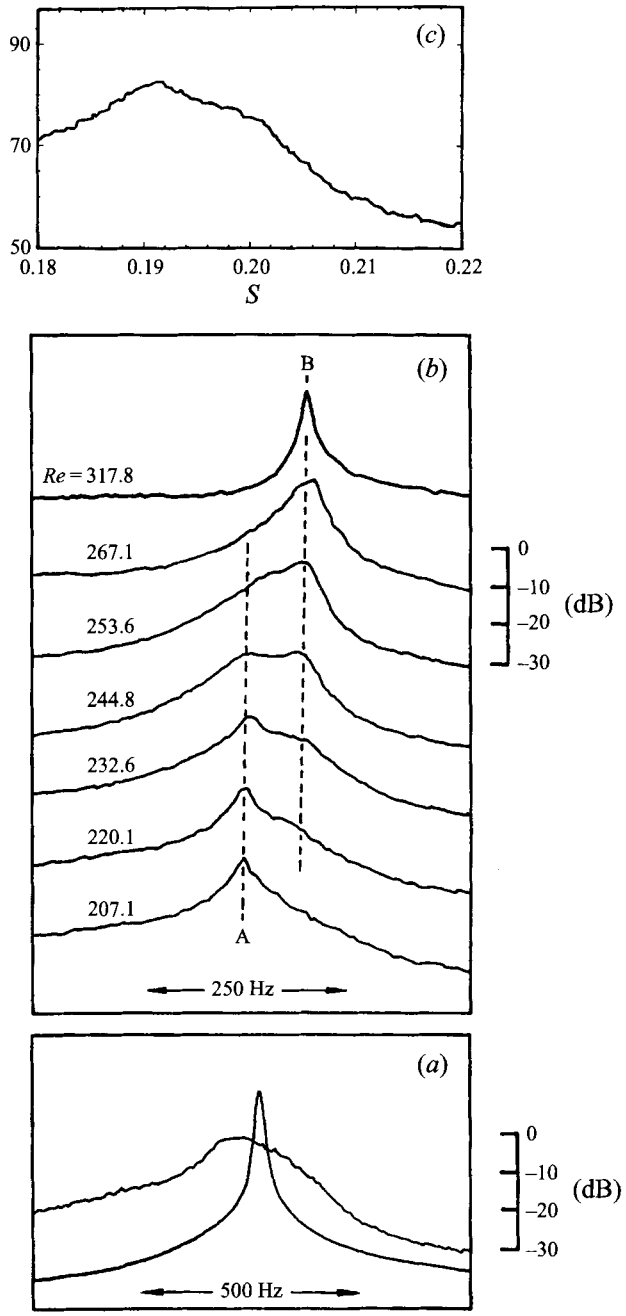

FIGURE 2. Velocity spectra from the near wake in the wake transition regime. (*a*) Spectra at the first discontinuity, showing hysteresis. Re = 172.8. (L/D = 200). (*b*) Spectra at the second discontinuity, showing gradual transfer of energy from mode A to B, as Re increases. Re = 207–318. (L/D = 200). (*c*) Spectra at the second discontinuity, for high aspect ratio, L/D = 2000, for Re = 234.1. From C. Norberg (1989, private communication).

regime to date, there are even fewer flow visualization studies, although some new phenomena in this region have been discovered in the last few years. Based on his early experimental velocity measurements, Roshko (1954) suggested that transition to turbulence existed in the separating shear layers before the vortices were fully formed and shed from the cylinder. High-frequency oscillations were later detected in the separating (and transitioning) shear layers by Bloor (1964). Wei & Smith (1986) observed that 'secondary' vortices were associated with these high-frequency oscillations, and hypothesized that it is the three-dimensional stretching of these secondary vortices that causes streamwise vortices to appear in the wake. However, although this scenario of shear layer transition is known to occur at Re greater than around 1200, the brief but significant visualizations of Hama (1957) showed that the instability in the wake transition regime takes the form of a three-dimensional waviness on the primary Kármán vortices, and the formation of what Gerrard (1978) later calls 'fingers of dye'. Shear layer transition itself is a separate phenomenon in a higher-Re regime. We shall show in the present paper that Gerrard's dye fingers are associated with vortex loops and streamwise vortices, like other well-studied free shear flows.

The existence of two different modes of three-dimensional shedding in wake transition (modes A and B), involving vortex loops and streamwise vortex pairs, was briefly presented by Williamson (1988*b*, 1992), and these have some analogy with the streamwise structure found in free shear layers (for example, Bernal & Roshko 1986; Corcos & Lin 1984), and also in the unseparated wake that forms behind a splitter plate (Meiburg & Lasheras 1988). In mode A, corresponding to shedding frequencies along curve A in figure 1, the primary vortices deform in a wavy fashion along their length during the shedding process, as will be shown later in §4. This results in the local spanwise formation of vortex loops, which become stretched into streamwise vortex pairs. The spanwise lengthscale of these vortex loops is around 3 to 4 diameters, or 3/5 to 4/5 primary wavelengths. At higher Reynolds numbers, when the Strouhal frequencies lie on curve B in figure 1 (i.e. after the second discontinuity), finer-scale streamwise vortex pairs are formed. In this case the primary vortex deformation is more spanwise uniform than for mode A, and the streamwise vortex structure has a markedly smaller spanwise wavelength of around one diameter or 1/5 of a primary wavelength. In the present paper, we shall present accurate measurements of spanwise wavelength corresponding to Reynolds numbers just beyond where wake transition begins (close to $Re = 190$), and these data follow from the more approximate presentations made in Williamson (1987). These and other results will be related to the approximate stability analysis of Noack & Eckelmann (1994), and to the recent Floquet stability analysis of Barkley & Henderson (1996). The experimental agreement with the latter work appears to be excellent, concerning the critical Re for transition and the most unstable spanwise wavelengths for mode A instability. It should also be mentioned here that Henderson & Barkley (1996) go on to show that the secondary bifurcation (near $Re = 189$) is subcritical, which is distinctly different from several previous investigators who concluded that this bifurcation is supercritical. This result relates to the possibility of a hysteresis at the 2D $\Rightarrow$ mode A transition. A comparison between their instability analysis and the experimental mode A measurements, including the inception of vortex dislocations arising from a breakdown of the periodicity of mode A, is included in Williamson (1966*b*).

Direct numerical simulations (DNS) are now contributing strongly to our understanding in this wake transition regime (Karniadakis & Triantafyllou 1992; Zhang *et al.* 1995; Henderson 1994, 1995; Mittal & Balachandar 1995*a–c*, 1996; Persillon & Braza 1996; see also the review of numerical work in Braza 1994). Three-

dimensional DNS computations of wake transition have clearly demonstrated the existence of both modes A and B in computations (Thompson, Hourigan & Sheridan 1994, 1996; Zhang *et al.* 1995; B. N. Noack 1995, personal communications; R. D. Henderson 1994–1996, personal communications). Other work by Mittal & Balachandar (1995*a–c*, 1996) has investigated the near-wake region, showing the structure of primary and streamwise vorticity interactions, indicating consistent results with some of the present conclusions, but the short spanlength in their case precludes discussion of modes A and B. Mittal & Balachandar (1996) suggest a process of what they call 'autogeneration' of streamwise vortices, which has some relevance to the mechanisms causing mode B, and will be further discussed in this paper in §9. A further mode C three-dimensional instability has been proposed by Zhang *et al.* (1995), for $Re = 170$–270, based on the approximate stability analysis of Noack & Eckelmann (1994). The question as to the existence of such a mode (in a natural unforced wake) will be taken up in the Discussion §9, in the light of the full Floquet stability analysis of Barkley & Henderson (1996) and in the light of other experiments to date.

The study of Karniadakis & Triantafyllou (1992) suggested that the wake becomes three-dimensional as a result of a secondary instability of the two-dimensional vortex street, which is confirmed by Barkley & Henderson (1996), discussed earlier. Karniadakis & Triantafyllou state that, as Re is increased, the wake velocity fluctuations indicate a cascade of period-doubling bifurcations, which create a chaotic state in the flow at around $Re = 500$. Period doubling in this case refers to the three-dimensional structure, rather than inferring the presence of primary vortex pairing. This scenario has recently been supported by DNS computations of Mittal & Balachandar (1995*c*), and also by the experimental results of Mansy, Yang & Williams (1994) and D. R. Williams (private communication), using an ingenious scanning laser anemometer. Despite the evidence above, it appears relevant that Thompson *et al.* (1994, 1966) do indeed find period doubling in their simulations, but only for small spanwise domains close to $1D$–$1.5D$, and for larger domains there is no evidence of period doubling. The simulations mentioned earlier both have spanwise domains of around $1D$–$1.5D$, so the matter of period doubling perhaps remains an interesting subject of further research.

The present work was begun in 1986, whilst the author was at California Institute of Technology, and part of the early work was reported in Williamson (1987). A preliminary overview of some aspects of the wake transition problem was also presented in Williamson (1988*b*, 1992). The former paper introduces the two modes A and B and the two discontinuities in a plot of S–Re, while the latter paper is concerned with large structures in the form of 'vortex dislocations' in wake transition. The present comprehensive study intersects these other preliminary studies, but goes significantly further, and is concerned mainly with small-scale instabilities and modes rather than with the large-scale dislocations. In §3, we present some of the general characteristics associated with wake transition, with reference to both velocity and spectral measurements and also smoke and particle visualization, which demonstrate essentially the existence of the two scales of streamwise vorticity for the two modes A and B. In §4, we present spanwise wavelength measurements and a discussion of critical Re for wake transition, which is in excellent agreement with the Floquet stability analysis of Barkley & Henderson (1966) for the mode A instability. The physical origins for the growth of modes A and B instabilities are presented. In both modes, the mechanism of streamwise vortex stretching in braid regions between concentrated vortices has close similarities with the stretching and amplification of streamwise vorticity that has been made clear in free shear layer studies (Bernal & Roshko 1986;

Corcos & Lin 1984; Meiburg & Lasheras 1988; Rogers & Moser 1992; and several other papers, referenced therein). Streamwise vortex stretching in the wake has also been demonstrated by the simulation of Wu *et al.* (1995). It is shown in §4 that the symmetries of modes A and B streamwise vortex structure are distinctly different to each other. It is of interest that both of these natural modes in the separated wake may be related to the two forced patterns in an unseparated wake from a splitter plate, studied by Meiburg & Lasheras. In §5, we present wake velocity and spectral measurements, which show rather distinct changes associated with transition. We find consistent variations of stress, base suction, wake width and formation length, as the flow undergoes wake transition. The marked peak in base suction and in the level of stress in the near wake at a Reynolds number of 260, coupled with the almost periodic velocity fluctuations, and the ordered flow structure, leads one to suspect that there is some form of resonance at this Re. In §6, it is suggested that an interaction between the instability of the separating shear layer and the instability of the wake could possibly explain this resonance at $Re = 260$.

Having indicated, from the velocity measurements, the predominance of very large scales in the flow in §5, we are led into a brief discussion of large-scale 'vortex dislocations' in §7. These are vortical structures which originate from phase dislocations of the primary vortex shedding near the body, and were shown in Williamson (1992) to be a significant fundamental natural phenomenon in the wake transition regime. They should not be confused with such dislocations which can occur at the spanwise ends of a long cylinder (Gerich & Eckelmann 1982; Eisenlohr & Eckelmann 1989; Williamson 1989) due to the existence of cellular shedding near the ends. In §8, we discuss the possible stable and unstable flow states through wake transition, relating the existence of dislocations to the sharp and hysteretic drop in Strouhal frequency, as mode A appears in the data of figure 1. In §9, there follows a discussion, and a comparison of the present experimental results with those recently found in DNS computations. The conclusions follow in §10.

2. Experimental details

Measurements of velocity fluctuations were made with a miniature hot wire situated in the wake of cylinders of diameter 0.00051, 0.00061 and 0.00108 m, in a 0.305 m square test section (12 in. by 12 in.) of an open-circuit suction wind tunnel at Cornell. Some of the measurements were made in a 6 in. circular-test-section open-jet wind tunnel at California Institute of Technology, whose details were described in Williamson (1989). The turbulence level was close to 0.1 %, with flow uniformity better than 0.3 %, in both facilities. A good deal of care was taken to isolate the cylinders from the tunnels, and to damp out any cylinder vibrations. In most cases, the spanwise end conditions comprise end plates parallel with the flow, in the manner described in Williamson (1989).

Flow visualization in air at Cornell was conducted using a smoke-wire system in the manner originally described by Corke *et al.* (1977). Flow visualization was also conducted in an X–Y Towing Tank (at Caltech). Cylinders of diameter 0.00328 and 0.00657 m were towed along the length of the tank, and the shed vorticity was visualized using laser light which excited fluorescein dye washed off the surface of the cylinders. In the case of stereoscopic flow visualization, two synchronized Nikon F3HP motordrive cameras were used. They were linked to a function generator which output TTL pulses at a prescribed low frequency of typically around 0.3 Hz. An effective yet simple aluminium-flake technique was also used, whereby the water channel contained

a homogenous distribution of flakes, which were then disturbed by the passage of the towed vertical cylinder. From the orientation of the light sheet source (parallel to the wake centreplane yet out to one side) coming from below the tank's glass bottom, coupled with the camera looking horizontally at the wake patterns through the sidewall of the tank, it proved possible to determine the patterns of streamwise vorticity. The brightest reflections came from the flakes which were wound around the horizontal (streamwise) vortices.

The origin of the wake coordinate system is fixed on the axis of the cylinder. The x-axis is downstream, the y-axis is perpendicular (defined as transverse) to the flow direction and to the cylinder axis, and the z-axis lies along the axis of the cylinder (defined as spanwise). Similarly, in the discussions of near-wake vortex instability, the (x, y)-plane is the cross-sectional plane, while the z-axis is measured spanwise along the vortex. Unless otherwise stated, the data for the transverse velocity profiles are measured for positive y, and the mirror image used for negative y, under the assumption of symmetry.

3. General characteristics associated with three-dimensional wake transition

Velocity spectral measurements in the wake transition regime display quite different characteristics at the two Strouhal frequency discontinuities, as described in the Introduction. In the case of the drop in frequency as the laminar shedding regime changes to mode-A three-dimensional vortex shedding, there is a hysteresis. On the other hand, the second discontinuity from mode A to mode B is characterized by the twin peaks in the spectra, and a gradual transfer of energy from the lower frequency of mode A to the higher frequency of mode B, as Re is increased. The point must be made that this is not due to a coexistence of these two frequencies at one time, as one may naturally think, but is due to an intermittent swapping between the lower-frequency and the higher-frequency modes. Experiments have shown that, over as short a time as possible to retrieve a spectrum, one can observe predominantly one of the modes, with subsequent spectra intermittently exhibiting predominantly the other mode. Clearer spectra averaged over longer time show both modes, as found in figure 2.

In figure 3, we show clearly the transfer of fluctuation intensity from mode A to mode B, as Re increases. This is represented by the measurement of $(u'_{rms}/U)_{peak}$ evaluated at the peak frequencies in the spectra. Both modes A and B have equal energy at close to $Re = 245$, and by $Re = 260$ only mode B can still be detected. In figure 3(b), we further characterize the spectra by a measurement of bandwidth, showing a sharp jump increase, as expected, as one changes from laminar to mode-A shedding (near $Re = 190$), followed by a further dramatic maximum in bandwidth around $Re = 245$, where the two modes are competing equally. A sharp reduction in bandwidth is reached for $Re = 260$ and above, as the flow settles continuously into the mode B. In fact, these trends are even clearer if one deliberately induces parallel shedding by manipulating the end boundary conditions, as shown in Prasad & Williamson (1997b).

Velocity fluctuations correspondingly exhibit distinct characteristics as Re increases through wake transition. In figure 4, the laminar-shedding periodicity at $Re = 152$ gives way to intermitting 'glitches' in the time traces at $Re = 210$, which have been interpreted, using simultaneous visualization with velocity measurement in Williamson (1992), to mark the passage of vortex dislocations past the measuring probe. It is significant that the broad spectra reflect the presence not only of mode-A small-scale

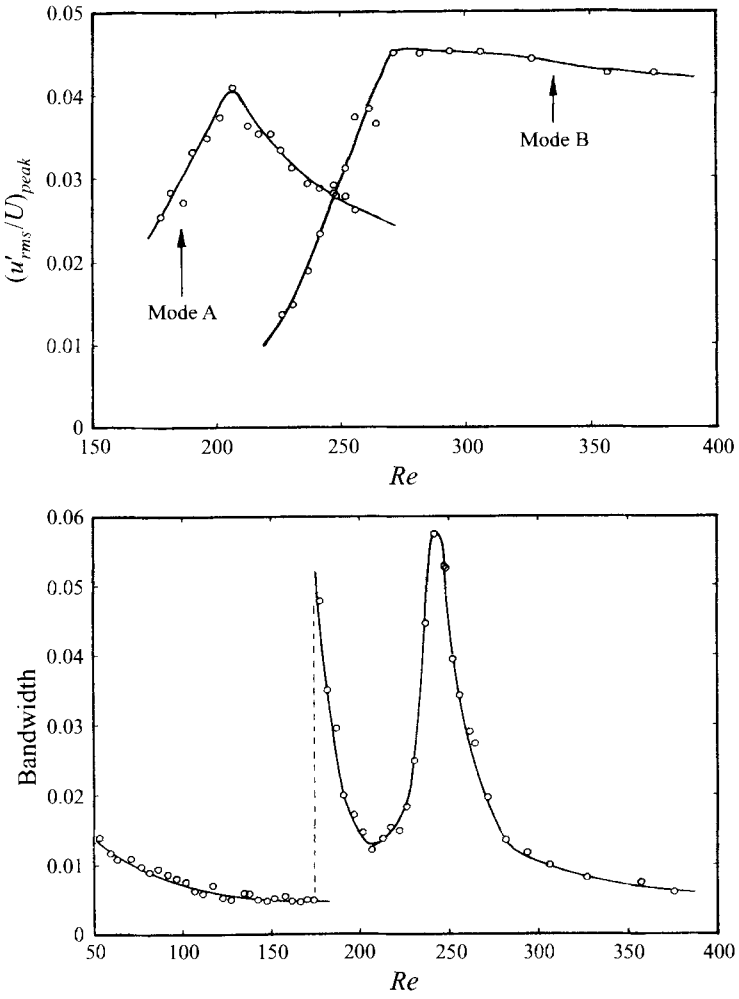

FIGURE 3. Peak energy and bandwidth of the spectra, through the wake transition regime. (*a*) Peak values of (u'_{rms}/U) measured at the peaks in the spectra, clearly exhibiting the transfer of energy from mode A to mode B. (*b*) Spectral bandwidth through wake transition. The maxima correspond with the competition between modes of shedding.

instabilities, but also of the very large scales of the dislocations. We shall show how these two phenomena are related directly to each other in §7. At the higher $Re = 260$, in figure 4, the glitches are almost non-existent, suggesting that the dislocations are very sparse, and indeed cannot be detected at all if parallel-shedding end conditions are deliberately arranged. At $Re = 520$, the time trace has become less periodic, as wake three-dimensionality becomes more disordered.

Corresponding flow visualization, using smoke, in figure 5, shows clearly that there are distinct stages through wake transition, as deduced briefly in Williamson (1988*b*). The laminar shedding case $Re = 152$ appears remarkably like the case at $Re = 260$ (noting that in both these photographs we have parallel shedding). Aside from the fact that the streamwise wavelength is less at $Re = 260$ than at $Re = 152$, there is an ordered fine-scale three-dimensional structure at $Re = 260$ for mode B (visible by scrutinizing this photograph), which is not present at $Re = 152$ in the laminar-shedding regime. One can exert control over shedding angle through end boundary condition

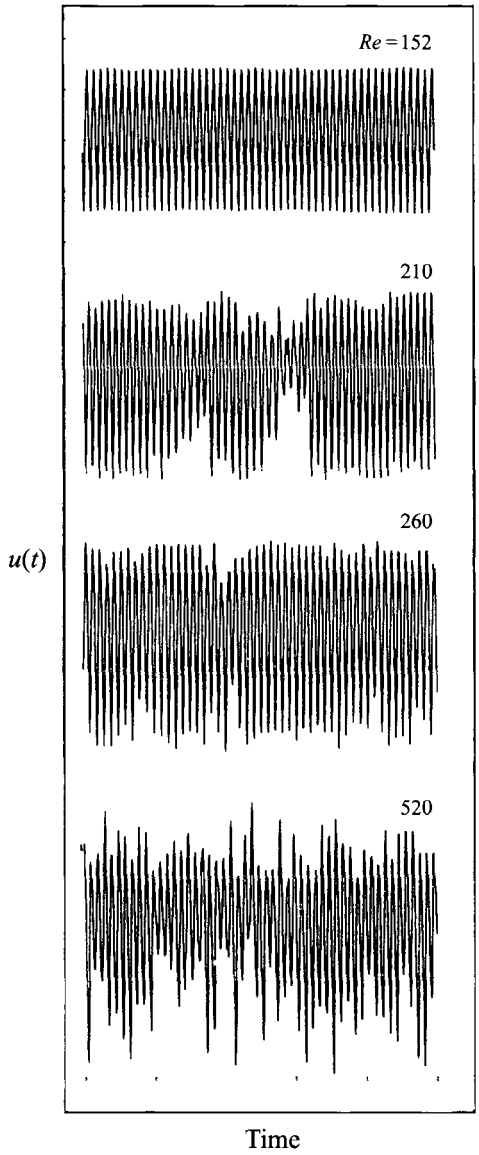

FIGURE 4. Typical time traces of velocity fluctuation through the wake transition regime. Transition involves the loss of periodicity at $Re = 210$, although it is closely regained at $Re = 260$, despite the presence of small-scale three-dimensionality in the flow. Beyond the wake transition regime, increasing disorder is evident in the fluctuations of $Re = 520$. Hot-wire is at $x/D = 10$, $y/D = 1.3$.

manipulation at (and above) $Re = 260$ for mode B (Prasad & Williamson 1997*b*), just as one can control the flow pattern in the laminar regime. However, this is not the case at the intermediate Reynolds numbers, as indicated, for example, by the mode A case at $Re = 210$, where the presence of intermittent (naturally occurring) dislocations across the complete span effectively decouples the end conditions from the bulk flow across the span. The wake shedding pattern is broken up, and has the same appearance and a similar spectrum, irrespective of whether parallel or oblique shedding conditions are attempted by end manipulations.

By the use of aluminium-flake visualization in figure 6 for $Re = 205$ and 260, we can

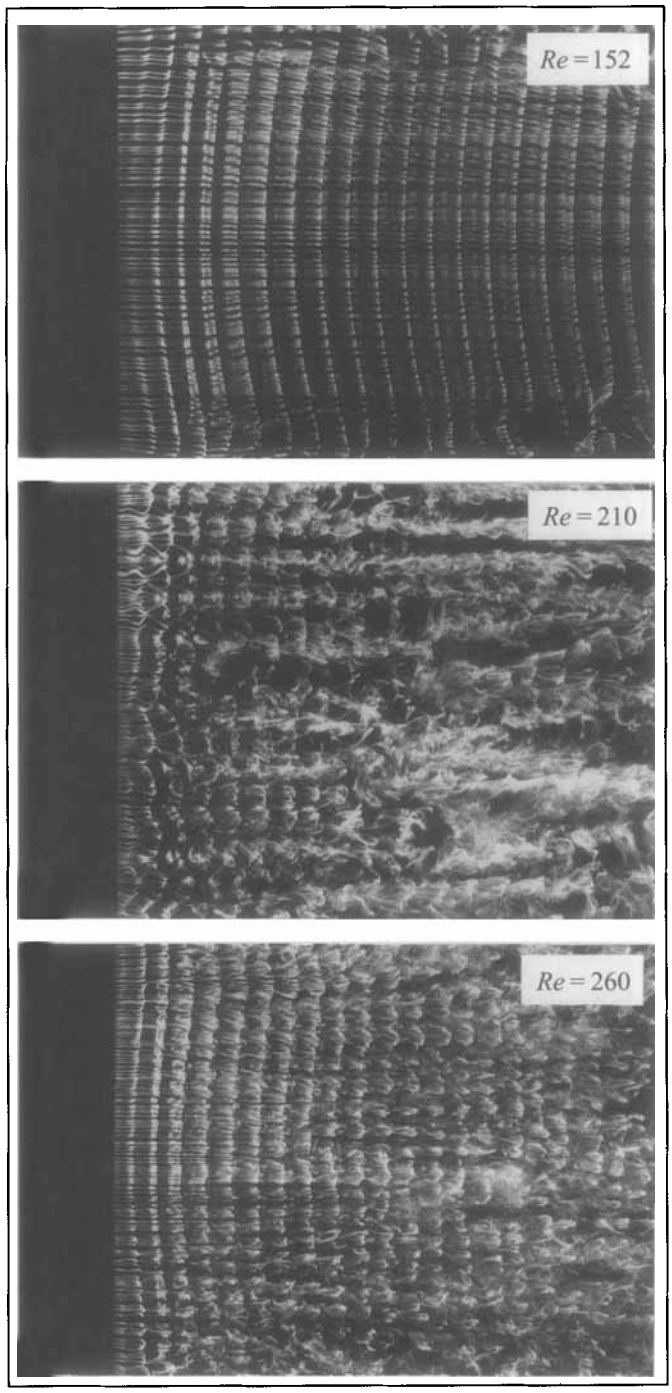

FIGURE 5. Smoke visualization through the wake transition regime. Corresponding with the loss of periodicity at $Re = 210$ in figure 4, is a breakup in the spanwise coherence of vortex shedding, due to the presence of large-scale (dislocation) structures in the flow. The return to a closely periodic flow at $Re = 260$ corresponds with the almost laminar-shedding appearance at this Re, although one can observe regular small-scale structures at $Re = 260$, which are not present at $Re = 152$. Flow to the right, with smoke wire located $10D$ downstream of vertical cylinder axis on the left.

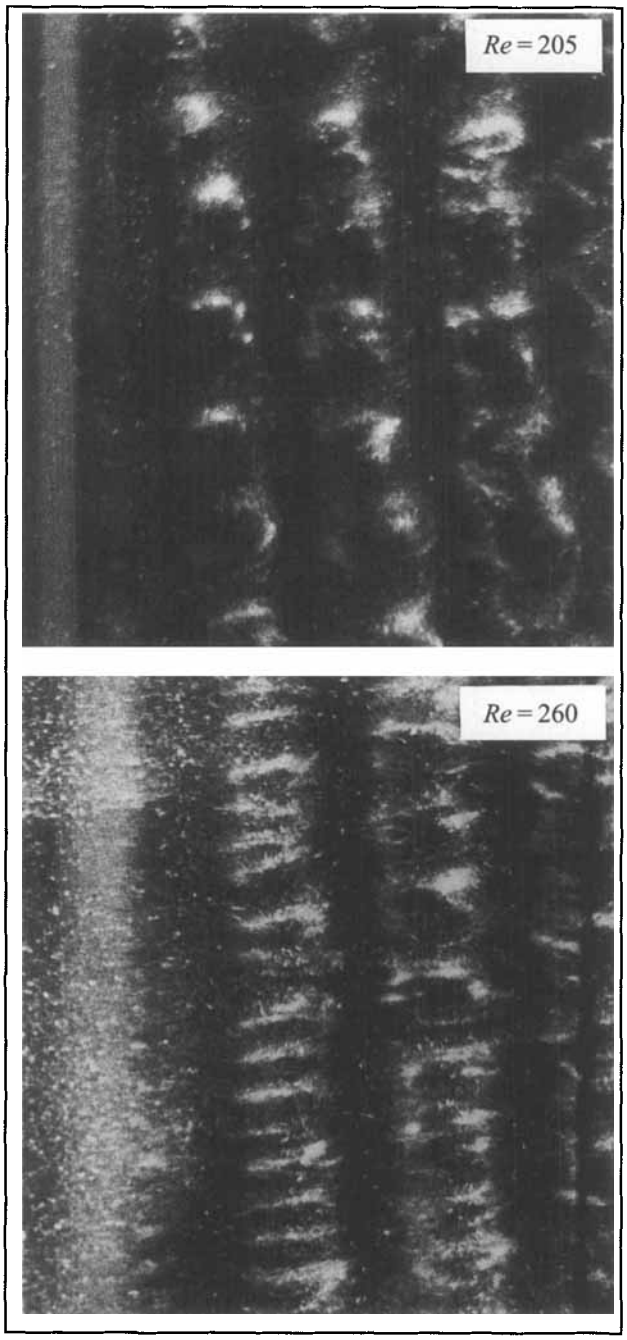

FIGURE 6. Aluminium-flake visualization in planview: evidence for distinct streamwise vortex structure for modes A and B. There is clearly a jump in the spanwise lengthscale of the streamwise vortices between $Re = 205$ (mode A) and $Re = 260$ (mode B). Note that this technique enables one to see predominantly streamwise vorticity by the white regions, and that the method shows essentially the instantaneous structure, without the well-known history effects of dye and smoke injection. Flow is to the right, with vertical cylinder at left.

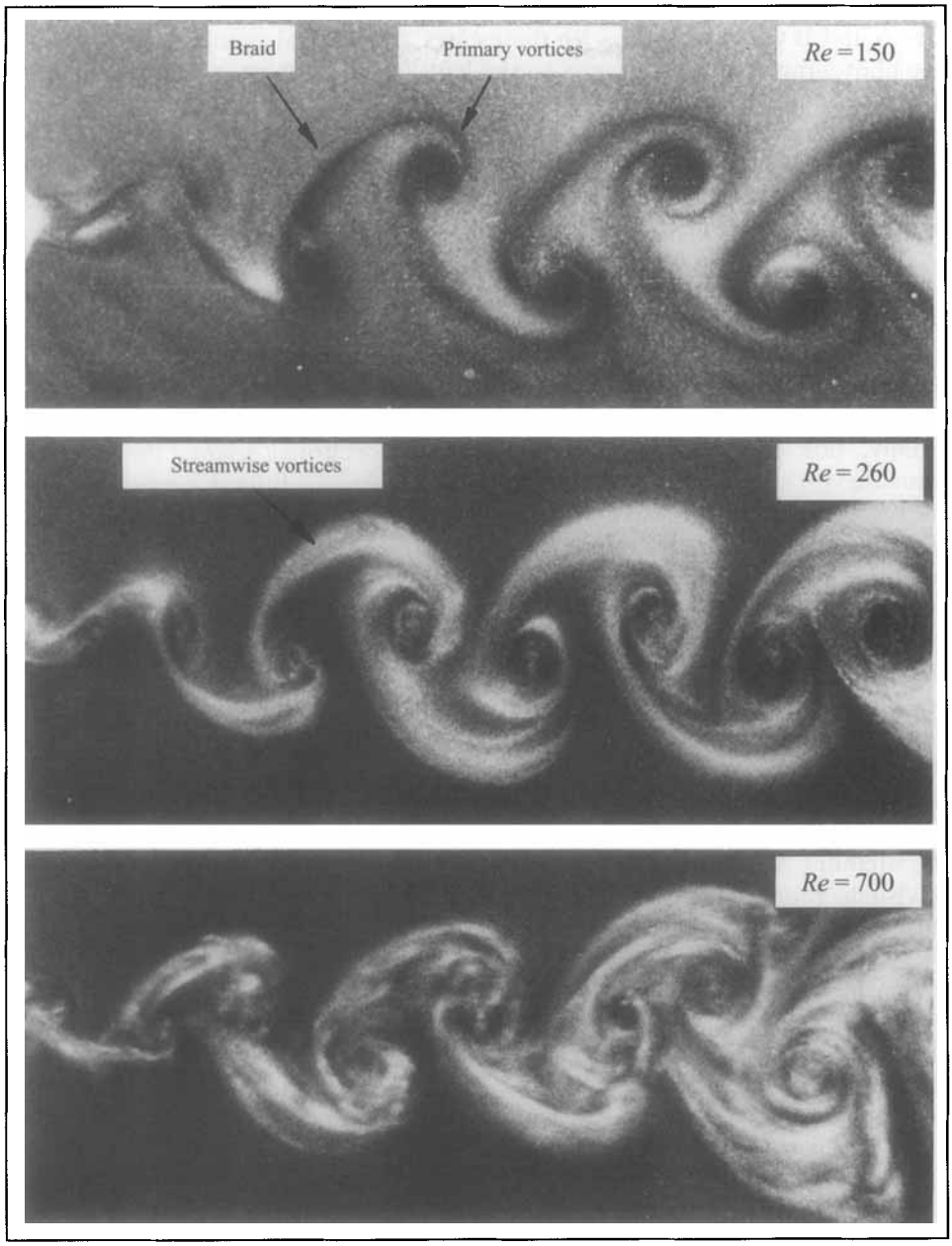

FIGURE 7. Aluminium-flake visualization in cross-sectional view: evidence for the location of streamwise vorticity in the braid shear layer regions between primary vortices. One may simply contrast, with this technique, the dark regions at $Re = 150$, indicative of two-dimensional wake formation, with the white regions at $Re = 260$, indicative of the streamwise vorticity in the braids. Increasing disorder of this three-dimensional structure is observed at $Re = 700$, although clearly the vigorous streamwise vorticity remains resident in the braids. Flow is to the right past the cylinder on the left.

demonstrate the existence of streamwise vorticity of distinct spanwise wavelength for modes A and B vortex shedding. In these cases, the vertical cylinder is at the left edge of the photographs, and is moving to the left. The light sheet is parallel to the wake centreplane, but is located towards the viewer relative to the centreplane. As the wake widens laterally downstream, it pushes through the light sheet, towards the viewer. Since the light sheet comes from a source below the photographs, and we are using aluminium flakes, which orient themselves with the stream surfaces in the fluid, the horizontal bright lines now represent horizontal, or 'streamwise', vortices in the wake flow. At $Re = 205$, for mode A, we can clearly see that the spanwise wavelength of the streamwise vortex structure is distinctly larger than for mode B shown below at $Re = 260$, where the structure is strikingly periodic and well ordered. The sharp difference in spanwise lengthscale between the two modes A and B already suggests strongly that there are two distinct spanwise instabilities in the wake flow. This will be made evident in the next Section.

Finally, one can observe, even in the cross-sectional plane, the presence of streamwise vortices. Again, the aluminium-flake technique is used, see figure 7, and the white regions (within the wake structure) mark the presence of streamwise vortices. One should note that the technique does not involve a flow marker like dye or smoke, which have a history effect, but rather the flake patterns are responding to the flow structure at the time the photographs are taken. For the case $Re = 150$, we can also see the dark regions where flakes are oriented around the axes of the primary vorticity (whose vectors are perpendicular to the photographs), and the density of reflecting flakes is even less than for undisturbed fluid. It is clear, by comparing $Re = 152$ (laminar shedding) with $Re = 260$ (mode-B shedding) that the streamwise vortices lie along the braid shear layer regions between primary vortices. It is here that streamwise vorticity is vigorously stretched in the strain-rate field due to the primary vortices, in the same manner as found in mixing layers and unseparated wakes (Bernal & Roshko 1986; Meiburg & Lasheras 1988). Although this simple, but effective, technique of flow visualization shows clearly the location of the streamwise vorticity, it is also confirmed by the extensive measurements of Wu *et al.* (1995). As one increases Re to $Re = 700$, figure 7 shows a persistent presence of these streamwise vortices. Indeed it is shown in figure 1 of Williamson (1996*a*) that streamwise vortices are present at $Re = 4000$ (using the present technique), and they are found at $Re = 270000$, from the schlieren photographs of Thomann (1959). Their presence is shown experimentally for moderate Reynolds numbers (of order 10^3–10^4) by Wei & Smith (1986) and by Bays-Muchmore & Ahmed (1993) using hydrogen bubbles in water, and by Chyu & Rockwell (1996) using DPIV techniques.

The two scales associated with modes A and B instabilities are often complicated by the presence of the large-scale dislocations, and, possibly for this reason, almost no understanding of the physical origin of these two modes is at present to hand, despite the few papers which investigate wake transition. These questions are directly addressed in the following section.

4. Instability modes A and B in wake transition

We have seen in the previous section that modes A and B involve streamwise vortex structures of distinct spanwise lengthscale. In this section, we shall investigate the instabilities causing these modes to appear, and it will be seen that the two instabilities scale on different physical parts of the wake flow.

In figure 8(*a*), the dye visualization shows the mode-A instability at $Re = 200$,

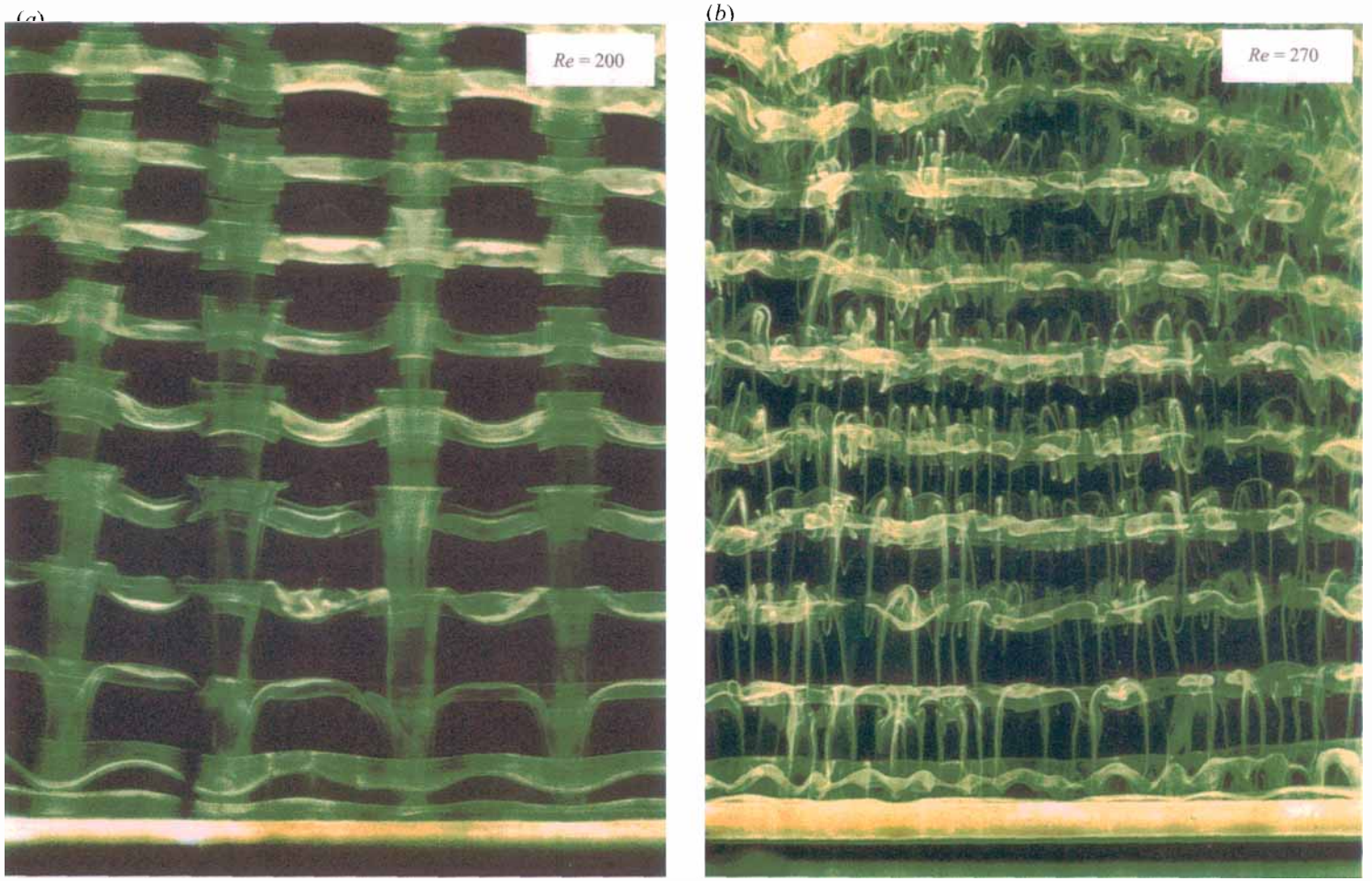

FIGURE 8. Modes A and B three-dimensional instabilities. (*a*) Mode A instability, associated with the inception of streamwise vortex loops. This specific example for $Re = 200$, corresponds to a spanwise wavelength $\lambda/D = 4.01$, which is remarkably close to the maximum growth rate from Floquet analysis, Barkley & Henderson (1996). (*b*) Mode B instability, associated with the formation of finer-scale streamwise vortex pairs. $\lambda/D \approx 1.0$. $Re = 270$. Note that both photographs are to the same scale, and flow is upwards.

demonstrating that the primary Kármán vortices develop a waviness from which vortex loops evolve. In this case, we may note that the spanwise wavelength is given by $\lambda/D = 4.01$ for $Re = 200$. Mode B is shown in figure 8(*b*) at $Re = 270$, to exactly the same scale as in (*a*) In sharp contrast to mode A, this mode is characterized by a much smaller spanwise scale of close to $\lambda/D = 1$, again suggesting the existence of a distinctly different mechanism to cause spanwise instability than is found for mode A.

The precise value of critical Reynolds number at which wake transition first appears, and the wavelength of the initial instability, are both surprisingly difficult to evaluate from experiment and simulation, as is evident from the large scatter in the literature (see figure 9*a*). However, a precise definition of these measurements is indeed possible, if one considers two experimental characteristics: the contamination from end boundary conditions, and the fact that one must measure spanwise wavelength in the absence of interfering dislocations. (We refer here to those dislocations spontaneously occurring along the span in the transition regime, not to those induced by the end conditions.) At the present time, Barkley & Henderson (1996) have just completed a highly accurate Floquet stability analysis, from which one may compare, with the experiments, the conditions for the initial instability of mode A.

4.1. *Incipience of wake transition*

Regarding the inception of wake transition in experiment, there is a relatively large range of critical Re for wake transition ($Re = 140$–190) quoted in the literature. Surprisingly, the origin of these differences has had almost no attention in the literature, except for the study by Bloor (1964), and recent studies by Hammache & Gharib (1989), and Miller & Williamson (1994). Bloor found that Re_{CRIT} could vary between 140 and 190, depending on the level of free-stream turbulence (0.03–1.0%), although the end conditions are unknown in these experiments. However, it now appears that in a number of facilities, even with essentially the same turbulence level (of order 0.1%) and comparable oblique shedding angles, investigators have nevertheless found a large disparity in Re_{CRIT}: for example, Roshko (1954) and Tritton (1959) found $Re = 150$; Zhang *et al.* (1995) found $Re = 160$; Eisenlohr & Eckelmann (1989) and Norberg (1994) found $Re = 165$; and Williamson (1988*a*, 1989) found $Re = 178$. In a related study, Hammache & Gharib (1989) suggested that transition was triggered early at $Re = 156$ by the fact that the shedding was oblique, rather than parallel, although in changing the oblique angles, they were simultaneously varying the end conditions. In contrast, Leweke & Provansal (1995) have found, in the wake of a ring cylinder (torus), that the oblique modes have a higher critical Re than the parallel modes, which suggests just the opposite result.

It has recently been shown (Miller & Williamson 1994) that non-mechanical end conditions (using suction tubes downstream of the body) can yield rather 'clean' end conditions, in essence without the large unsteady flow structures (vortex dislocations) at the cylinder spanwise ends that are normally present. It is found that, under these conditions, the laminar regime for parallel shedding can be extended up to $Re_{CRIT} = 194$, as indicated later in the data of figure 34. The central conclusion from the above studies is that wake transition is triggered early due to end conditions, and, in the absence of other effects, it would appear that end contamination could account for the large scatter in the quoted critical Reynolds numbers for transition, reported over the last forty years. Physically, this contamination takes the form of regions of vortex dislocations moving across the span.

The above conclusions regarding an accurate determination of critical Re from experiment are most timely since analytical studies are, at the present time, predicting

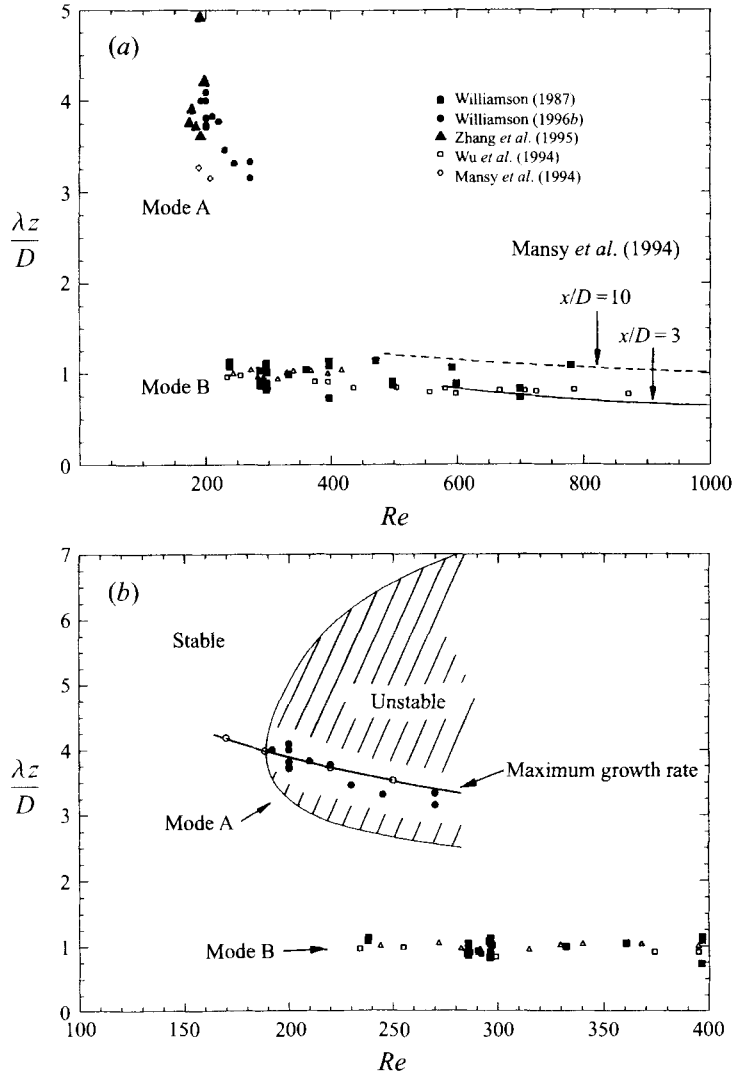

FIGURE 9. Spanwise instability wavelengths of the two three-dimensional instabilities. Normalized spanwise wavelength of streamwise vortex structures (λ_z/D) versus Re. It can be seen that there are two distinct wavelengths for mode A and B instabilities. (*b*) Comprises only part of the data of (*a*), and compares experimental data for mode-A instability wavelengths with the Floquet analysis of Barkley & Henderson (1996). It is significant that in the latter more-accurate experimental data, measurements are made for purely mode A, in the absence of interfering dislocations.

critical Reynolds numbers for wake transition. Noack & Eckelmann (1994) have conducted an approximate analysis, using a low-dimensional Galerkin method (with 100 modes), and find $Re_{CRIT} = 170$, somewhat below the experimental value of 194. However, Barkley & Henderson (1996) have predicted three-dimensional instability from their Floquet stability analysis (including 10000 modes), and find $Re_{CRIT} = 188.5$ (± 1.0), which is in excellent agreement with the recent experiments. It should also be mentioned that Persillon & Braza (1996) also find a critical Re close to 189, based on (nonlinear) DNS computations. In fact, it is quite possible that the small differences in Re_{CRIT} between the Floquet results and the experiments can be attributed to the fact that a small wavy instability may indeed exist in the experiment, prior to $Re = 194$, but

which is insufficient to begin to form dislocations, and thereby to cause a broad spectrum and a corresponding reduction in Strouhal number. These were the experimental characteristics that were taken to indicate transition, in this case.

Comparisons of experimental and theoretical predictions of spanwise wavelengths for modes A and B can now be made in figure 9, using the stability analysis of Barkley & Henderson (1996). In the collected experimental data in figure 9(*a*), it can be seen that there is a discontinuous reduction in lengthscale, as one passes through the second discontinuity of figure 1 ($Re = 230$–250). However, what also appears to stand out in figure 9(*a*) is the large degree of scatter for the mode A measurements. Despite this evident large scatter, indicating a range of $\lambda_z/D = 3.0$–5.0, Zhang *et al.* (1995) interpret the wavelength as having a constant value: $\lambda_z/D = 4.0$, for mode A. On the other hand, Mansy *et al.* (1994) find values close to $\lambda_z/D = 3.0$, and the data of Williamson (1987) suggest a decreasing wavelength as Re increases, although again the degree of scatter precluded precise conclusions. However, this latter trend is now confirmed in the present measurements, where it appears that one can only make suitable accurate measurements of the mode-A wavelength during the early stages of the instability. Such measurements have been made possible in our towing tank, where the data for spanwise wavelength may be extracted before dislocations appear spontaneously along the span.

In figure 9(*b*), we can see that there is excellent agreement between the present experimental determination of mode-A wavelengths, when measured accurately in the above fashion, with the curve of wavelengths having maximum growth rate, derived from the theoretical data in Barkley & Henderson (1996). The experimental data measured for $Re > 230$ reflect a transient condition, whereby mode A appears in advance of mode B (or a mix of A and B, indeed in advance of dislocations), during an experimental run. This is a transient feature confirmed by numerical simulations (Thompson *et al.* 1994). The prediction from Barkley & Henderson of a range of unstable wavelengths, which is a function of Re, almost (but not quite) encompasses all the scatter of mode-A experimental data in (*a*). At their critical Reynolds number, $Re_{CRIT} = 188.5$, Barkley & Henderson find an instability wavelength for mode A of $\lambda_z/D = 3.96$. This is surprisingly close to the present measurements, one of which may be derived directly (with a ruler) from the visualization in figure 8(*a*), yielding $\lambda_z/D = 4.01$ at $Re = 200$. (Accurate measurements were made from enlargements of the original photographic negatives.) It should, however, be noted that vortex loops have been observed in experiments at Re lower than 194, under conditions when there is early transition associated with the presence of contaminating dislocations from the ends of the body.

4.2. *Origin and symmetry of mode-A three-dimensional instability*

Despite the excellent agreement between experiment and theory for the critical Reynolds number for wake transition, and for the initial wavelengths of instability, one is left with the central question as to what is the physical origin of these three-dimensional instabilities, and it seems from the jump in lengthscale that there exist two different three-dimensional instability phenomena, scaling on two different physical features of the wake flow, as mentioned earlier.

Mode A would appear to be due to an instability of the primary vortex core during the process of shedding, causing a spanwise waviness. The spanwise core instability is clearly evident in the wake visualizations from the start-up conditions in the towing tank, where the early state of the instability may be observed. (An example of such an early-developed flow visualization may be found in Leweke & Williamson 1996.) The

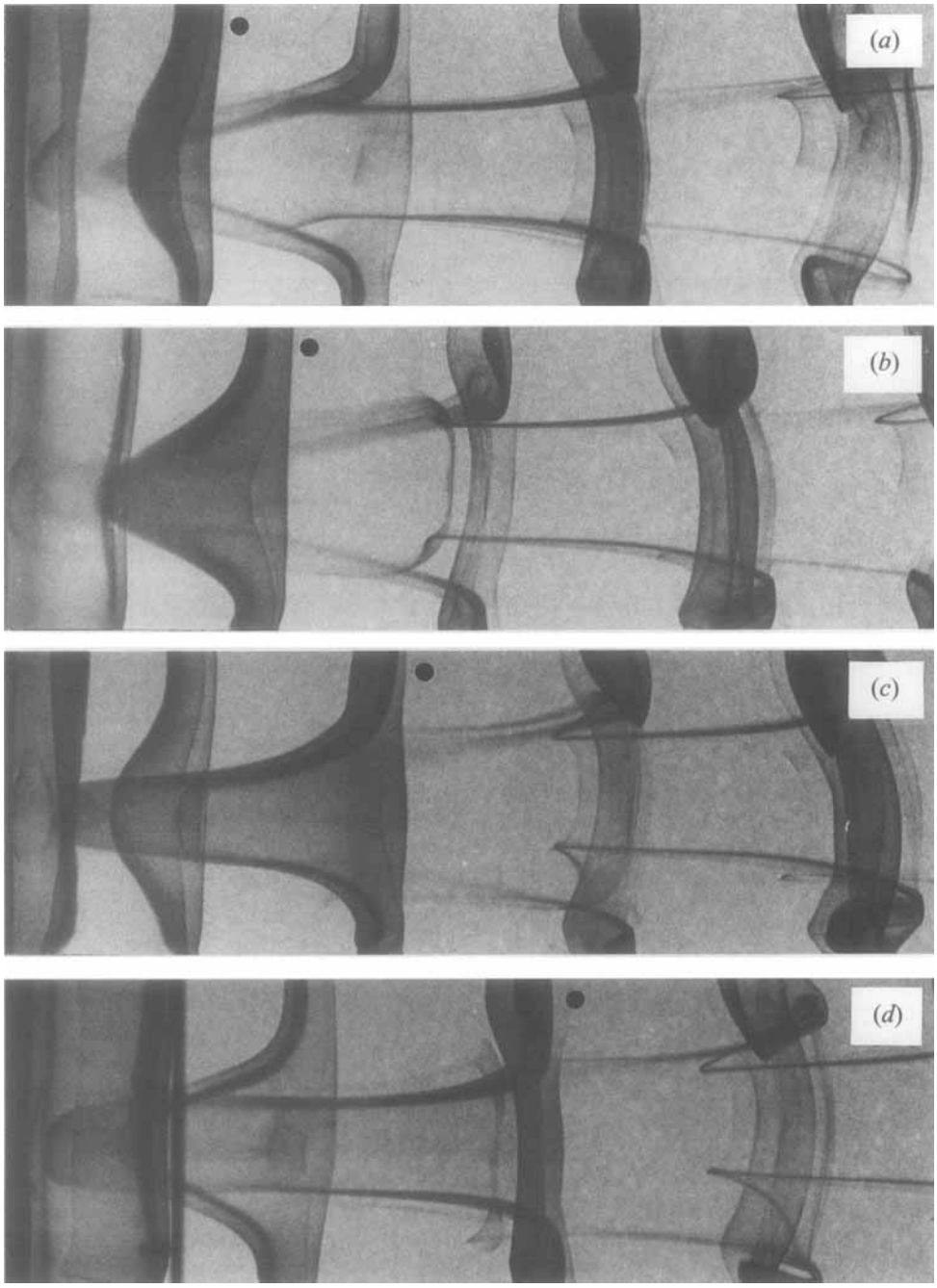

FIGURE 10. Visualization of self-sustaining vortex loop formation of mode A. One may observe the vortex loop marked with a blob in the sequential photographs being deformed by the presence of the previous vortex loop, thus generating a series of loops at the same spanwise location. Flow is to the right past the vertical cylinder on the left.

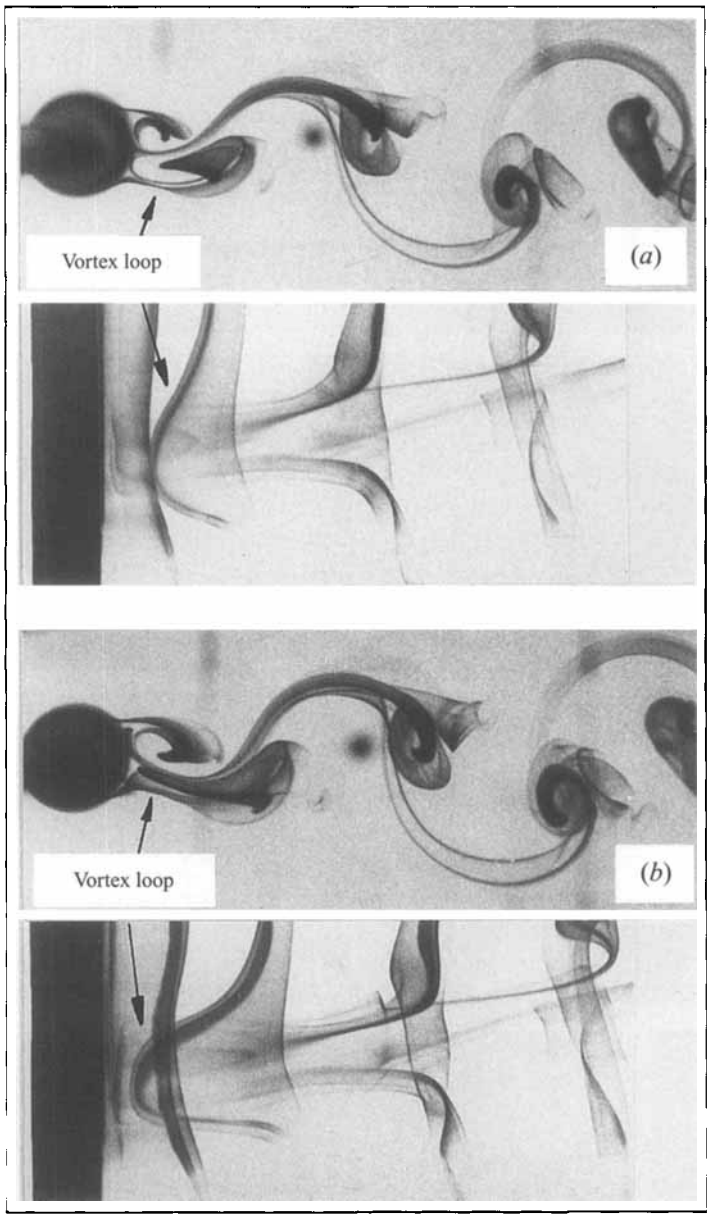

FIGURE 11. Location of vortex loops from simultaneous views in plan and cross-sectional planes. The vortex loop segment of the primary vortex, as seen in the cross-sectional plane, appears to be in the more central region of the near wake. It is thus pulled from the primary vortex back upstream, while the rest of the primary vortex sheds into the wake. Simultaneous views are made possible with the use of systems of mirrors, with both images focused into a single camera.

subsequent growth of vortex loops is due to a feedback mechanism from one primary vortex to the next. During an experimental run, the initially small waviness grows until vortex loops, pulled out of the deforming primary vortices, are stretched in the braid regions. Not surprisingly, the spanwise wavelength of the vortex loops is equal to the initial wavelength found in the primary vortex cores. This vortex deformation and loop generation is self-sustaining, as demonstrated clearly in figure 10, where we may follow

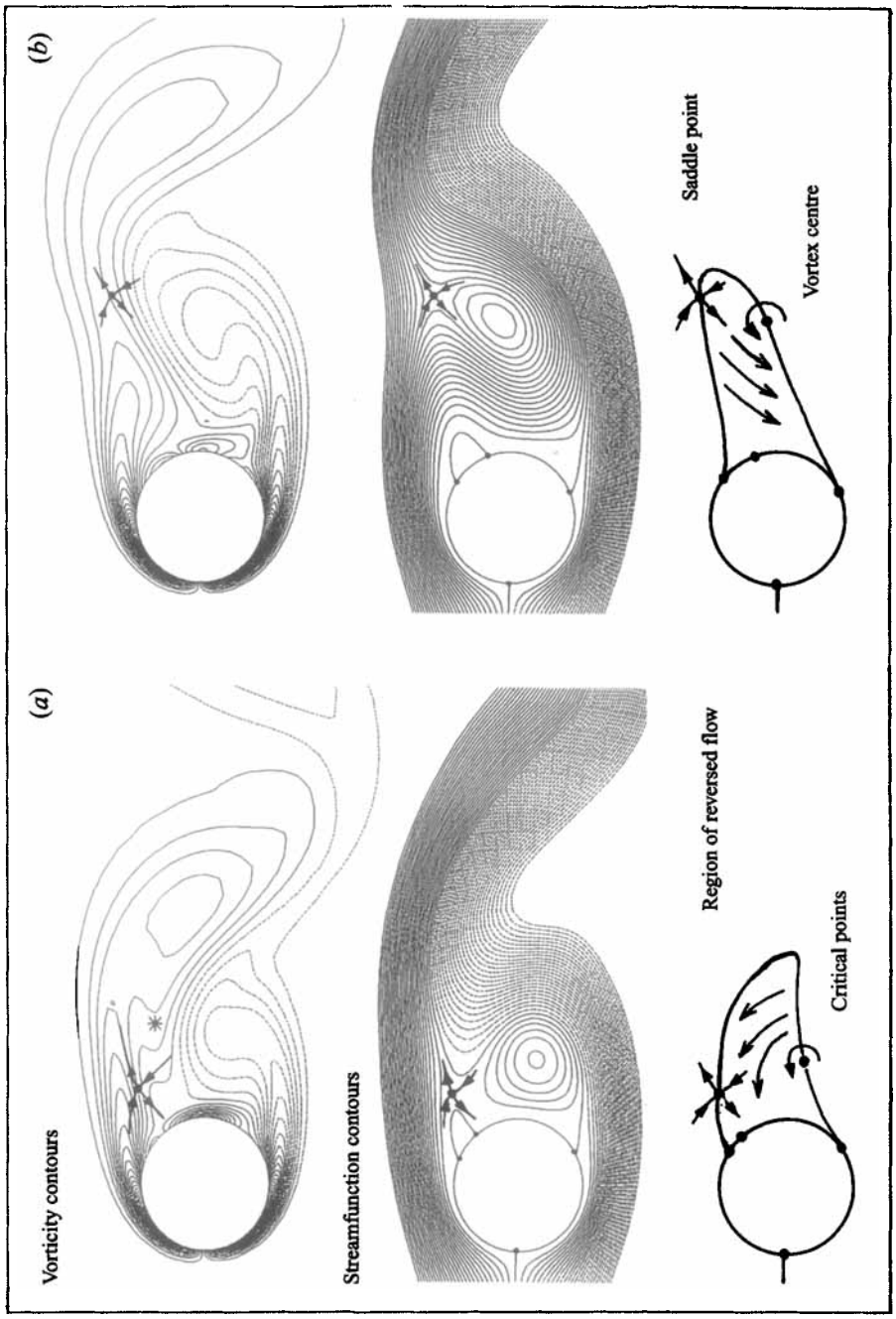

FIGURE 12. Vorticity, streamlines and reversed flow from two-dimensional direct numerical simulations. Simultaneous vorticity and streamline plots from 2D-DNS computations at $Re = 200$ are shown here, with instantaneous reverse-flow regions interpreted from the streamline plots included at the bottom. DNS from Karim Shariff (personal communication, 1990). The star in the vorticity plot of (*a*) indicates the segment of the primary vortex which is being pulled back upstream in the reverse-flow region. This demonstrates the deformation, or tearing, of Kármán vortices as they are shed from the near wake.

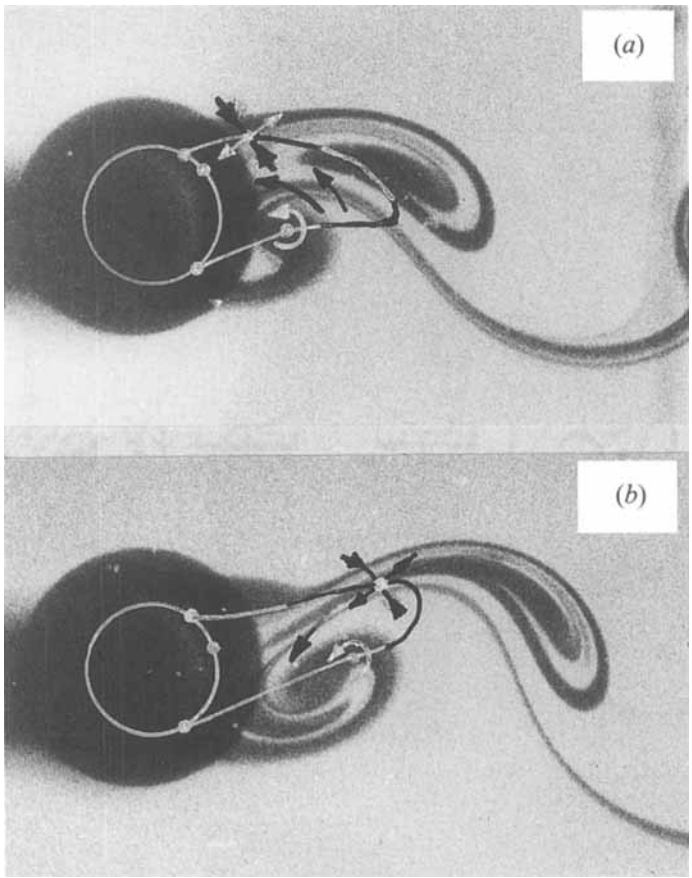

FIGURE 13. Superposition of reverse-flow region from the simulation onto dye visualizations, at the spanwise location of a vortex loop. This demonstrates experimentally the vortex deformation or tearing during shedding due to the placement of part of the primary vortex in the reverse-flow region of the near wake.

the loop, marked with the blob, deforming under the influence of the previous vortex loop. The sides of the loop, in the strong strain rate between primary structures, roll up to form a streamwise vortex pair. This deformation and stretching, also described in brief in Williamson (1988*b*), has also been confirmed by the numerical simulations of Mittal & Balachandar (1995*c*). Simultaneous images in cross-section and from side view can be seen in figure 11, by the use of a system of mirrors in the experiments. The sequence of cross-sectional views suggests that the loop segment of the primary vortex is located more towards the centreplane of the wake than the rest of the vortex, and appears to be pulled out of the primary vortex in a reverse-flow region behind the body.

The deformation, or indeed this 'tearing', of the primary vortex during shedding can be confirmed from a combination of experiment and direct numerical simulation. We shall look at the cross-sectional flow in figure 12 that is responsible for setting up the reverse-flow and strain-rate field, causing streamwise vorticity stretching, not only for mode A, but also relevant for mode B. Direct numerical simulations of the two-dimensional cylinder wake at $Re = 200$ were carried out by Karim Shariff at NASA Ames, and kindly made available in 1990 to the author (for computational details, see

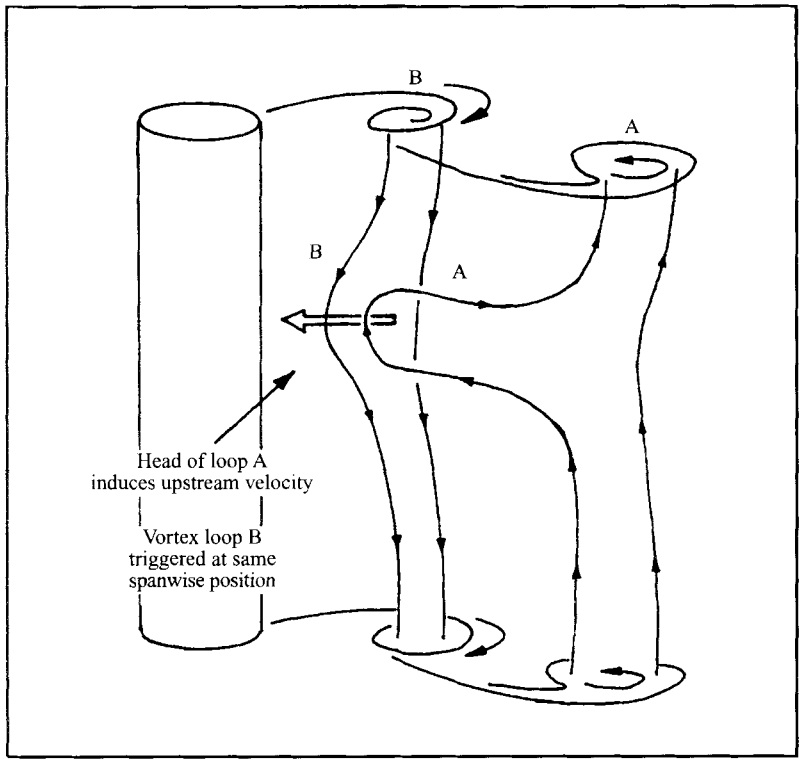

FIGURE 14. Physical mechanism to produce vortex loops of mode A. Segments of the primary vortex cores are pulled out of the primary structure as it is shed, and form an array of vortex loops. The self-sustaining formation of loops at a particular spanwise location is due to the Biot–Savart induction of one vortex loop on a newly forming primary vortex, as shown in the sketch. This produces the out-of-phase symmetry of the streamwise vortices for mode A, shown in figure 20.

Shariff, Pulliam & Ottino 1991). These simulations included 24 instances during a shedding cycle where simultaneous contour plots of vorticity and streamline patterns were computed, two of which are shown in figure 12. The saddle point of the streamline pattern has also been included in the vorticity plots to indicate where much of the streamwise stretching of vorticity is occurring. (This is further quantified in figure 22.) Regions of reversed flow in the lowest diagrams have been deduced from the streamline patterns. One may expect vorticity to be convected back towards the cylinder, against the free-stream direction, in these reverse-flow regions (noting that these are of course instantaneous patterns). Interestingly the reverse-flow region includes both of the critical points in the wake flow, namely the saddle point and the vortex centre, and it should be noted that the reverse-flow region extends downstream further than the saddle point itself.

The simulation in figure 12 shows evidence for vortex deformation or 'tearing', in the manner observed experimentally for both modes A and B. Part of the primary vortex marked * in (*a*) is being pulled back upstream during shedding, while the remaining segment of the primary vortex travels downstream. Vortex tearing during shedding is shown experimentally rather clearly in figure 13. In this case for $Re = 210$, we are viewing a particular cross-section which captures the formation of a vortex loop. (One should note, in such a visualization, that the dye is less diffused than the actual vorticity would be.) As precisely as possible, the corresponding vorticity contour plots from the numerical simulations have been placed over the photographs, and to

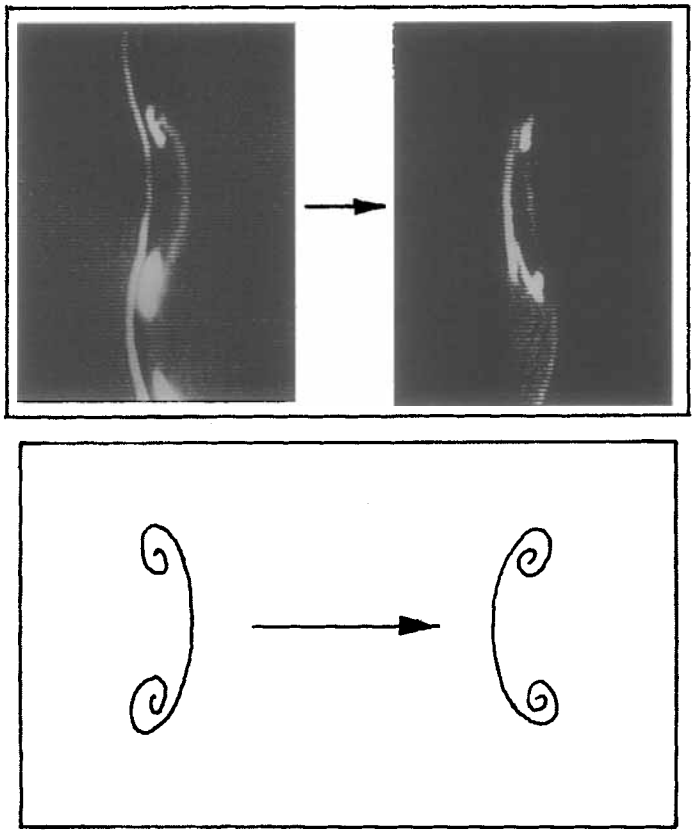

FIGURE 15. Video evidence of out-of-phase streamwise vortex symmetry for mode A. Each photograph, taken half a cycle apart, is extracted from video images looking upstream from behind the cylinder, and normal to a planar light sheet (at $x/D \approx 2$) in the near wake. The passage of fluorescent dye (washed off the body) passing through the sheet shows the distinct symmetries of the streamwise vortices. $Re = 200$.

the same scale, in order that the reverse-flow region can subsequently be drawn onto the photographs. In figure 13, one can clearly observe the tearing of the primary vortex, as a segment is caught in the reverse flow and convected back towards the body, while the remaining segment of the primary structure sheds downstream. This process is similar to the tearing of weak vortices that can often be observed in mixing layers (see Ho & Huerre 1984). Such vortex deformation, in the case of the wake, places significant primary core vorticity into the braid regions, where streamwise vortex stretching amplifies the three-dimensionalities. In the case of mode A, this deformation occurs at particular spanwise locations where vortex loops are forming, which will be further discussed below. For mode B, the deformation occurs more uniformly along the span.

The spanwise lengthscale of mode A is given by the spanwise waviness of the primary vortex cores, the origin of which will be discussed in §4.4. What is observed experimentally is that the first spanwise segments of the primary vortex to get 'caught' in the reverse-flow region during shedding will be the parts of the wave that are most upstream. In figure 14, we show the mechanism whereby these vortex loops are self-sustaining at the same spanwise location. A previously formed vortex loop A convects close to the shedding primary vortex B. The induced velocity due to the head of the loop A will retard a segment of the vortex B at the same spanwise position, by

Biot–Savart induction. From this segment, a vortex loop will be drawn out of the primary structure. The process will continue from one vortex to the next in a self-sustaining mode. From the sides of the loops, streamwise vortices will roll up, in a process which naturally causes an out-of-phase symmetry of the streamwise vortex array. Although most (but not all) of the streamwise vorticity for mode A comes from vorticity initially pulled out of the core into the braid region during shedding, the stretching thereafter occurs in a manner similar to the strong straining near the 'braid' saddle point in a mixing layer (Corcos & Lin 1984; Meiburg & Lasheras 1988).

In order to confirm the symmetry of the streamwise vortex structure of both modes A and B, we set up a video arrangement coupled with our water channel facility, which looks directly upstream and normal to a plane light sheet situated in the near wake of the cylinder. This experiment proved to be highly revealing, as follows. In the case of mode A, the video images taken half a cycle apart shown in figure 15 proved what was already deduced from the above, namely that the streamwise vortex structure for mode A follows an out-of-phase pattern of streamwise vortices. The symmetry of both modes A and B is shown schematically later in figure 20. In the following section, we shall find that the symmetry of mode B is quite distinct from that for mode A.

4.3. *Origin and symmetry of mode-B three-dimensional instability*

The instability of mode B would not appear to be related to a waviness of the primary vortex as in mode A, since these vortices deform much more uniformly along their length. In contrast with (long-wavelength) mode A, which scales on the larger primary vortex core dimensions, we shall show that the (small-wavelength) mode B scales on the smaller dimensions of the braid shear layer.

Mode B involves an instability with a wavelength of around $1D$, from Reynolds numbers of around 260 up to at least 10000, as given by the data of Mansy *et al.* (1994), Lin, Towfighi & Rockwell (1995*a*, *b*), Williamson, Wu & Sheridan (1995), and Chyu & Rockwell (1996). This roughly constant wavelength is consistent with the independence of spanwise scale found for turbulent mixing layers by Bernal & Roshko (1986). The laser-induced dye visualization in figure 16 shows the streamwise vortices when they are cut by a thin light sheet close to, and parallel with, the wake centreplane. The mushroom-like pattern comprises alternate-signed vortices in a row which resides in the braid region. The pattern indicates an almost spanwise-periodic system of vortex pairs representative of a range of $Re = 260$–300, with a wavelength of $\lambda_z/D = 0.98$ (in this case).

The symmetries of these wake patterns (A and B) are intimately linked to the fact that streamwise vortices formed in a previous half-cycle are in the vicinity of newly forming streamwise vortices. We can understand the mode-B symmetry (which we shall prove later has an in-phase streamwise vortex pattern) by considering the induced velocity of a periodic array of pre-existing streamwise vortices 'imprinted' onto a newly forming braid shear layer, as in the diagrams of figure 17. The velocity field due to the already-formed streamwise vortex array in braid A will be such as to induce a spanwise waviness in the newly forming braid shear layer B, and will lead to a preferred phase relationship for the new set of streamwise vortices, relative to the pre-existing set of streamwise vortices. To illustrate this point, let us consider the vortices in braid A as point vortices of strength Γ, with spanwise wavelength equal to λ, and with the origin through an anticlockwise vortex, as shown in figure 17(*b*). In the vortex array A, we may note that we have, for $n = 0, 1, 2, 3, \ldots$,

positive vortices at $\quad z = 0, \pm\lambda, \pm 2\lambda, \ldots = \pm n\lambda,$

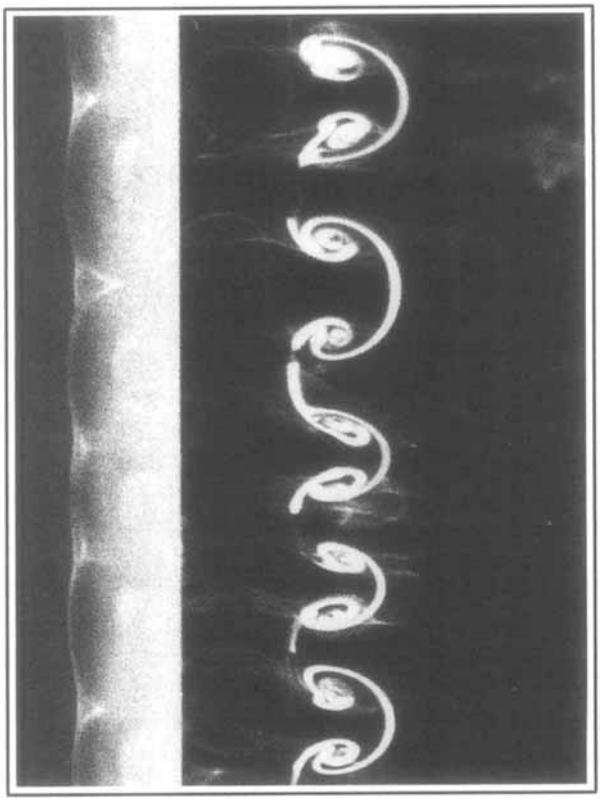

FIGURE 16. Cross-sectional view of mode-B streamwise vortex structure. We can see clearly the smaller-scale 'mushroom' vortex pair structures of mode-B vortex shedding, using laser-induced fluorescence. $\lambda/D = 0.98$; $Re = 300$. There is a remarkable similarity between this vortex array and that found in a mixing layer, Bernal & Roshko (1986).

negative vortices at $z = \pm\lambda/2, \pm 3\lambda/2, \ldots, = \pm(n+1/2)\lambda$.

The horizontal velocity (v) due to the vortex array in A may be given as

$$v = (\Gamma/\lambda)\cosh(2\pi y/\lambda)[\sin(2\pi z/\lambda)/\cosh^2(2\pi y/\lambda) - \cos^2(2\pi z/\lambda)] \quad (1)$$

which is well approximated, when braid B is horizontally separated by a distance $y = \lambda/2$ or more from the line of vortices in A, as

$$v = [(\Gamma/\lambda)/\cosh(2\pi y/\lambda)]\sin(2\pi z/\lambda). \quad (2)$$

The perturbation due to vortices in A could thus be well modelled as a sine wave in the manner sketched in figure 17(*b*). One now questions how this sinusoidally perturbed braid B will generate streamwise vorticity.

In order to determine the evolving system of streamwise vortices in the new braid shear layer B, one might naturally imagine that a spanwise undulation in such a shear layer is three-dimensionally unstable, much like the mechanism of Hama (1963), where a sinusoidally perturbed vortex filament becomes stretched into long streamwise vortices in a background shear flow. However, the limiting cases of oblique waves of angle 90° (our case here) on the limiting Stuart vortex array (a 'tanh' shear layer profile, representing our braid shear layer) is the only case in Pierrehumbert & Widnall's (1982) analysis which is not linearly unstable to the translative instability!

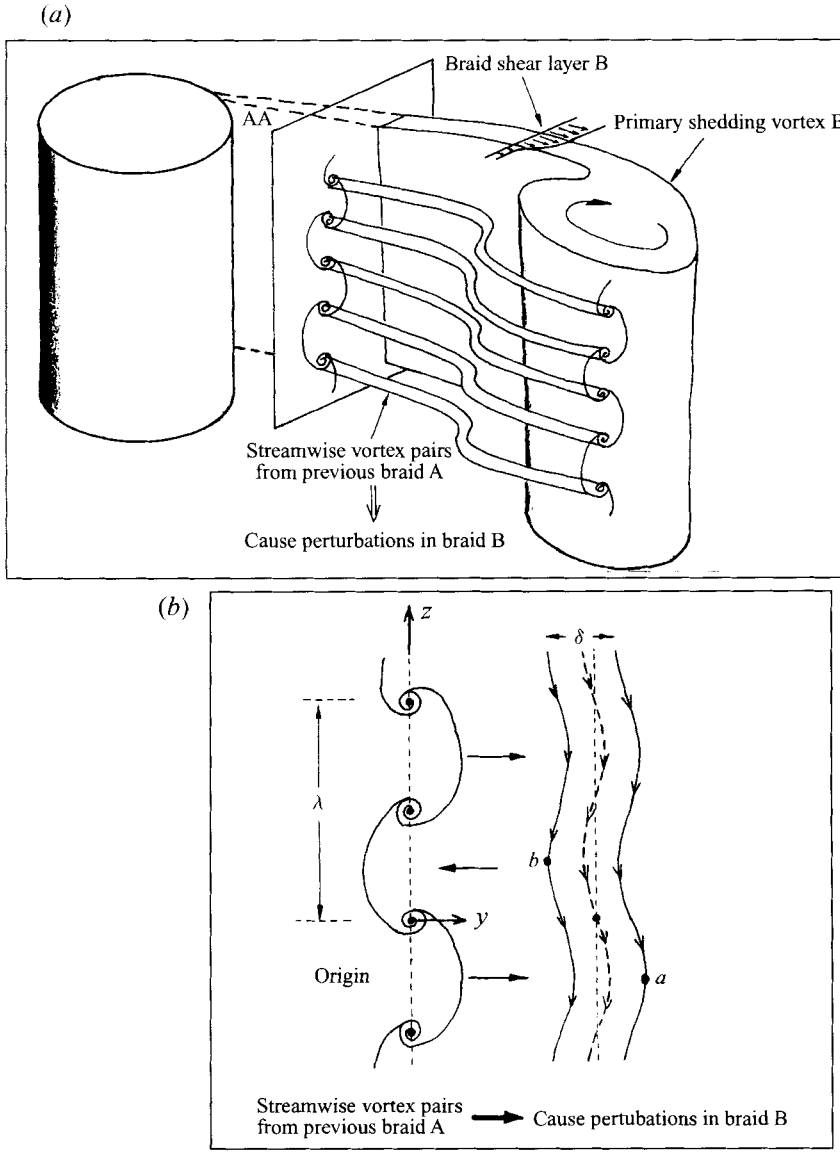

FIGURE 17. Physical mechanism in the braid shear layer to produce mode-B streamwise vortices: preferential phase relationship of streamwise vortices from one braid to the next. The presence of a previous array of streamwise vortices (A) close to the forming braid shear layer (B) causes spanwise perturbations on the new shear layer. Perspective view. (*b*) The line of vortices in braid A will cause spanwise waviness in the new braid shear layer in the manner shown. View looking upstream in section AA.

On the other hand, the presence of a saddle point (or line) in the braid shear layer does indeed ensure the three-dimensional instability, and the formation of streamwise vortices, as follows. We now consider a vortex filament in shear layer B in the neighbourhood of the saddle point (which could previously be noted in the cross-sectional simulations of figures 12 and 13). It may be observed that the saddle point extensional axis is rotated with respect to the shear layer, in just the same manner as found by Martin & Meiburg (1991) for the braid region of a jet, and this is shown in

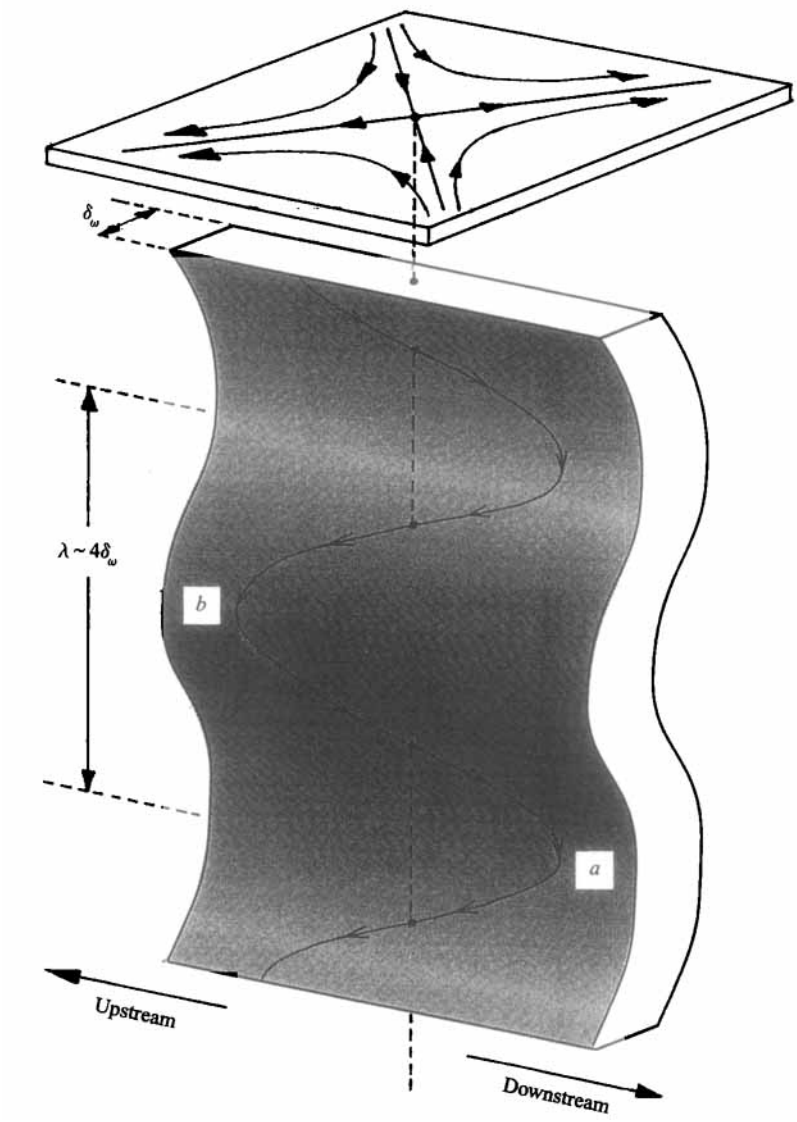

FIGURE 18. Amplification of streamwise vorticity close to tiled saddle point, for mode B. The initially vertical lines of the braid shear layer are perturbed by the previous braid vortices into a transverse (y) spanwise waviness (see figure 17). It is the presence of the cross-sectional saddle-point flow field that generates streamwise vorticity; point b is taken upstream, and likewise point a is taken downstream, causing the streamwise wavy vortex lines, as shown. Maximum streamwise + and − vortices will be generated opposite the same-sign original vortices in the previous braid. Thus the new braid vortices are a repeat of the old braid vortices, and we have an in-phase streamwise vortex pattern. In a sense, the old braid vortices imprint themselves into the new braid shear layer.

figure 18. The saddle-point flow, at the top of the figure, represents the cross-sectional flow field set up by the large primary vortices, which is acting at all horizontal cross-sections throughout the vertical extent of the braid. Point b from the perturbed shear layer of the previous figure is pulled towards us (in figure 18), into a region of the saddle-point flow which is moving fluid upstream. Likewise, point a is perturbed away from us, and is taken downstream by the saddle-point flow. In this manner, the initially vertical vortex lines in the braid shear layer become stretched into an approximate sine

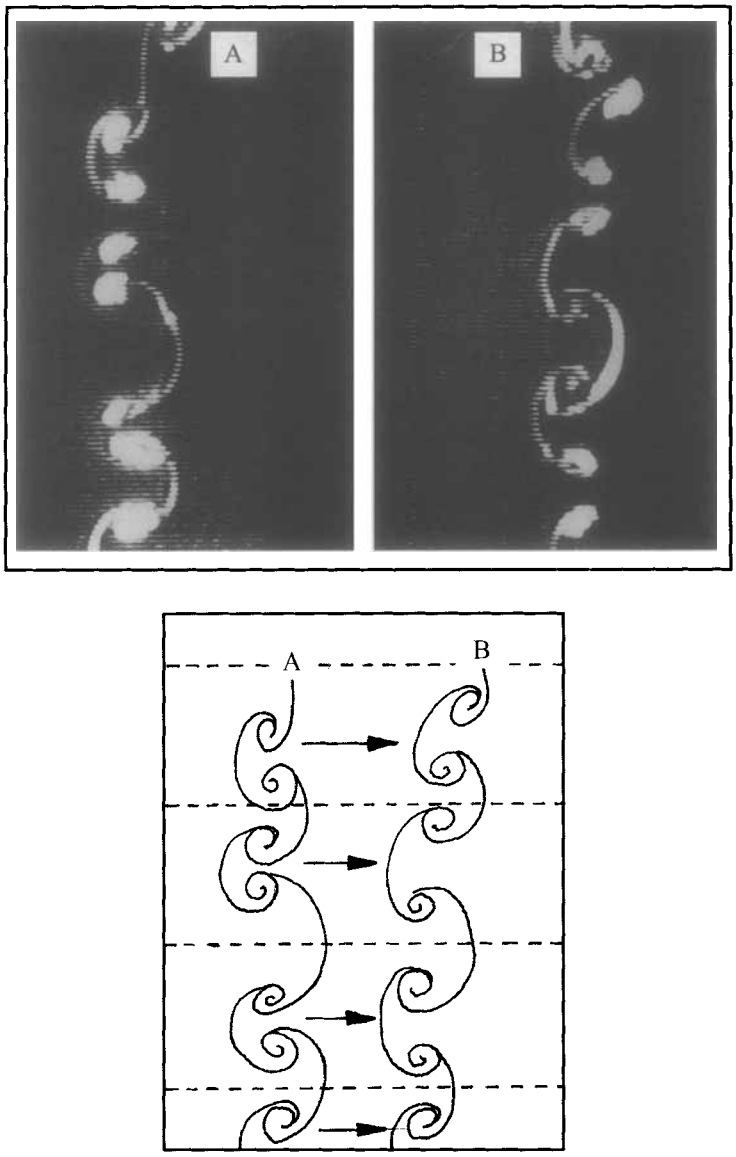

FIGURE 19. Video evidence of in-phase streamwise vortex symmetry for mode B. The photographs are taken half a cycle apart in the manner described for figure 15. $Re = 280$.

wave in the streamwise direction, as shown in figure 18. These vortex filament motions will also induce tilting and stretching of streamwise vorticity in the entire region of the shear layer in proximity to the saddle point, rather than simply right at the saddle point. Positive and negative streamwise vorticity is thus induced in the new braid shear layer, and it has a particular phase relation with the pre-existing streamwise vortices, as shown below.

The maxima in positive streamwise vorticity (as defined earlier, namely anticlockwise when looking upstream) will be where the vortex filament vector is most aligned in the streamwise downstream direction. An example where one of the maximum positive vortices in braid B will lie is where the vorticity vector is most directed downstream,

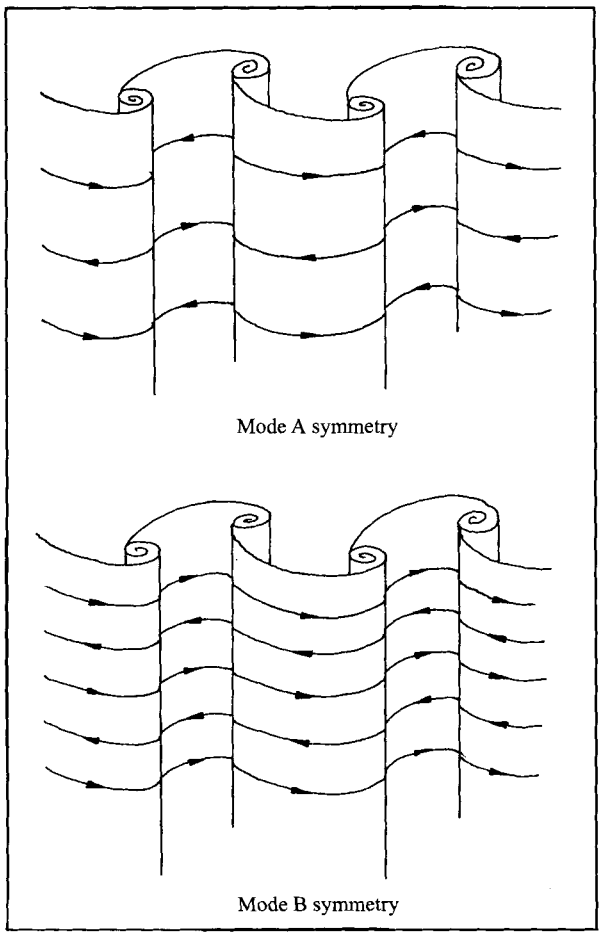

FIGURE 20. Symmetry diagrams of modes A and B. Mode A, of large spanwise wavelength, comprises an out-of-phase sequence of streamwise vortices from one braid to the next one. Mode B, of small spanwise wavelength, comprises an in-phase arrangement.

i.e. midway between points a and b in figure 18. If we now look back at figure 17, this is exactly opposite the positive vortex in braid A that was at the origin. Therefore the new vortex system in braid B is a repeat of the original braid vortex array in A, and we find that all the positive vortices are located as follows:

maximum positive vorticity in braid B at $z = \pm n\lambda$.

This is the same expression as used for the positive vortices for braid A earlier. The 'imprint' of one braid onto the next braid, coupled with the saddle-point flow will thus generate an in-phase pattern of streamwise vortices in the successive braids.

We show, in figure 19, two video images taken of the braid shear layer (in the manner of figure 15) half a cycle apart, clearly showing that mode B indeed yields an in-phase pattern of streamwise vortices. One vortex pair in braid A, for example, will be followed by the same vortex pair orientation on the next braid region B to form. Although there is some degree of spanwise (vertical) wandering of these pairs from one half-cycle to the next, a continuous running of the video on the screen monitor leaves no doubt regarding this symmetry. It should also be mentioned here, from studying carefully the video sequences, that subsequent to the growth of the new braid

streamwise vortices, which are a repeat of the previous set of braid vortices, the like-sign vortices in each braid system appear to amalgamate into a single set of braid streamwise vortices. There is thus a successive process of streamwise vortex amalgamation with each new braid to form, for mode B. The in-phase streamwise vortex pattern of mode B is presented diagrammatically in figure 20, and may be contrasted with the out-of-phase pattern of mode A.

In analogy with this repeating of streamwise structure from one braid onto another for mode B instability in the separated wake, one can then imagine that in the case of a splitter plate unseparated wake, if one has a corrugation or waviness at the trailing edge of the plate with this form of cross-stream shape (i.e. as for braid B in figure 17*b*), then one would expect to find an in-phase system of streamwise vortices. This is precisely what is found from the experimental/simulation study in Meiburg & Lasheras (1988), and in Lasheras & Meiburg (1990). In their mode 1 perturbation to the splitter-plate wake flow, with the above corrugations, they cause sine-wave disturbances to the flow in the cross-stream direction. In their figure 18, Meiburg & Lasheras write in their caption: 'Notice also the equal rotation sense of the streamwise vortices in the two consecutive braids'. The actual view shown in their figure looks remarkably like our video image in figure 19 for mode B. Their mechanism for the generation of streamwise vortices in their mode 1, involving the presence of the saddle point in the braid regions, is wholly consistent with our description given in this section.

4.4. *Mode A*: '*Elliptic instability*' *of the primary vortex cores*

The experiments in this paper provide clear evidence that mode-A instability scales on the primary vortex cores, and we shall present in this section further evidence, from theoretical considerations, that this mode is indeed a manifestation of an 'elliptic instability' of the vortex cores.

One may suggest that this mode-A instability has some similarities, in terms of the lengthscale and symmetry, with the translative instability in a mixing layer vortex array analysed by Pierrehumbert & Widnall (1982). They consider a shear layer, which has assumed an equilibrated state comprising an array of Stuart vortices (Stuart 1967), and for which they find streamwise structures arising from a secondary three-dimensional instability of this primary finite-amplitude flow. Their 'translative' mode of instability induces a spanwise waviness of the vortex cores, which is in-phase from one primary vortex to the next. The equivalent symmetry for the wake corresponds with our out-of-phase streamwise vortex pattern for mode A, shown in figure 20. The most unstable spanwise wavelength λ_z from Pierrehumbert & Widnall (for vortices typical of a shear layer) is given by $\lambda_z/\lambda_x = 0.62$, where λ_x is the primary wavelength. This value is close to the experimental measurements of Bernal & Roshko (1986) and Huang & Ho (1990) for a shear layer, who find broadly $\lambda_z/\lambda_x = 2/3$, but is also surprisingly close to the range of values $\lambda_z/\lambda_x = 0.6$–$0.8$ found in the wake (noting that λ_x is close to $5D$).

These studies suggest that the lengthscale for mixing layer instability comes from the instability of the primary vortex core, rather than the braid, even though the braid region is where much of the streamwise vortex stretching takes place. This viewpoint has the support of several investigators of the mixing layer, including experimentalists Nygaard & Glezer (1990), and Huang & Ho (1990), as well as analytical investigators, such as Corcos & Lin (1984), Pierrehumbert & Widnall (1982), and Pierrehumbert (1986). However it is believed by Lasheras & Choi (1988) and Bell & Mehta (1989) that the origin of the streamwise vortices comes from the braid. It has subsequently been pointed out by Rogers & Moser (1992) that the instability naturally involves both the core and the braid together. They also show evidence, beyond the stability analysis of

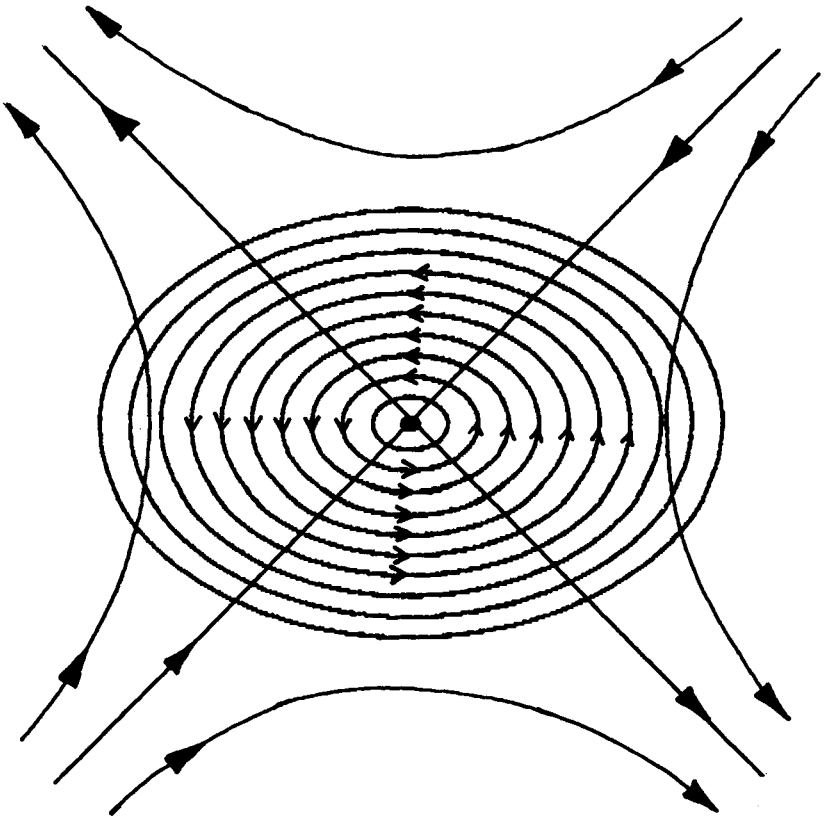

FIGURE 21. Elliptic flow streamlines. We note that the horizontal major diameters of the elliptic streamlines are oriented at $+45°$ with respect to the principal stretching axes. In this case, the uniform rotation is anticlockwise, and the principal stretching axes of the uniform strain rate at $-45°$ and $+135°$.

Pierrehumbert & Widnall, which shows that the lengthscale itself comes from the primary core instability, as described below. This is distinctly relevant to the mode-A wake instability.

Rogers & Moser have discussed the more recent work by Pierrehumbert (1986), Bayly (1986), Landman & Saffman (1987) and Waleffe (1990), all of whom have studied the three-dimensional stability of elliptic flow. Rogers & Moser then evaluate values of strain rate and vorticity at the centre of a Stuart vortex (in the periodic array of vortices), and input these values into the elliptic instability analysis for the single vortex by Waleffe, predicting $\lambda_z/\lambda_x = 0.61$. In other words, the elliptic-instability analysis for a single vortex in an array gives a most unstable spanwise wavelength essentially the same as that from the translative instability for the complete array. One may reasonably conclude from this, and from the results in Pierrehumbert (1986), that the elliptic instability of the primary vortices triggers the spanwise lengthscale for the ubiquitous streamwise vortices seen in the braids, in the absence of extrinsic effects from experimental facilities. From the above analysis for the mixing layer, one may suggest similarly that the spanwise wavelength for mode A in the wake corresponds to an elliptic instability of the primary vortex cores.

An elliptic instability represents the exponential growth of inertial waves in a flow with uniform vorticity and uniform strain, which occurs in the case when the perturbation vorticity remains aligned with the principal stretching axis (a result made

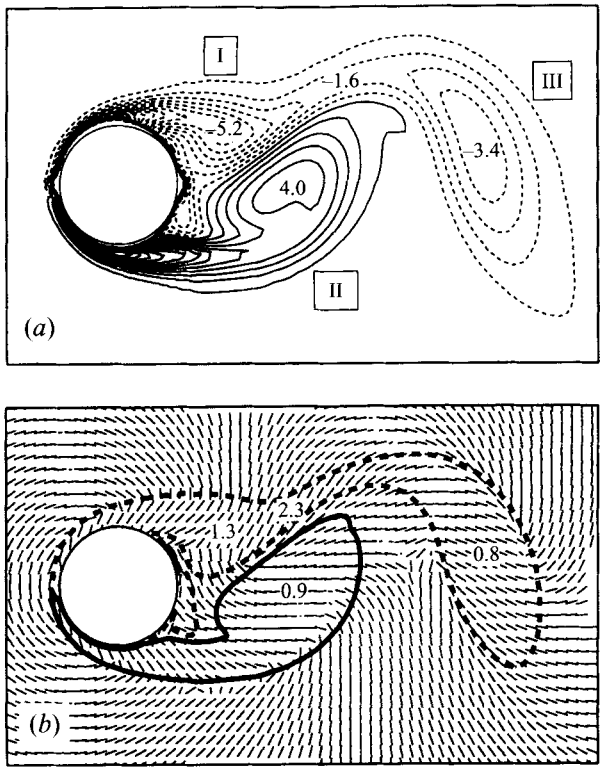

FIGURE 22. Vorticity and strain fields from two-dimensional direct numerical simulation of flow around a circular cylinder at $Re = 200$. (*a*) Vorticity contours at $\omega D/U = \pm 0.4, \pm 1.2, \pm 2.0, \pm 2.8 \ldots$. Numbers indicate local extrema. (*b*) Directions of principal stretching axis. Numbers show typical values of the strain rate. (These data are kindly provided by Helene Persillon, and have been manipulated and plotted by Thomas Leweke, both at Cornell.)

clear by Waleffe 1990). A flow with elliptic streamlines is generated when there is uniform rotation γ (which is half the vorticity $= \omega/2$), and uniform strain rate ϵ, and where the velocity components are

$$\left.\begin{array}{lll} u = -\gamma y & u = -\epsilon y & u = -(\gamma+\epsilon)\,y \\ v = +\gamma x & v = -\epsilon x & v = (\gamma-\epsilon)\,x \\ \text{Uniform rotation} + \text{Uniform strain} \Rightarrow \text{Elliptic flow} & & \end{array}\right\} \tag{3}$$

A useful sketch of this flow is given in figure 21. The rotation is in the anticlockwise direction, and the principal stretching axis is in the $-45°$ (and $+135°$) direction. The streamfunction given by

$$\Psi = -\tfrac{1}{2}\gamma(y^2+x^2) - \tfrac{1}{2}\epsilon(y^2-x^2)$$

defines ellipses whose major axis is horizontal, and at $+45°$ with respect to the stretching axis (rather than aligned in the stretching direction), as seen in figure 21. The aspect ratio (or eccentricity) of these ellipses is given by $\alpha = [(\gamma+\epsilon)/(\gamma-\epsilon)]^{1/2}$, and the ratio of strain to vorticity is defined by $\beta = (\epsilon/\gamma) = (2\epsilon/\omega)$. Elliptic flow ensues if $0 < \beta < 1$. The value $\beta = 0$ refers to circular rotating flow, while $\beta = 1$ refers to planar Couette flow.

We now observe the two-dimensional base flow of the cylinder wake from direct numerical simulation (data kindly made available by Helene Persillon, and plotted by Thomas Leweke, both at Cornell). It is distinctly relevant that the roughly elliptical region of high vorticity II in figure 22(*a*) is associated with a principal stretching axis,

shown in (*b*), which is aligned at 45° to the major axis of the ellipse. A similar situation is found for regions I and III. A flow field such as in II satisfies the conditions of the 'elliptic' instability, and may be compared with the sketch of elliptic flow in figure 21. (Of course, one is concerned in the real flow with a finite vortical region, not unbounded as in the present theories, and with only a roughly uniform-vorticity region.) In the present case, streamlines are not a good indicator of ellipticity, due to the unsteady two-dimensional flow field, although this point is further addressed below. However, in the case of vortex II, we find

$$\omega D/U \approx 3, \quad \epsilon D/U \approx 0.9, \quad \alpha \approx 2 \tag{4}$$

and the lengthscale (minor diameter) of the vortex region is of order $1D$. The values of strain and vorticity yield a value of $\beta \approx 0.6$, which indeed signifies an elliptical flow.

It is important to introduce further the elliptic flow instability in the present context, as follows. In the case of a circular (inviscid) rotating flow, and if we rotate with the base flow, i.e. take a reference frame rotating with angular velocity $= \gamma$, then the base flow is reduced to rest, and the small velocity perturbations $\boldsymbol{u}$ on this flow are governed by

$$\mathrm{d}\boldsymbol{u}/\mathrm{d}t = -2\boldsymbol{\Omega} \times \boldsymbol{u} - (1/\rho)\,\boldsymbol{\nabla} p, \tag{5}$$

$$\boldsymbol{\nabla} \cdot \boldsymbol{u} = 0. \tag{6}$$

where p represents what is known as 'excess' pressure. The first term on the right-hand side of (5) is the Coriolis force, and is the term which gives rise to waves known as inertial waves, in this rotating fluid. Our base flow, in the present example, has circular streamlines in the (x, y)-plane, and thus has a rotation around the z-axis: $\boldsymbol{\Omega} = (0, 0, \gamma)$. We can obtain a physical understanding of the problem of inertial waves by considering the following example. If we consider, for the moment, a particle moving as a result of a disturbance in the (x, y)-plane only, with a velocity $\boldsymbol{q} = (u, v, 0)$ (and not in this case representing a genuine fluid motion) then there will be a Coriolis force in the (x, y)-plane on this particle $= -2\boldsymbol{\Omega} \times \boldsymbol{u} = 2q\gamma$, acting in a direction perpendicular to velocity q, regardless of its direction in this plane. Thus the particle moves in a circle, with angular frequency $\omega^* = 2\gamma$. (The above illustration is included in Tritton 1988.) What is also particularly interesting is that this particle will counter-rotate relative to the base flow rotation. Similarly, it may be shown that a plane wave, whose wavenumber is along the z-axis (i.e. where all the particles in a given (x, y)-plane move in unison in circles), satisfies the disturbance equations for this rotating base flow, yielding the same frequency, $\omega^* = 2\gamma$. More generally for a wave given by

$$\boldsymbol{u}(x, t) = \tilde{\boldsymbol{u}} \exp[\mathrm{i}(\boldsymbol{k} \cdot \boldsymbol{x} - \omega^* t)], \tag{7}$$

where the wavenumber vector is at some angle, θ, to the z-axis, then the angular frequency of these waves, ω^*, which is governed by the disturbance equations (5), (6), is given as

$$\omega^* = 2\gamma \cos\theta. \tag{8}$$

Physically, in each plane normal to the wave vector, the particles again move around in circles, counter-rotating relative to the base flow. Inertial waves exist only with frequencies from zero up to 2γ. If we now consider the inertial frame of reference, the wave vector $\boldsymbol{k}$ will move with the circular rotating flow, with a constant angle θ to the z-axis. The counter-rotation of the particles in each plane normal to the (rotating) wave vector is the direct result of the Coriolis force.

In the presence of uniform strain, which then yields the elliptic flow, as considered by Pierrehumbert (1986), Bayly (1986), Landman & Saffman (1987), Waleffe (1990), and also included briefly as one of a number of cases by Craik & Criminale (1986), a certain range of these inertial waves are not neutrally stable, as they all are in circular

rotating flow. For small strain, there exists a small range of wavenumber vectors close to $\theta = \frac{1}{3}\pi$ which are unstable. Physically, this corresponds to the case when $\omega^* = \gamma$. With this frequency relationship, for small strain, the inertial waves are destabilized via a subharmonic instability from the imposed ellipticity (further discussed by Huerre & Rossi 1996). Waleffe has made clear a physical interpretation that, when the clockwise rotation of the velocity vector of the waves is equal and opposite to the anticlockwise rotation of the wave vector itself around the z-axis (i.e. when $\omega^* = \gamma$), then one can choose initial conditions such that the average perturbation vorticity is, and remains, in the principal stretching direction of the strain field. An exponential growth of these waves then follows. One may note that, in the elliptic flow case, the wave vector precesses around the z-axis along an elliptic path which is normal to, but the same shape as, the base flow streamline ellipse.

Waleffe has superposed the individual wave Fourier modes to construct localized solutions, which for small strain, consist of Bessel function expressions for the perturbation velocities and vorticities, and thereby it is found that the perturbations decay roughly with $1/(\text{radius})^{1/2}$ as one moves away from the z-axis. It is rather difficult to visualize the ensuing elliptic instability (in order to relate it to the present physical situation of the wake vortices) without plotting the streamlines of the flow resulting from the growth of the inertial waves. This has been done in figure 23 (plotted by Thomas Leweke at Cornell; see also Leweke & Williamson 1996*a*) for the analytical expressions based on weak strain from Waleffe. The structure of the perturbation results in a displacement of the centre of rotation (for the resultant flow in (*c*) = base flow + perturbation) in the direction of the principal stretching axis. The inner and outer vortex layers (inside or outside of the bold circle, defining an 'invariant' streamline) are displaced in opposite radial directions. The flow pattern is modulated in the spanwise direction with a wavelength that depends on the eccentricity (α) of the elliptic flow. For small strain this modulation has a wavelength close to twice the diameter of the invariant streamline. For comparison with the present experiments, we also show in figure 23(*d*), the deformations of initially concentric material surfaces, visualized in the plane of principal stretching. In the present problem, such waviness is clearly visible in the vortex cores of near-wake vortices, in the early stages of flow development when the cylinder is started from rest in a towing tank, an example of which is included in Leweke & Williamson (1996*a*). The elliptic instability theory shows that the spanwise waviness of the core of an elliptical vortex region will be in the direction of principal stretching, which from the numerical simulation in figure 22, will be in the upstream–downstream direction. If one looks at the cross-sectional picture of the near-wake vortex in figure 11(*a*), this also appears to be the case. However, one should note that the flow visualization in this case principally shows the mode-A instability well into its nonlinear development.

In inviscid flow, for a given shape of the elliptic streamlines (for a given eccentricity), all wavelengths have the same growth rate. However, one can deduce discrete wavelengths if one imposes the condition that the invariant streamline (which is actually a tube with elliptic cross-section) will fit into a given finite vortex, which was a condition used by Rogers & Moser for the mixing layer Stuart vortex, employing the results for weak strain from Waleffe (1990, pp. 79–80). If one does this for the near-wake vortex II, one finds that the growth rate (σ) and most-unstable spanwise wavelength (λ) of the elliptic instability are given as

$$\sigma D/U = (9/16)(\epsilon D/U)(1-\beta^2)^{1/2} \approx 0.405, \tag{9}$$

$$\lambda \approx 2D_{MIN} \approx 2\text{D}, \tag{10}$$

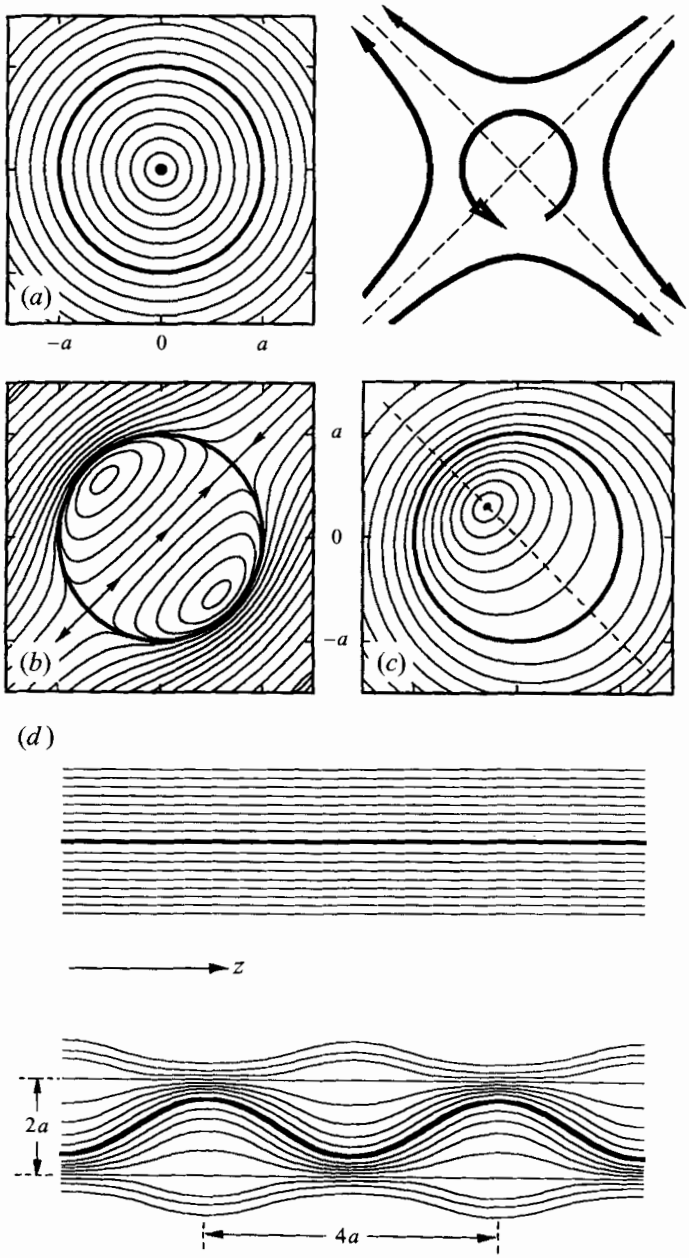

FIGURE 23. Effect of the elliptic instability on the streamlines of an elliptical flow, shown for the asymptotic limit of vanishing strain rate. (*a*) Base flow (solid rotation). (*b*) Perturbation due to the inertial waves (from Waleffe 1990). Its characteristic lengthscale (wavelength) in this plane is $2a$. (*c*) The resultant total flow, indicating clearly the displacement of the centre of rotation out along the principal stretching axis. The bold line shows the streamline that remains unchanged under the perturbation (described as the 'invariant streamline' in the text), and the dashed line indicates the plane that is shown in (*d*). (*d*) Schematic representation of the vortex deformation in the plane of maximum strain rate. The upper diagram shows the initial situation with concentric vortex layers. The lower diagram shows the vortex perturbed by the elliptic instability. The thick line shows the centre of rotation, which is periodically displaced along the stretching axes with wavelength λ.

where D_{MIN} = minor diameter of the elliptic vortex. We shall find that this growth rate is reasonably correct, based on further results below. This approach also yields a spanwise wavelength of the right order, as found for mode-A instability. However, our analysis is based on an inviscid flow, and in fact the choice of the largest discrete wavelength from Waleffe's results is arbitrary, in that there exist smaller discrete wavelengths, if we scale down other larger invariant streamline tubes into the finite elliptical vortex. Further to this, the value of $\beta = 0.6$ in our wake case is not close to the conditions for small strain (small β). Following the first version of this paper, the author has indulged in much discussion over elliptic instability in wakes with Thomas Leweke at Cornell, and this has directly led to two of the present figures (22 and 23), and indeed to a further letter (Leweke & Williamson 1996*a*). It appears that the key to deducing a reasonable estimate for the spanwise wavelength and growth rate in the present problem is the inclusion of viscosity in the analysis, which has been mentioned by several authors, although it is the paper of Landman & Saffman (1987) which explicitly demonstrates the effects on the instability of including viscosity.

Including viscosity in this problem has two essential effects. First, it yields a cut-off lengthscale below which the elliptic instability is not unstable. Secondly, and quite significantly, the effect of viscosity leads us to predict that the largest wavelength, in a given problem, is the most unstable. These points are discussed with reference to the problem at hand, as follows.

Landman & Saffman (1987) show usefully, in their figure 1, the maximum inviscid growth rate $\sigma_{INVISCID}$ versus the strain parameter β, and demonstrate that although the cases $\beta = 0$ (circular rotating flow) and $\beta = 1$ (planar Couette flow) are stable, there is a maximum instability for $\beta = 0.8$. This is relevant to the near-wake vortices, where $\beta \approx 0.6$ typically, suggesting a rapid growth of instability in our case. When viscosity is included in the analysis, as in figure 2 of Landman & Saffman, in the form of Ekman number, E, versus β ($E = 2\pi\nu k_0^2/\gamma$, where ν is viscosity, k_0 the spanwise wavenumber of the instability), then it is immediately seen that for a given β, the growth rate increases as one decreases Ekman number, with a maximum growth rate for the inviscid case (horizontal axis in their figure 2). This trend is seen clearly from the following total growth rate expression (noting that θ is the minimum angle of the wave vector, which actually precesses around an elliptic path):

$$\sigma_{TOTAL} = \sigma_{INVISCID} + \sigma_{VISCOUS}, \tag{11}$$

$$\sigma_{TOTAL} = \sigma_{INVISCID} - \nu k_0^2[1 + \tfrac{1}{2}(\alpha^2 - 1)\sin^2\theta], \tag{12}$$

or normalized with respect to wake quantities,

$$(\sigma_{TOTAL} D/U) = (\sigma_{INV} D/U) - 4\pi^2 Re^{-2}(\lambda/D)^{-1}\cos^{-2}\theta[1 + \tfrac{1}{2}(\alpha^2 - 1)\sin^2\theta]. \tag{13}$$

The total growth rate increases, for a given value of viscosity (or Re) and given ellipse aspect ratio (α), as the lengthscale of the instability increases. In a finite size vortex, the most unstable wave will be the largest that can be fitted into the vortex. Although this is not a surprising result, since one expects that the smallest waves will be the most damped by viscosity, it is nevertheless a significant point.

The second principal effect of viscosity is the imposition of a viscous cut-off length for the perturbation, below which the elliptic flow is stable. One can think in terms of a critical Ekman number, E^*, for marginal stability, for which $\sigma(E^*, \beta) = 0$. The existence of a short-wavelength viscous cut-off means that the region of elliptical flow must be larger than a minimum size for the instability to manifest itself. The instability lengthscale L ($= 2a$ in figure 23) in the (x, y)-plane perpendicular to the rotation axis, is given by

$$L = 2\pi/[k_0(1 + \alpha^2)^{1/2}\sin\theta_m]. \tag{14}$$

We can deduce the critical length L^* from the relation $E^* = E(L^*)$, and using equations (4), (14):

$$L^* = 4\pi^{3/2} D [\sin^2 \theta_m (\omega D/U) Re (1+\alpha^2) E^*]^{-1/2} \approx 0.5D. \quad (15)$$

The elliptical region II in figure 22 therefore has a size $L \approx D > L^*$, which is large enough to support unstable disturbances. (The parameter θ_m is the most unstable wave vector angle, which for $\beta = 0.6$ in Landman & Saffman, figure 3, gives $\theta_m \approx 53°$). With the non-dimensional parameters for the vortex in the near wake varying only slowly with Reynolds number, the critical length varies roughly as $Re^{-1/2}$, in other words it decreases with Re. The fact that at $Re = 200$ the critical length is of the same order of magnitude as the sizes of the different elliptical regions in the two-dimensional wake is consistent with the fact that the critical Re for the three-dimensional transition is found in this range.

It is important to consider the growth rate for the near-wake vortices, and its relation to the characteristic time of the periodic base flow. The vortices of figure 22 retain their elliptic shape for at least one shedding period, $T = D/US$, where the Strouhal number S equals roughly 0.2. We can deduce that $E \approx \frac{1}{4}E^*$, using the fact that the elliptical region is about twice the critical length L^*, and that $E \sim L^{-2}$. From figure 2 of Landman & Saffman, for our case $\beta \approx 0.6$, we find $E^* \approx 1$, so that $E \approx \frac{1}{4}$, and the non-dimensional growth rate is thus $2\sigma/\omega = 0.25$. Normalizing with respect to wake parameters gives $\sigma D/U \approx 0.375$, which is reasonably close to the earlier estimate given from Waleffe's weak strain analysis, equation (9). Using the fact that $S \approx 0.2$, we find $\sigma T \approx 2$, which means that the instability will grow by a factor 10, while instability conditions are favourable. Considering the feedback mechanism found in this paper, whereby the waviness grows from one primary vortex to the next until vortex loops are formed, the elliptic instability discussed above is sufficient to trigger ultimately the appearance of the nonlinear mode-A instability.

One of the significant results to come from the theoretical analysis of elliptic instability in the near wake is the prediction of spanwise wavelength. The spanwise wavelength is related to the magnitude k_0 of the three-dimensional wave vector by $\lambda = 2\pi/(k_0 \cos \theta_m)$, which when divided by L using equation (14), gives a value for the 'aspect ratio of the instability', from which we find

$$\lambda = L(1+\alpha^2)^{1/2} \tan \theta_m \approx 3D. \quad (16)$$

This final result appears to be in good agreement with the measured spanwise wavelengths for mode-A instability in figure 9(*b*).

The above approximate accordance of predicted and measured instability wavelengths could be interpreted to indicate that the mode-A wake instability is triggered by an elliptic instability within the primary vortex cores. However, presentation of these considerations has met with some useful and important suggestions from Maurice Rossi of Universite Paris VI, Jean-Marc Chomaz and Patrick Huerre of Ecole Polytechnique, and Stephan Le Dizes of Marseilles (all private communications, 1996). One question concerns the inclusion of viscosity in the discussion of elliptic instability here, and whether viscosity has any effect on the results. It was reasonably suggested by Chomaz that the growth rate is relatively independent of wavenumber (for low values of $k_0 D$, the growth rate would have a 'plateau'), and thereby would not favour the growth of the largest wave. It should thus be pointed out here, for clarity, that the relationship between σ and k_0 has a parabolic form, and equation (12) yields, for $Re = 200$,

$$(\sigma D/U) = 0.465 - 0.00978\ (k_0 D)^2. \quad (17)$$

The range of possible unstable wavenumbers that would be smaller than the cut-off value, yet larger than that corresponding to the finite vortex size limit is given by $3.5 < (k_0 D) < 7.0$, which is a range that falls on a reasonably steep part of the growth rate curve, clearly favouring smaller wavenumbers (larger wavelengths). Viscosity would seem to remain important in the selection of unstable wavelengths. (It should be mentioned that one expects that for very small $k_0 D$ the growth rate will diminish, as it does for the Stuart vortex array (Pierrehumber & Widnall 1986; Brancher & Chomaz, private communication, 1996).)

It was further kindly pointed out by Maurice Rossi that the order of magnitude argument which led to $\lambda \approx 3D$ in equation (16) was perhaps too precise in the light of the fact that one does not know precisely how the lengthscale of the perturbation, L, will relate to the diameter of the finite-size vortex. In the case of the Rankine-type uniform vortex, Kelvin (1880) shows that the first zero of a neutrally stable Bessel function disturbance has a diameter D_{INV} (defining the invariant surface) which is 0.6 of the vortex diameter, for his first mode of vortex inertial waves. It is nevertheless clear that the major problem for the present case is that one does not know the precise relationship between D_{INV} and the cross-sectional dimensions of a *distributed* vortex. However, our very recent experimental results from elliptic instability in vortex pairs (Leweke & Williamson 1996*b*) clearly yields such a relationship, from which it appears one may reasonably predict instability lengthscales in the present wake problem.

We shall first use a more precise estimate for the cross-sectional lengthscale of the disturbance (D_{INV}), rather than the order of magnitude value, taken from Landman & Saffman, in equation (14). The wave vector of the disturbance is given by

$$\boldsymbol{k} = k_0[\sin\theta,\ \alpha\sin\theta,\ \cos\theta]. \tag{18}$$

Using the result from Waleffe (1990, p. 80) for the first zero of the Bessel function disturbance, we have an estimate for the dimensions of the invariant streamline (D_{INV}) in the minor axis (Y) direction:

$$(k_0 \alpha \sin\theta)\, D_{INV} = 5.47, \tag{19}$$

giving an aspect ratio of the disturbance given as

$$(\lambda / D_{INV}) = (\pi/2.735)\,\alpha\tan\theta = 3.05 \tag{20}$$

using previous values for the variables (α, θ). In the study of elliptic instability of an interacting vortex pair of Leweke & Williamson (1996*b*), it has been found possible to measure *directly* the value of D_{INV}, as well as to undertake velocity field measurements, which yield accurately the diameter at which the circumferential velocity is a maximum (D_{MAX}). We find the ratio as

$$(D_{INV}/D_{MAX}) = 0.92. \tag{21}$$

It is found that the (Oseen-like) vortex velocity distribution within the vortex pair problem and in the near wake are similar (in both cases, the vorticity in the minor-axis direction is well represented by a Gaussian distribution), indicating that a similar relationship will hold for the near-wake vortex II (of figure 22). If one looks at the streamline pattern of figure 24(*a*), it is clearly not possible to infer much for the velocity distribution of near-wake vortices. If, on the other hand, one subtracts the velocity at the centre of vortex II from the whole flow field, in (*b*), as carried out by Thomas Leweke (using the data of Helene Persillon), then the vortex becomes strikingly elliptic with an aspect ratio of close to 2, and with a minor-axis diameter (D_{MAX})

$$(D_{MAX}/D) = 1.03. \tag{22}$$

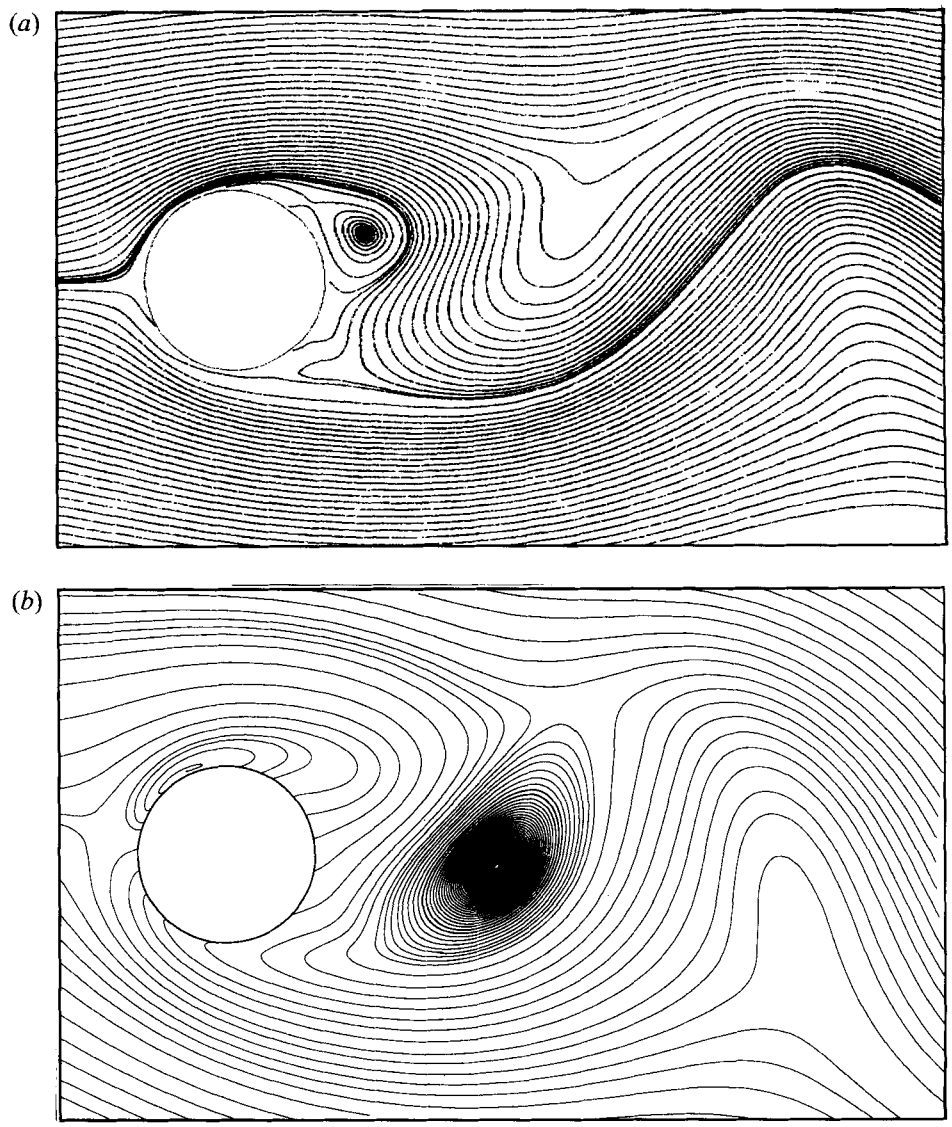

FIGURE 24. Streamlines for Reynolds number of 200. In (*a*) we show the streamlines which suggest very little information regarding the near-wake vortices. If, however, we subtract the velocity of the centre of vortex II from the whole flow field, the result in (*b*) shows a striking elliptic vortex from which we can make measurements. This plot is made by Thomas Leweke, from data kindly supplied from DNS by Helene Persillon and Marianna Braza.

We are now in a position to make a more precise prediction of the spanwise wavelength of elliptic instability by combining equations (20), (21) and (22), as follows:

$$(\lambda/D) = (\lambda/D_{INV})(D_{INV}/D_{MAX})(D_{MAX}/D) = 2.9, \tag{23}$$

although in view of the obvious assumptions made, the best we can predict is that

$$(\lambda/D) \approx 3, \tag{24}$$

again giving a predicted wavelength in good agreement with those values measured for the mode-A instability. In this case, however, we have a firm footing upon which to

base the relation between instability lengthscale and the vortex dimensions. In summary, it would appear from both experimental and analytical work that the spanwise lengthscale of mode A is indeed caused by an elliptic instability of the primary vortex core in the strain field of neighbouring structures in the near wake.

4.5. *Mode B: Instability of the 'braid' shear layer*

The instability mode B is quite distinct from mode A, and is shown to be an instability of the braid shear layer region, as observed in §4.2. This region of the flow is hyperbolic, and from the upper braid of figure 22, has a maximum ratio of strain to rotation $\beta \approx 2$. Before a discussion of theoretical prediction of the mode-B scale based on the braid instability, let us consider the relationship between spanwise wavelength (λ) and the vorticity thickness (δ_ω) of the separating shear layer, for the mode-B instability. Measurements of the shear layer vorticity thickness at $x/D = 1.0$, over a wide range of Re (Williamson, unpublished results, 1988) give

$$\delta_\omega/D = 4.2/Re^{1/2}. \tag{25}$$

For $Re = 280$, we find $\delta_\omega/D \approx 0.25$, and for $\lambda_z/D \approx 1.0$ as given from figure 9,

$$\lambda_z \sim 4\delta_\omega. \tag{26}$$

Since the above estimate is based on mean velocity profiles for the separating shear layers, it is an overestimate of the layer thickness at any instant, because the shear layer is flapping back and forth transversely. Instantaneous (δ_ω/D) may be estimated from the simulations of figure 12, again giving a value of around $\frac{1}{4}$.

Based on a knowledge of other shear flow instabilities, a wavelength $\lambda_z \sim 4\delta_\omega$ seems of the right order as an 'expected' most unstable wavelength. One would perhaps not expect, for example, λ_z to be less than $1\delta_\omega$ or greater than $10\delta_\omega$. That the most unstable wavelength in the braid is of order $\lambda_z \sim 4\delta_\omega$ is not actually predicted by any existing theoretical study, to the author's knowledge. It may be recalled that the analysis of streamwise vorticity in a braid strain field by Corcos & Lin involves a predetermined or imposed spanwise wavelength on the braid vortices, which does not originally come from a stability analysis. An analysis which takes into account the originally spanwise vortex lines, perturbed in the manner found in the present experiments, and in the presence of a saddle-point flow, has been discussed with Peter Schmit (University of Washington, personal communication, 1995–1996). Since such analysis is rather unwieldy, the approach of Peter Schmit is to analyse the counterpart of the elliptic flow instability, namely the hyperbolic flow instability (see also Lagnado, Phan-Tien & Leal 1984), in the presence of unbounded uniform strain and rotation, but where the strain dominates ($\beta > 1$). Such an analysis, which has also been suggested by Rogers & Moser (1992) and Robert Moser (University of Illinois, personal communication, 1996), should provide a useful comparison with the present experimental measurements of mode-B instability.

As a final point, it is worth stating that Corcos & Lin (1984) show that the instability of a shear layer that is strained in the direction of the principal vortices (i.e. parallel with the vorticity vector) yields a most unstable wavelength close to that without the superposed strain. Without superposed strain, the observed spacing between like-signed vortices is of the order of $\lambda \sim 3\delta_\omega$, as found by Brown & Roshko (1986), based on a number of different studies. A system of counter-rotating vortices (as found in a braid) might be expected to have a spacing of twice this value, if one assumes that each vortex has the same cross-sectional aspect ratio as for the same-sign vortex array, thus

$$\lambda_z \sim 6\delta_\omega. \tag{27}$$

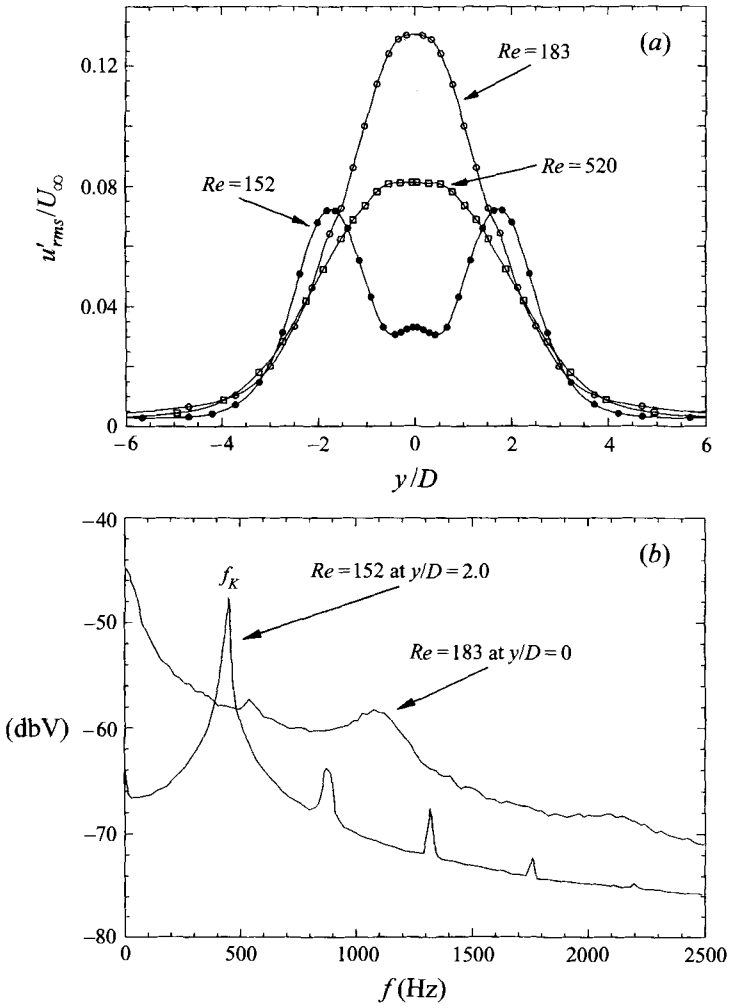

FIGURE 25. Wake fluctuation profiles and spectra in the transitional wake. (*a*) RMS velocity fluctuation profile measured in both the laminar regime (Re = 152) and also in the wake transition regime (Re = 183), and beyond the transition regime (Re = 520), at x/D = 30. (*b*) Spectra taken at points of maximum energy in the laminar regime (Re = 152) and in the transition regime (Re = 183).

This is an approximate indication that the instability wavelength for mode B ($\lambda_z \sim 4\delta_\omega$) is of the same order as one might expect based on the shear layer thickness. Nevertheless, a stability analysis for a shear layer in a strain rate field remains needed. We need here to predict the most unstable three-dimensional wavelength for a two-dimensional shear layer in a superposed two-dimensional strain rate field.

5. Wake measurements characterizing transition

In this section, we shall discuss velocity and pressure measurements made at various Reynolds numbers in the laminar shedding regime and through the wake transition regime. The fluctuation velocity profiles in figure 25(*a*) for the laminar regime (Re = 152) strongly contrast with those measured in the transition regime (Re = 183). The two side lobes for Re = 152 correspond to the two vortex rows moving downstream past the probe, whereas in wake transition not only is there far more

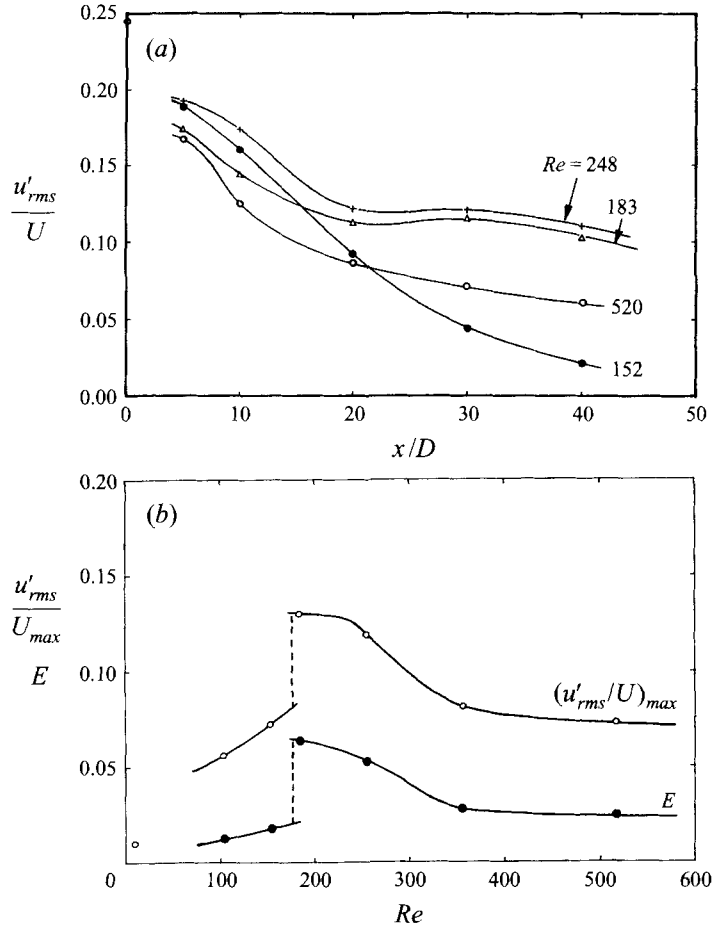

FIGURE 26. Downstream decay of wake velocity fluctuations and integrated energy, through wake transition. (*a*) Downstream decay of normalized rms velocity fluctuations, showing the distinctly different rates of decay in the laminar region (Re = 152) versus the transition regime (Re = 183, 248). The plateau region and slow decay are less pronounced outside transition (Re = 520). (*b*) Level of velocity fluctuations and integrated energy (E) across the wake at x/D = 30, for various Re through wake transition. The large level of fluctuations is particularly evident within the wake transition regime (Re = 190–250).

turbulence intensity at 30 diameters downstream (x/D = 30), but there is only a single large peak in the centre of the profile. This characteristic profile remains beyond the transition regime, as indicated by the case for Re = 520. Corresponding with these profiles, the spectra taken at the maxima in the profiles are radically different, as seen in figure 25(*b*). At Re = 152, the periodic spectra correspond to the translation of a laminar periodic vortex array past the probe, and the peaks are at the Kármán vortex frequency and their harmonics only. For the turbulent case for Re = 183 we have a much broader spectrum, with low energy remaining at the Kármán frequency. There is a surprisingly large amount of energy spread in a broad peak at the lowest frequencies, which far exceeds the energy for the laminar periodic wake.

The development of fluctuation level as one travels downstream, in figure 26(*a*), shows that in the middle of the wake transition regime ($Re \approx 240$), there is even a slight increase in fluctuation level between x/D = 20 and 30. This increase, or plateau, contrasts strongly with the exponential decay of fluctuations for the laminar wake at

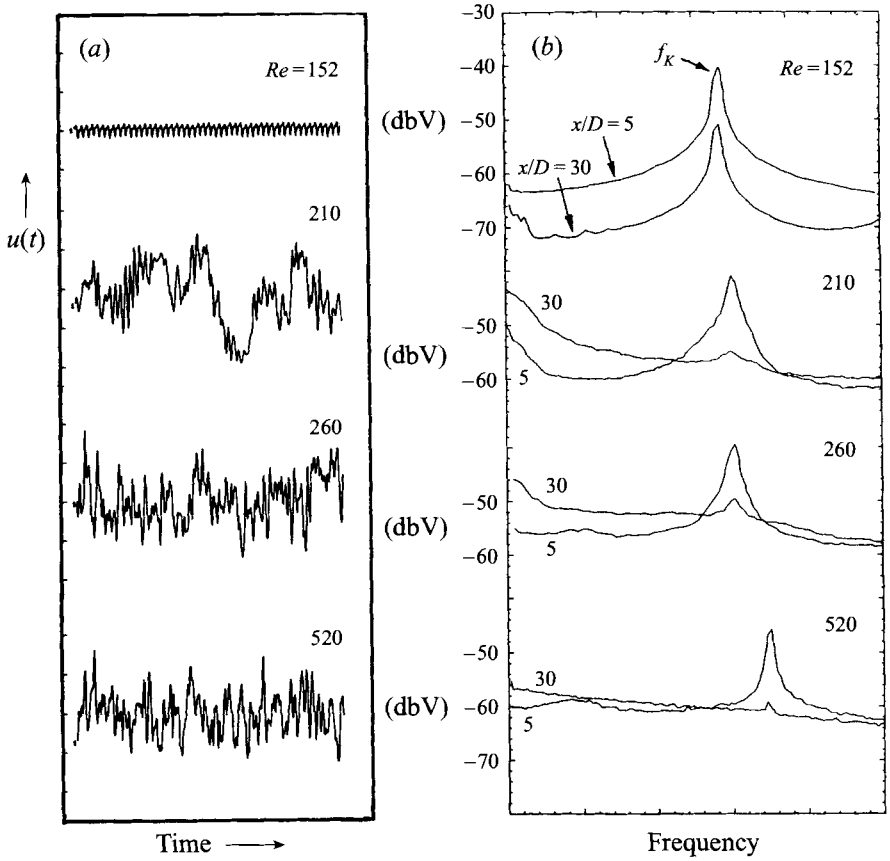

FIGURE 27. Large low-frequency fluctuations and corresponding spectra, through the transition regime. (*a*) Low-frequency intermittent velocity fluctuations in the transition regime explain the large fluctuation energy measured in the profile and downstream decay plots of figure 26. (*b*) Spectra at $x/D = 5$ and 30 for a selection of Re show the dominance of energy at low frequencies through transition, although by $Re = 520$, the broad low-frequency peak has diminished.

$Re = 152$. The slow decay of integrated energy across the wake profile (denoted E), shown in figure 26(*b*), is most evident in the wake transition regime around $Re = 190$–250, and the effect diminishes as Re increases outside this regime. Thus the transition regime is characterized by a surprisingly large level of low-frequency irregular fluctuations and a slow decay of turbulent energy, as one travels downstream.

The time traces of velocity fluctuation at $x/D = 30$ are particularly striking: figure 27 shows the relatively enormous low-frequency fluctuations at $Re = 210$ compared to the decayed laminar high-frequency fluctuations at $Re = 152$. Again, these large irregular fluctuations diminish in intensity as Re increases to 520, away from transition. Spectra at $x/D = 5$ and 30 are also shown for various Re, in figure 27, indicating the decay of fluctuations at the Kármán frequency when there is laminar shedding, although in the transition regime, the Kármán peak is rapidly lost in the noise by $x/D = 30$. The low-frequency component in the spectra at $x/D = 30$ reaches a maximum in the wake transition regime, but it is not apparent at higher Re, as shown for $Re = 520$.

The character of the above measurements through wake transition are largely influenced by the rapid loss of energy at the Kármán frequency, and a growth of fluctuations at low irregular frequencies. These low-frequency irregularities were

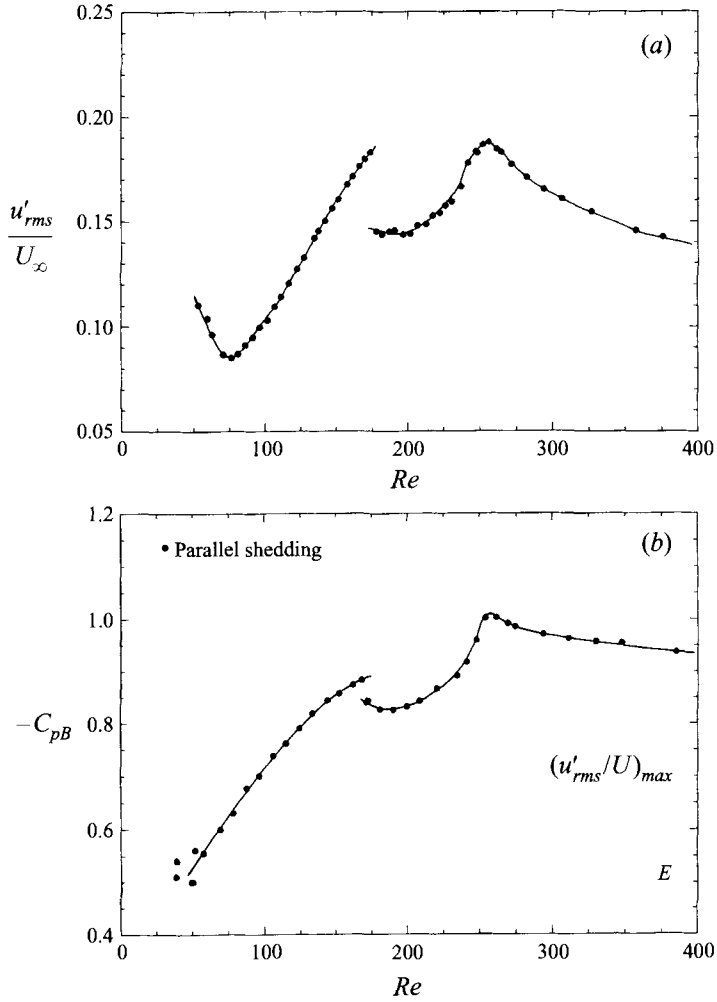

FIGURE 28. Striking similarities in variation of (u'_{rms}/U) and base suction $(-C_{pB})$, through the wake transition regime. (*a*) Velocity fluctuations (u'_{rms}/U) measured at $x/D = 10$, $y/D = 1.5$, as a function of *Re*. (*b*) Base suction coefficient $(-C_{pB})$ as a function of *Re*. Both of these wake parameters vary consistently with each other. One would expect the level of velocity fluctuations to be some measure of the near-wake Reynolds stresses, which would approximately be balanced by the level of base suction, in order that the forces acting on the mean recirculation region of the near wake are in equilibrium.

detected originally by Roshko (1954) and by Bloor (1964), and they are explained in Williamson (1992) as being due to the generation of intermittent vortex dislocations. A further brief discussion of large-scale vortex dislocations in natural wake transition will be given in §7.

The wake transition regime may be characterized also by mean wake parameters as one varies the Reynolds number. In figure 28, there appears to be a striking accordance between the shapes of the fluctuation level (u'_{rms}/U) and the base suction coefficient (the negative of the base pressure coefficient, or $-C_{pB}$), as *Re* is varied through transition. The level of (u'_{rms}/U) at a point in the near wake is an indication of the level of stress in the near wake. As the stress (and in particular the shear stress) in the formation region increases, and the mean wake recirculation bubble becomes smaller,

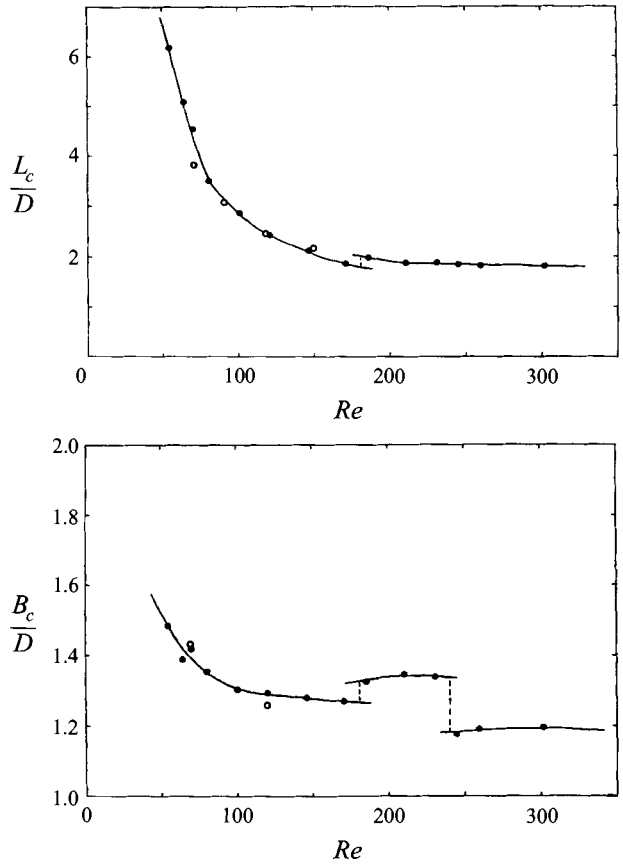

FIGURE 29. Variation of the location (L_C, B_C) of the characteristic point as a function of Re, exhibiting distinct changes for the different shedding modes in wake transition.

this is balanced by an increase in the base suction (see discussion in Roshko 1993, and in Williamson 1996*a*). Thus the curves in figures 28 are very similar in shape: each shows a drop as laminar shedding becomes unstable to mode-A instability and to dislocations. To some extent, the coherence and spanwise correlation of the shedding is reduced by the three-dimensionality, and the (two-dimensional) stresses are reduced, at this point. There is a remarkable peak in the stress and base suction at $Re = 260$, which corresponds to a strongly periodic spanwise instability of mode B, and a particularly ordered primary shedding. The reduction of two-dimensional stress and base suction after $Re = 260$ ensues as the small-scale three-dimensionality becomes more disordered.

Further extensive measurements of (u'_{rms}/U) have been made at each Re, and plotted in the form of contours in the near wake (Williamson 1987 and 1995 as yet unpublished work). There is a point on each side of the wake where (u'_{rms}/U) has reached a maximum. The location of this maximum is defined here as the 'characteristic' point, for a particular Re, with downstream distance to this point defined by L_C, and transverse coordinate as $\pm B_C/2$. Levels of characteristic $(u'_{rms}/U)_{MAX}$, and its correlation with several wake parameters are the subject of further work of the author. We can see that wake transition does influence the characteristic length (L_C) and width (B_C) in figure 29, causing an increase of both dimensions when mode-A instability appears. Essentially the near-wake formation region (or 'bubble') expands as the two-

dimensional stresses decrease, due to inception of three-dimensionality. As mode B appears at around $Re = 250$, there is a sharp decrease in wake width, which possibly corresponds with a decrease in the presence of dislocations, though this is not yet explained precisely.

6. A 'resonance' in the near wake for $Re = 260$

At this point in the presentation of results for the wake transition regime, it must be very apparent that the Reynolds number of 260 does represent a critical condition. At this Re, the wake oscillations are particularly periodic, with sharp-peaked spectra, in just the same manner as found in the laminar region. Examples of spectra and time traces of the velocity (the case without dislocations in this figure) are given in figure 30, under conditions of parallel shedding, where it can be seen that their appearance is close to that for a laminar regime case. In summary, the case $Re = 260$ seems critical for the following reasons:

the spanwise instability mode B is particularly periodic;
the primary vortex shedding is particularly ordered, and appears visually similar to the laminar regime, with the exception of the fine-scale three-dimensionality;
the velocity fluctuations are particularly periodic, with sharp-peaked spectra;
there is a maximum in the fluctuations (u'_{rms}/U);
there is a maximum in base suction $(-C_{pB})$.

All of these variations at $Re = 260$, particularly the maxima seen in (u'_{rms}/U) and base suction $(-C_{pB})$, suggest that there is possibly some form of resonance at this Reynolds number. It is conceivable that this is a manifestation of a resonance between the shear layer oscillations (frequency f_{SL}) and the wake oscillations (frequency f_K), where the relevant frequencies are coincident:

$$f_{SL} = f_K. \tag{28}$$

Arguments put forward by Bloor (1964) suggested that the separating shear layer instability frequency would scale as

$$f_{SL}/f_K \sim Re^{1/2}. \tag{29}$$

However, it happens that data from almost all previous investigations are not close to this 'law', despite the fact that most of them have fitted their data to a 1/2-power law. By replotting all of the available frequency data for the shear layer (including data up to the highest investigated, $Re = 100000$), Prasad & Williamson (1996, 1997*a*) have computed a much closer collapse of the frequency data, using the following relationship:

$$f_{SL}/f_K = 0.0234Re^{0.674}, \tag{30}$$

as shown in figure 31. There are reasons, discussed in Prasad & Williamson, why one should expect an exponent greater than 1/2.

For frequency ratios (f_{SL}/f_K) just greater than unity, one would not expect a two-frequency interaction, because one would not be able to fit a shear layer instability of the relevant wavelength within the streamwise extent of the vortex formation region before the vorticity becomes part of the fully formed shed wake. In fact, the first manifestation of shear layer instability is detected by probes at around $Re = 1200$ and for a ratio (f_{SL}/f_K) around 3. However, if the frequencies are coincident (or synchronized) then it is conceivable that the shedding instability in the near wake will be particularly strong. It is worth mentioning that this suggestion was made after the expression for frequencies (22) was computed. One can find that the Reynolds number

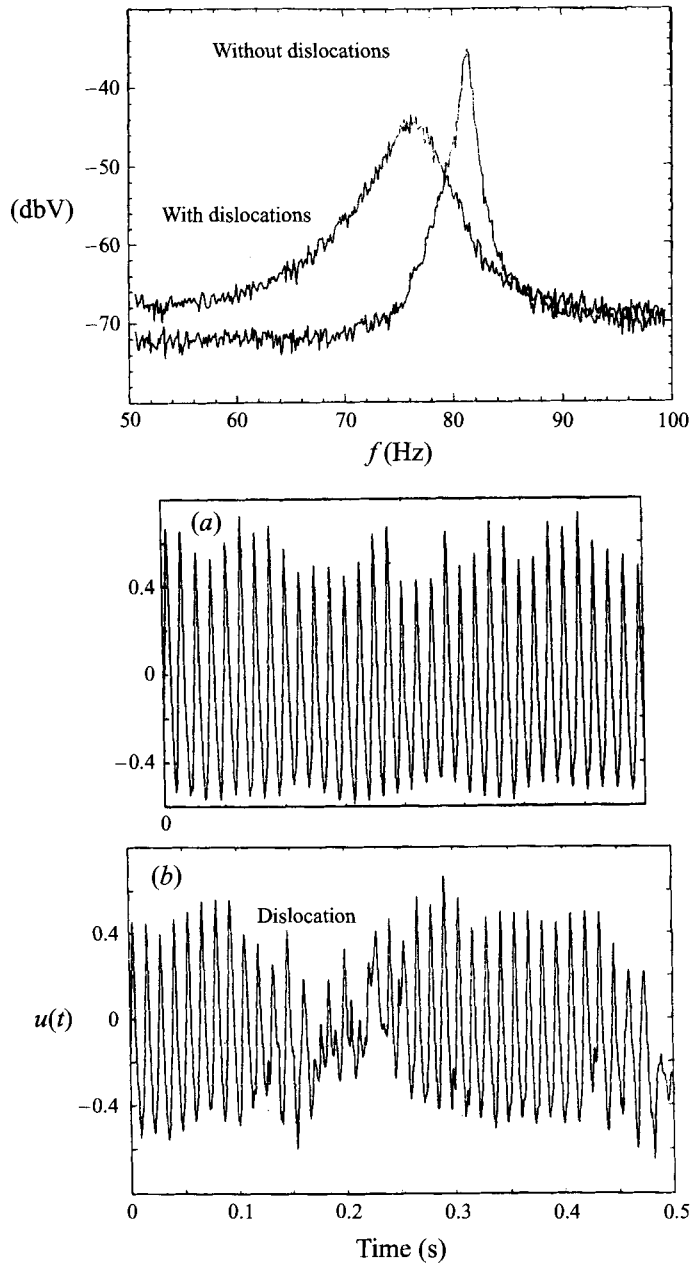

FIGURE 30. Spectra and velocity fluctuations at $Re = 260$. These spectra demonstrate the effects due to the presence of dislocations in broadening the spectra, and in reducing the shedding frequency. The time trace without dislocations (*a*) is remarkably periodic, and very similar to such fluctuations found in the laminar regime, while the time trace in (*b*) indicates clearly the presence of dislocations. Hot wire at $x/D = 10$, $y/D = 1.3$.

at which $f_{SL}/f_K = 1.0$ is given as $Re = 262$, which is essentially just where one finds the maxima in stress and base suction, and the other critical conditions mentioned above. It appears conceivable that the resonant conditions found at $Re = 260$ are caused by an interaction between two coincident frequencies in the near wake: namely the separating shear layer frequency and the bluff-body wake frequency.

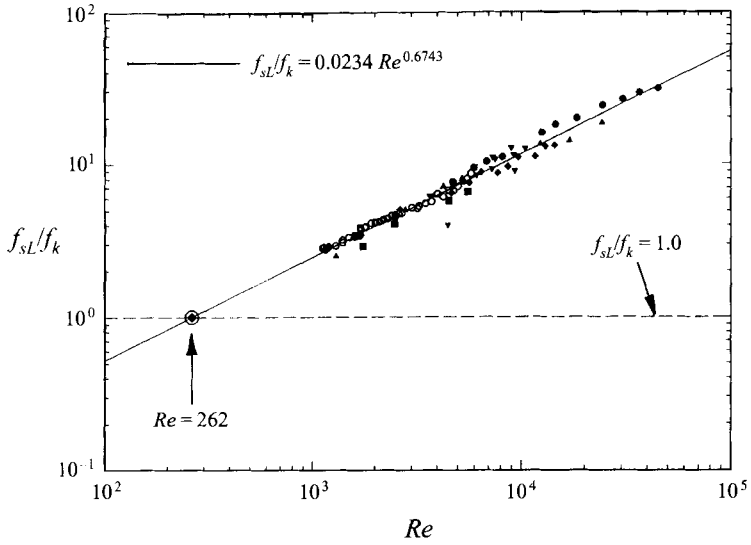

FIGURE 31. Coincidence between extrapolated shear layer frequency (f_{sL}) and Kármán frequency (f_K) at $Re = 260$, where there is an apparent resonance. The best-fit to all previous shear layer frequency measurements is not given by a $Re^{1/2}$ power as generally assumed, but rather by an expression involving a $Re^{0.67}$ power (Prasad & Williamson 1996). In this figure, we have extrapolated this expression down to the point where $f_{sL} = f_K$, yielding the value of $Re = 262$. This marks precisely the point where there are distinct maxima in stress level and base suction, evident in figure 28, and represents what we have termed a 'resonance' of the flow. [See Prasad & Williamson for references corresponding to the data symbols.]

Despite the above possible scenario to explain the resonance, one may also suggest that $Re = 260$ represents the Reynolds number at which mode B becomes linearly unstable, as found from the recent analysis of Barkley & Henderson (1996), and where we may perhaps expect the most periodic form of the streamwise vortex structure to appear, and this point is discussed further in §9.

7. Vortex dislocations: fundamental large-scale structure in wake transition

The existence of large-scale vortex dislocations, or in other words 'phase dislocations' of the primary vortex shedding, as a fundamental aspect of wake transition, was discovered in Williamson (1992). Their existence in wake transition explains the low-frequency irregular fluctuations originally reported by Roshko (1994) and later by Bloor (1964). In Williamson (1992), it was shown that forced 'two-sided' dislocations and naturally occurring dislocations in wake transition had distinct similarities, one of which was the large low-frequency fluctuations found further downstream, responsible for most of the energy in the velocity spectrum. Two-sided dislocations occur at a local spanwise location where the shedding falls out-of-phase with the shedding to each of the two sides, hence the terminology 'two-sided'. This contrasts with 'one-sided' dislocations which occur between spanwise cells of different frequency, and can be associated with the end conditions. The main point about two-sided structures in wake transition is that they occur independently of the ends, in an intermittent fashion. However, it has not been made clear before where these naturally occurring dislocations are triggered along the span, or what is their symmetry with respect to the wake centreplane, in the transition regime.

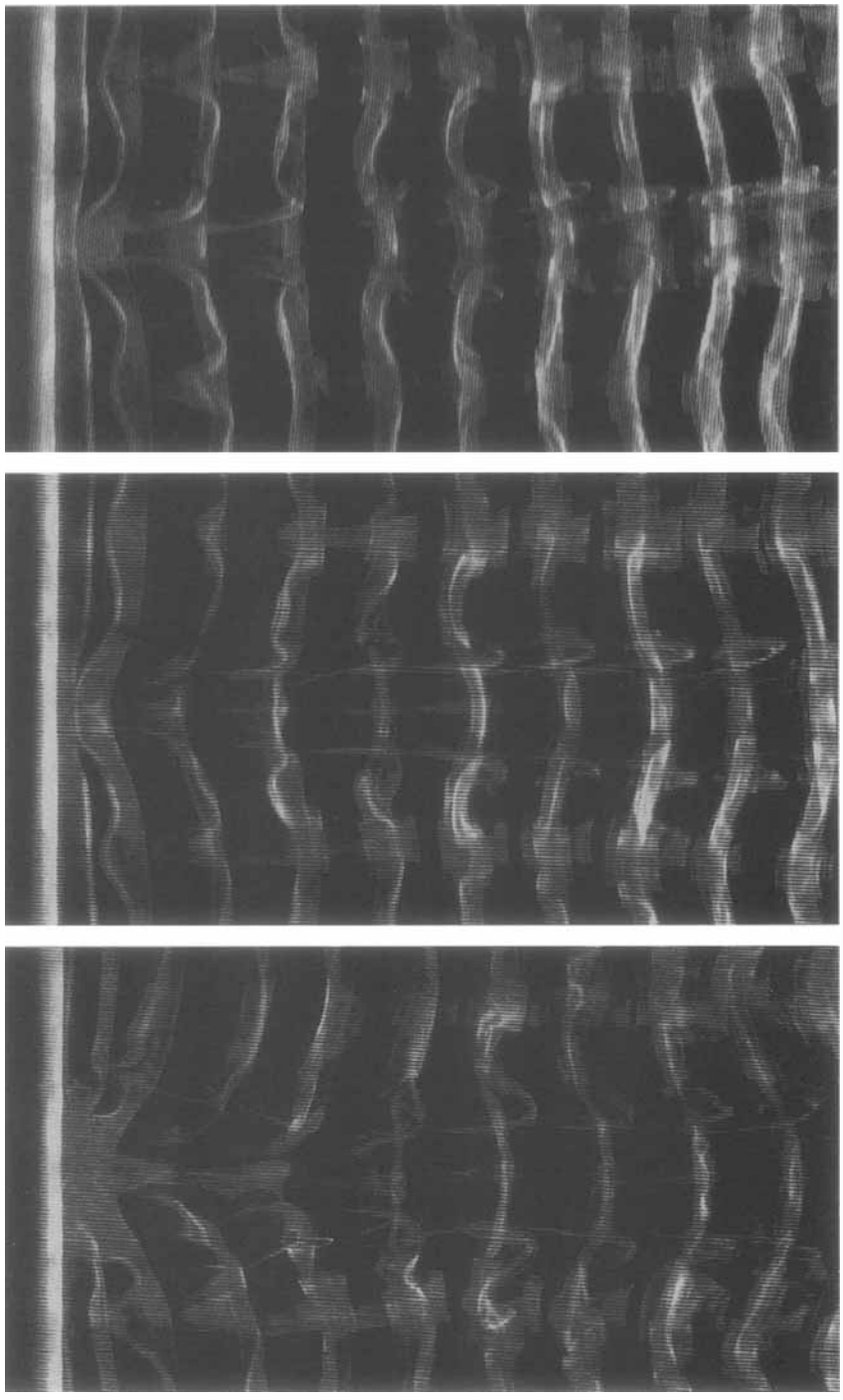

FIGURE 32. Evolution of a vortex dislocation at the site of a vortex loop of mode A: breakdown of spanwise periodicity for mode A instability. These are the two-sided dislocations that were forced to occur in the case of Williamson (1992), but it is clear that in the case of wake transition, they can form independently of the end conditions.

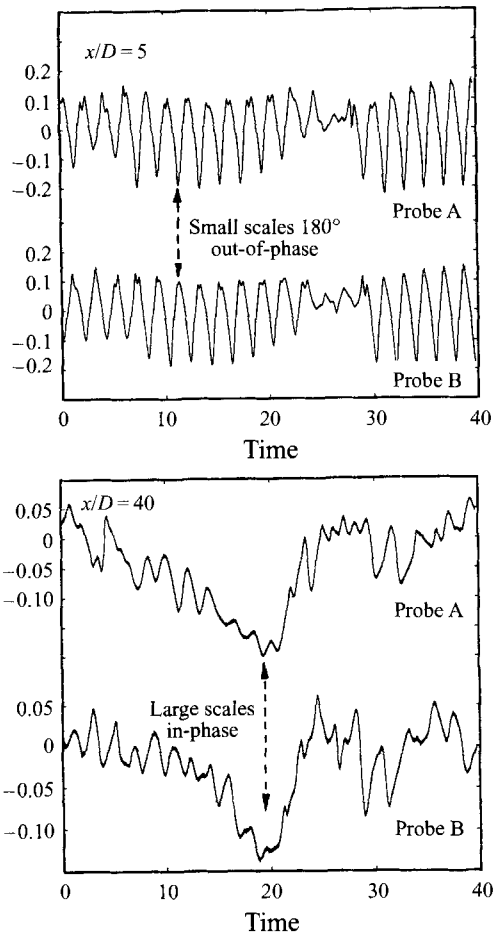

FIGURE 33. Transverse symmetry (across the wake centreplane) of a vortex dislocation. Placement of two hot wires, exactly opposite each other on two sides ($\pm y$) of the wake centreplane, shows that although the high-frequency Kármán vortex fluctuations are out-of-phase, the low-frequency irregularities, indicative of dislocations, are in-phase. The conclusion is that the large-scale dislocations are symmetric with respect to the centreplane, which is perhaps not unexpected.

From extensive visualizations of these two-sided dislocations, it has become clear that they are triggered at the sites of the vortex loops of mode-A instability, as indicated on the sequence of photographs of figure 32. One can interpret a vortex loop of this mode A as being a segment of the primary vortex whose shedding is delayed relative to the main part of the vortex. If such a loop grows, from one primary structure to the next, it can lead to the complete primary vortex locally shedding later than the rest of the primary vortex to each spanwise side, and we then have a phase or vortex dislocation. This is essentially what is shown in the visualization sequence in figure 32. There is a tendency for a single loop, within a spanwise row of vortex loops, to grow, inhibiting the formation of other dislocations to each side. This leads to a certain density of dislocations within the wake, which is comparable to the 'vortex defect' density found in mixing layers by Browand & Prost-Domasky (1990).

One might question the symmetry of these large-scale structures with respect to the wake centreplane: are they antisymmetric or symmetric when viewing in the spanwise direction? Hot-wire probe measurements have answered this question, as follows. Two

probes were placed opposite each other on each side of the wake ($\pm y$). Near the body, at $x/D = 5$, the Kármán-frequency velocity fluctuations are clearly in antiphase in figure 33, although the effect of the glitches, shown to represent phase dislocations in Williamson (1992), are in-phase across the wake. If one places the two probes downstream at $x/D = 40$, then it is clear that the large-scale structures are in-phase, even though the remnants of the small-scale (Kármán vortex) structures remain out-of-phase. One can conclude that the large-scale structures, or vortex dislocations, are of a symmetric form in wake transition. This appears to be consistent with theoretical statements in Yang, Mansy & Williams (1993), who state that the dislocations must be symmetric if the Kármán street is antisymmetric.

8. The 'stable' and 'unstable' flow states through wake transition

As may be suggested from the frequency measurements of figure 1, the effect of these dislocations is to decrease the Strouhal number. With the transition to mode-A instability and, perhaps more relevant here, the inception of dislocations, the vortex formation region grows in size as shown by the characteristic dimensions of figure 29, the base suction decreases, and the turbulence intensity in the near wake (and hence the stresses) decreases. These variations are consistent with the reduction of spanwise coherence of the primary vortex shedding when dislocations appear; the three-dimensionality will decrease the two-dimensional stresses. The growth of the near-wake dimensions is consistent with a reduction in vortex formation frequency, both of which are expected to have, very roughly, an inverse relationship.

It has proven possible, even for $Re = 260$ and above, to encourage or inhibit the presence of dislocations, by suitable manipulation of end conditions, as demonstrated in Prasad & Williamson (1997*b*) (over a range $Re = 260$–6000). The presence of dislocations tends to broaden the spectra, and to produce a lower peak intensity and a lower frequency, as shown by figure 30. The corresponding time trace of velocity fluctuations (*b*) indicates the presence of dislocations, in contrast to the periodic time trace (*a*) without the dislocations but at the same $Re = 260$. It is most significant that, where dislocations are imposed by end conditions in figure 34(*a*), the curve of Strouhal number is a simple continuation of the curve for the mode-A instability (also with dislocations). In fact, by imposing dislocations up to around $Re = 400$, the lower-frequency curve is further extended. If this lower curve represents (mode B + dislocations), then it suggests that the curve for mode A is more strictly the curve for (mode A + dislocations). This suggests a higher frequency could exist for purely mode A (in the absence of dislocations). The possibility of a higher-frequency curve (denoted mode C at that time) was discussed when the modes A and B were originally found in Williamson (1988*b*).

Of direct relevance to our discussion here, Zhang *et al.* (1995) proposed that the first discontinuity and hysteresis, associated with the onset of three-dimensionality in experiment, and representing a 'hard' transition, can be replaced in numerical simulations by a 'soft' transition. The three-dimensional flow state for this 'soft' transition causes the Strouhal curve in figure 34(*a*) to diverge gradually downwards from the two-dimensional case (although this point is not altogether as clear because their data are surprisingly high compared to all the other simulations compiled in the review of Williamson 1996*a*). However, Ron Henderson (personal communication, 1995) finds that dislocations do indeed appear in his three-dimensional simulations, and he has found Strouhal numbers close to the lower experimental curve. This fact, and further experimental evidence discussed above, has shown that the lower

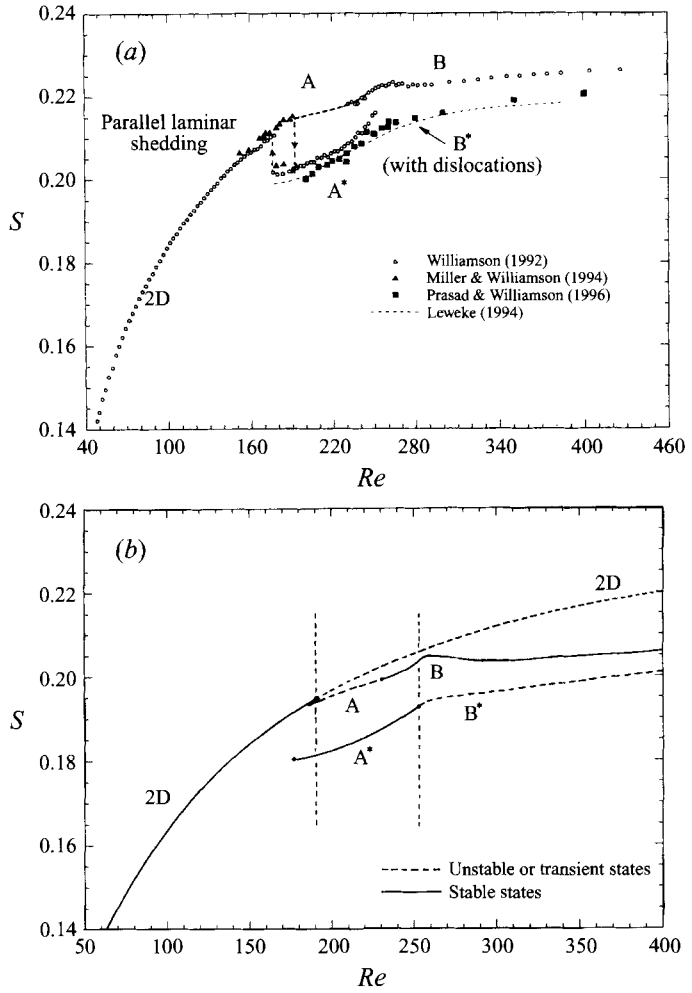

FIGURE 34. Stable and unstable states of the wake through the transition regime. (*a*) A new interpretation of the Strouhal curves; the upper curve corresponds to purely small-scale instabilities (e.g. A, B); the lower curve corresponds to these instabilities combined with intermittent vortex dislocations (e.g. A*, B*). The natural wake transition follows the sequence (2D → A* → B), although more probably a further state occurs, such that we have: (2D → A → A* → B). (*b*) The curves from the above data are drawn alone, for clarity, including the two-dimensional data from DNS of Barkley & Henderson 1996).

experimental curve (indicating the presence of dislocations) is a steady solution for the flow, and the upper three-dimensional curve from Zhang *et al.* (before dislocations appear) can be interpreted as a transient case.

In this section, the recent results of Leweke & Provansal (1995) must be mentioned, although in fact their problem comprises the flow normal to a ring cylinder (or torus). This represents, for large aspect ratio, the case of a cylinder with no physical ends, but can be thought of as a flow with periodic boundary conditions, just as in many of the DNS simulations. Leweke & Provansal find a distinct difference between the ring wake and the straight cylinder wake, in that they do not detect a second discontinuity separating mode A from mode B, and instead find a continuous curve as shown in figure 34(*a*). This they believe is the valid form for a wake without ends, and the second

discontinuity is an artifact of the straight-cylinder end effects. However, it now seems apparent that just the inverse of this statement is true. It happens that their curve in figure 34(*a*) is almost precisely the Strouhal curve that one finds for mode B, for a straight cylinder, when one induces vortex dislocations along the span (Prasad & Williamson 1997*b*), and suggests that for the torus, in this regime, the requirement of periodic end conditions cannot easily be met without dislocations being generated. This suggestion is supported by their measurements of a very low circumferential wake correlation close to $Re = 260$, which would also suggest dislocations. It is also found that DNS computations, where dislocations are present, give Strouhal numbers along the mode-A curve (R. Henderson, personal communication; see figure 11(*a*) in Williamson 1996*a*), whereas DNS computations without dislocations at $Re = 300$ place the Strouhal numbers very close to the experimental (upper) mode-B curve, in line with the straight-cylinder experiments. This appears to suggest again that the second discontinuity is an intrinsic phenomenon representing the wake of an infinitely long body, and not simply some artifact of the end conditions.

The investigations of the transition regime above lead us now to a new clarification of the possible flow states or modes through transition, as represented by the *S*–*Re* plot in figure 34(*b*). In this plot, the dashed curves are for flow states that are either unstable, or are transient, in the sense that such states can occur early in a DNS or experimental run, but will later evolve to a different more-stable flow state. When the flow exceeds a critical *Re*, the flow mode can follow a transition corresponding to mode-A instability small-scale structure, without dislocations. At some point in time after the start of the flow, when dislocations develop at some of the vortex loop 'sites' of mode A, then the flow will revert to a state A*, comprising a mix of both mode A structures and dislocations. At around $Re = 230$ up to 250, there are intermittent periods when there are predominantly small-scale instability structures across the span (a mix of A and B structures but without dislocations), yielding the upper frequency curve (B), and periods when the flow is principally mode A structures, but with dislocations, yielding the lower frequency curve (A*). Beyond $Re = 250$, the flow remains in the flow state of mode B, without dislocations, unless such dislocations are artificially introduced (Prasad & Williamson 1997*b*), in which case one follows the curve marked B*. This is a continuous extension of A*.

Thus there are two distinct Strouhal curves in figure 34(*b*): the upper one corresponds to the small-scale instabilities alone, and the lower one to a combination of the small-scale instabilities plus dislocations present. The natural transitioning wake will, however, pass from one flow state to another in the sequence

$$(2D \rightarrow A^* \rightarrow B).$$

There does remain the likely possibility that there exists a very small range of *Re* for which the flow is unstable to small scales of mode A, but whose amplitude is too weak to trigger intermittent vortex dislocations. This would be consistent with the result of Barkley & Henderson (1996), which predicts mode-A instability at $Re = 189$, which is earlier than the value of $Re = 194$ where experiment shows a distinct drop in frequency, indicative of dislocations (Miller & Williamson 1994). The above scenario yields the sequence

$$(2D \rightarrow A \rightarrow A^* \rightarrow B).$$

In the above sequence, natural wake transition comprises two discontinuous changes as *Re* is increased, with a hysteresis at the first discontinuity. Although there are two conceivable flow states at any particular *Re* through wake transition, it is clear that

some states are 'unstable' or transient, while others are 'stable'. This conclusion is consistent with the final statement in Williamson (1988*b*), where an upper curve for mode A was indicated, although the lower curve was proposed as a more stable route in the transition to three-dimensionality.

9. Discussion

The present work has indicated how streamwise vortex stretching, in the manner found in mixing layers, is an essential ingredient for the generation of streamwise vorticity in both modes A and B. An explanation for the symmetries of the two modes is based on two different mechanisms of instability: one is based on the core instability while the other involves instability of the braid shear layers. However, there exists an alternative view. Koenig, Noack & Eckelmann (B. N. Noack, personal communication, 1995) believe that the streamwise structures are a manifestation of 'Gortler' vortices, and have suggested from simulation that supercritical Taylor numbers exist near the braid regions in the wake, with some analogy to Taylor–Couette flows, and they suggest that this fact supports centrifugal instability as the origin for streamwise vortices. Such an idea was also proposed for the origin of streamwise vortices in the mixing layer, prior to the three pioneering papers of Corcos & Lin (see 1984), and the experimental work of Bernal & Roshko (1986), who focused on the stretching mechanism near the saddle points in the braid shear layers. The results in the present paper neither discount nor support the possibility for a centrifugal instability, at the present time.

The approach to the bluff-body wake problem from direct numerical simulation has received a great deal of attention recently. Not only are the mean parameters, such as Strouhal number, drag force, base pressure, stresses in the wake, well predicted, but the simulations provide a tool to understand the physics of the flow. The agreement among the computations and with the experiments is now remarkably good for the Strouhal number and base suction coefficient (see Williamson 1996*a*). Three-dimensional DNS of wake transition have confirmed, recently for the first time, the existence of both modes A and B in computations (Thompson *et al.* 1994, 1996; Zhang *et al.* 1995; B. N. Noack 1995, personal communications). The distinctly larger and smaller wavelengths of modes A and B (respectively) can clearly be observed in the striking surface-contour plots from Thompson *et al.* (1994), also reproduced in the review of Williamson (1996*a*). Mittal & Balachandar (1995*a*, *c*) have also found results from their DNS computations consistent with the present work, although the short cylinder span in their case precludes confirmation of patterns such as modes A and B. They make the point that previously formed streamwise vorticity affects the formation of new streamwise structures. They conclude that streamwise vortices are due both to the deformation of primary vortices during shedding and also the subsequent stretching in the braids. They show that the vorticity that is not taken upstream in the form of loops forms horseshoe-type structures on the primary vortex. All three of these conclusions are in direct accordance with the present work, and with the preliminary or overview studies of Williamson (1988*b*, 1992).

Mittal & Balachandar (1996) have very recently proposed a related mechanism which they call 'autogeneration' of streamwise vortices, from a numerical simulation of the cylinder wake at $Re = 300$. A new set of streamwise vortices is autogenerated as a result of the presence of an older set of vortices in the near wake. Mittal & Balachandar go on to suggest that it is the spanwise distortion of the primary spanwise vortices (by the streamwise vortices), in particular causing an entrainment of vorticity

from the 'neck' region (a region 'which connects the rolled-up spanwise vortex with the shear layer'), that plays a 'crucial' role in the autogeneration process, since this results in a distortion of the stretching field, which in turn has a direct influence on the growth rate and location of the new vortices. The essential difference between this mechanism and the present mode-B generation of new streamwise vortices is that in the present case there is a direct and clear perturbation from the old braid vortices onto the new ones, whereas the autogeneration system is indirect: the old streamwise vortices generate an undulation in the primary vortices, which in turn somehow distort the stretching of the new braid. Although this is different and clearly a much more complex scenario than is experimentally observed for mode B, it does seem that the general concept that an old set of streamwise vortices will influence a new generation of vortices is consistent with the present work, indeed for both present modes. Mittal & Balachandar also state that, because the bluff-body flow has a 'strong spatial development', the instability cannot be explained on the basis of a core or braid instability alone.

A further new mode-C three-dimensional instability has been proposed by Zhang *et al.* (1995), for $Re = 170$–270, based on the approximate stability analysis of Noack & Eckelmann (1994). In their analysis, Noack & Eckelmann find a spanwise wavelength of instability of $\lambda_z/D = 1.8$, which is also observed in the experiments and simulations of Zhang *et al.* However, this mode has surprisingly not been detected in any of the other experimental, numerical or analytical studies to date (including the present). It is of direct relevance to the possible existence of such a mode that, in the full Floquet stability analysis of Barkley & Henderson (1996), using 10000 modes in their analysis, they state that they find no unstable wavenumbers outside the neutral stability curve of figure 9(*b*), and they find $\lambda_z/D = 1.8$ to be a stable wavelength at these Re. Further results to support a mode C has been proposed by Zhang *et al.* in the form of DNS and experiments. From these studies, it appears that this mode C is the result of forcing on the nominally two-dimensional flow, in this case using an interference wire placed close to and parallel to the cylinder axis. Presumably, if one interferes with the two-dimensional flow field in other ways, one can induce still further three-dimensional instability wavelengths and modes. From the above deductions, it appears, at this point, that the natural wake comprises only the two distinct instabilities yielding modes A and B.

It should be mentioned that particle-image-velocimetry (PIV) techniques are now being applied to the wake problem in an effort to find vorticity and circulations in the streamwise vortices. Wu *et al.* (1994) have deduced the velocity and vorticity field of such vortices using PIV, and they compute the streamwise peak vorticity at $Re = 525$ to be $(\omega_x D/U) = 7$, which is larger than the peak spanwise vorticity of the Kármán vortices, $(\omega_x D/U) = 4.5$. On the other hand, the streamwise vortex circulations ($\Gamma_x/UD = 0.4$) are much smaller than the primary vortex circulations ($\Gamma_z/UD = 2.5$–3.5). Similar results have been found over a large range of Re at least up to 10000, as shown by the work of Lin *et al.* (1995*b*), and are consistent with data at $Re = 5000$ (Chyu & Rockwell 1996), although data are not at present at hand for the wake transition regime (the latter case is receiving attention currently from Helmut Eckelmann and co-workers). As one may expect, although streamwise vortex circulations are less than primary vortex circulations, the streamwise vorticity is axially stretched in the braid regions between the primary structures, causing strong vorticity amplification.

Finally, it must be stated that very recent results from Barkley & Henderson (1996) have demonstrated significant new results which are of direct relevance to the present

study. Their work has now shown that both modes A and B are secondary instabilities on the primary two-dimensional wake structure. (It seems particularly interesting to mention here the discovery of the second branch of instability in the plot of spanwise wavelength versus Re of figure 9, which shows mode B to become unstable at $Re = 259$. Not only are the wavelengths close to those previously measured in experiments ($\lambda \sim 1D$), but this critical Reynolds number is very close to the so-called 'resonance' of measured wake parameters at $Re = 260$ shown in the present §6. The fact that smaller wavelengths corresponding to mode B are found in experiment at $Re < 260$ seems related to the fact that the real flow, in the absence of mode B, is not two-dimensional, as used for the analysis in Barkley & Henderson, but is indeed already unstable to mode A with the complication of the presence of intermittent dislocations. It seems quite possible that the peak in measured parameters of figure 28, and the apparent resonance observed, is due to the start of this region of mode-B instability. The whole span becomes unstable to mode B, leading to the particularly ordered streamwise vortex structure, rather than simply spanwise patches of mode B for $Re < 260$, modified by mode A and dislocations.

It also appears highly consistent with the present work, that the analysis of Barkley & Henderson (1996, and personal communications) also demonstrates quite distinct regions in the cross-sectional flow field where the two instability modes are theoretically concentrated. Their figure 11 appears to show that mode A is concentrated around the primary vortex cores, while mode B is concentrated in the braid regions. This result is clearly consistent with the present study.

10. Conclusions

The wake transition regime ($Re = 190$–260) is characterized by two distinct three-dimensional modes of instability, as shown by Williamson (1988*b*). Mode-A instability has a spanwise wavelength of 3–4 diameters, whereas mode-B instability has a wavelength of close to 1 diameter. It is proven in the present work that both modes involve the generation of streamwise vortex pairs in the wake, which reside and are stretched in the streamwise direction in the braid regions, between primary Kármán vortex structures. Such stretching of streamwise vorticity is a well-known mechanism in free shear layers.

The marked disparity in spanwise wavelengths, and visual appearance, between modes A and B corresponds to the fact that the modes are due to two distinct instabilities. The two instabilities scale on the two principal physical features of the wake flow. The (long-wavelength) mode A scales on the larger physical feature in the wake flow, namely the primary vortex cores, and is shown to be due to an elliptic instability in these vortices. The nonlinear growth of vortex loops is due to the deformation or tearing of the primary vortices periodically along the span. The loop formation is self-sustaining at the same spanwise position, causing an out-of-phase symmetry for the streamwise vortex pattern of mode A. It appears that the realization that mode-A wake instability is indeed an elliptic flow instability of the near-wake vortex cores may represent the first clear manifestation of such an instability in a real open flow, although it does seem highly probable that it is generic to all shear flows, under conditions where the coherent vortex size exceeds the viscous cut-off scale.

The (short-wavelength) mode B, on the other hand, scales on the smaller physical length scale, namely the braid shear layer. If mode A represents an instability akin to that found for free shear layers (Bernal & Roshko 1986), with comparable lengthscales, then mode B is altogether a different instability, which is highly influenced by the

existence of the reverse flow region in the bluff-body wake. An essential feature for mode B is the fact that a forming braid shear layer lies in close proximity to a previously formed braid, which comprises an array of rolled-up streamwise vortices, and which is brought upstream by the reverse flow. The disturbances thus imposed on the forming braid sets the preferred locations of the new braid vortices, giving a specific symmetry quite distinct from mode A; mode B has an in-phase symmetry for the streamwise vortex pattern. This symmetry, and the mechanism of instability involving the braid saddle points, is analogous with Meiburg & Lasheras' mode 1 perturbed unseparated wake from a splitter plate with cross-stream corrugations. It should also be mentioned here that, subsequent to the growth of the new braid streamwise vortices, which are a repeat of the previous set of braid vortices, the like-sign vortices in each braid system appear to amalgamate into a single set of braid streamwise vortices.

It is known that the incipience of wake transition is triggered early by contamination in the form of vortex dislocations coming from the ends of the body (Miller & Williamson 1994). Over the last forty years a range of critical Reynolds number of $Re = 140$–190 has been reported. However, by minimizing any end contamination, one finds $Re_{crit} = 194$, which is remarkably close to the results from the recent Floquet stability analysis of Barkley & Henderson (1996), which finds $Re_{crit} = 189$. In the present paper, we find that the presence of interfering vortex dislocations (not caused by end effects) causes the large scatter in previous measurements of spanwise wavelength for the vortex loops of mode-A instability. It is only by careful and accurate measurements without the presence of dislocations, that one finds a clear trend of decreasing wavelength with Reynolds number, which is quite distinct from the assumptions of constant wavelength in previous studies. The present data yield an excellent agreement with the curve of maximum growth rate from the stability analysis of Barkley & Henderson.

The wake transition regime can also be characterized by velocity and pressure measurements, and the inception of the different modes of instability, along with the presence of dislocations yield discontinuities in the S–Re relationship, the first of which is hysteretic while the second involves a gradual transfer of energy from one mode of shedding to another. It is shown here that the presence of the dislocations has an important impact on the flow measurements: it causes a discontinuous reduction in Strouhal frequency and it induces large levels of turbulent fluctuations, which decay only slowly downstream. One might question from where these two-sided dislocations originate. We show here that they are triggered at the sites of vortex loops, and are not a manifestation of end effects or of experimental artifact. In other words, the periodicity of the mode-A instability itself seems to naturally break down into a much more irregular state, and thus should be considered in further modelling or simulation of this flow.

Further measurements indicate a remarkable similarity between the variations of base suction and the level of fluctuations (or Reynolds stress) through the wake transition, which may be understood if one considers the balance of forces on the mean recirculation region in the near wake. It is consistent that, when dislocations and mode-A instability appear, one finds a reduction of fluctuation level, a reduction of base suction, a growth in the size of wake formation region, and thereby a reduction in Strouhal frequency.

At the end of the transition regime, $Re = 260$, there appears to be a resonance condition, corresponding with a local maximum in base suction and Reynolds stresses, which is matched by a particularly ordered and periodic shedding. It does seem conceivable, based on extensive frequency measurements, that this resonance is caused

by an interaction between two coincident frequencies in the near wake, namely the separating shear layer frequency and the bluff-body wake frequency. It is also significant that $Re = 260$ corresponds closely to the inception of a secondary instability region for mode B, as shown very recently by Barkley & Henderson.

The present work leads us to a new clarification of the possible flow states through transition. Right through this regime there exist two distinct and continuous Strouhal frequency curves – the upper one corresponds with purely small-scale instabilities (e.g. denoted as mode A), while the lower curve corresponds with a combination of small-scale plus dislocation structures (e.g. mode A*). However, some of the flow states are transient or unstable, and the natural transitioning wake follows the scenario

$$(2D \rightarrow A^* \rightarrow B).$$

However, we must admit the possibility of a very small stable regime of mode A, before dislocations appear, causing the discontinuous jump $A \rightarrow A^*$:

$$(2D \rightarrow A \rightarrow A^* \rightarrow B).$$

Although this latter sequence seems probable, evidence is not yet at hand to prove this scenario of flow states.

The author would like to enthusiastically thank Anil Prasad for wholehearted help with this paper, and Thomas Leweke for exceedingly enjoyable communications regarding elliptic instability in this and other flows we study. Helene Persillon (Cornell) and Marianna Braza, as well as Karim Shariff, are to be thanked for making available 2-D DNS wake data. The author would also like to thank Gregory Miller and Chantal Champagne PhD for further assistance, and Patrick Huerre, Jean-Marc Chomaz, Maurice Rossi and Stephan Le Dizes for interesting discussions. Thanks are also due to the enthusiastic help of undergraduates Phil Peters and David Williams, who set up the LIF video arrangement for two of the figures. The support from the Ocean Engineering Division of the ONR, monitored by Tom Swean, is gratefully acknowledged. (ONR Contracts No. N00014-94-1-1197 and N00014-95-1-0332). It is thanks to the opportunities provided by Anatol Roshko of Caltech and to Eugene Silva of ONR that this particular piece of work was begun at Caltech back in 1985.

Note added in proof: Very recent work of Brede, Eckelmann & Rockwell (1996) has addressed the wake transition secondary vortex structure from PIV (particle-image-velocimetry) measurements. Their excellent use of this technique (developed in this case by Don Rockwell at Lehigh University) is directly relevant to the present results. They find topologies as follows. For the A-mode they describe the structure as 'vortex patches' or 'tongues', which are essentially the vortex loops found here and in Williamson (1988), whereas for the B-mode they interpret the flow as having 'continuous vortex tubes'. This is also consistent with the present work, if one interprets the succeeding sets of streamwise vortices as being somehow joined (a point which is not obvious). As regards instabilities, they propose certain speculations, as follows. For the A-mode, it is proposed that it is 'the result of an instability of the braid region between the primary vortices', which they suggest is a manifestation of a centrifugal instability. For the B-mode, they suggest that it has its origin in the three-dimensional instability of the separated shear layer right behind the body, without primary vortex interactions being important. Although the wake structure observations are similar to the present and previous studies, the proposition that A and B modes

have respectively a braid-centrifugal instability, and a shear layer instability, are clearly in marked contrast to the present conclusions.

REFERENCES

BARKLEY, D. & HENDERSON, R. D. 1996 Three-dimensional Floquet stability analysis of the wake of a circular cylinder. *J. Fluid Mech.* **322**, 215.

BAYLY, B. J. 1986 Three-dimensional instability of elliptical flow. *Phys. Rev. Lett.* **57**, 2160.

BAYS-MUCHMORE, B. & AHMED, A. 1993 On streamwise vortices in turbulent wakes of cylinders. *Phys. Fluids* A **5**, 387.

BELL, J. A. & MEHTA, R. D. 1989 Three-dimensional structure of a plane mixing layer. *AIAA Paper* 89-0124.

BERNAL, L. P. & ROSHKO, A. 1986 Streamwise vortex structure in plane mixing layers. *J. Fluid Mech.* **170**, 499.

BLOOR, M. S. 1964 The transition to turbulence in the wake of a circular cylinder. *J. Fluid Mech.* **19**, 290.

BRAZA, M. 1994 Transition features in wake flows by means of numerical analysis. *Current Topics in the Physics of Fluids*, **1**, 391.

BRAZA, M., CHASSAING, P. & HA MINH, H. 1990 Prediction of large-scale transition features in the wake of a circular cylinder. *Phys. Fluids* A **2**, 1461.

BREDE, M., ECKELMANN, H. & ROCKWELL, D. 1996 On secondary vortices in the cylinder wake. *Phys. Fluids* (submitted).

BROWN, G. L. & ROSHKO, A. 1974 On density effects and large structures in turbulent mixing layers. *J. Fluid Mech.* **64**, 775.

BROWAND, F. K. & PROST-DOMASKY, S. A. 1990 Experiment on pattern evolution in the 2-D mixing layer. In *New Trends in Nonlinear Dynamics and Pattern Forming Phenomena* (ed. P. Coullet & P. Huerre). NATO ASI Series 8. Plenum.

CANTWELL, B. & COLES, D. 1983 An experimental study of entrainment and transport in the turbulent near-wake of a circular cylinder. *J. Fluid Mech.* **136**, 321.

CHYU, C. & ROCKWELL, D. O. 1996 Evolution patterns of streamwise vorticity in the turbulent near wake of a cylinder. *J. Fluid Mech.* **320**, 117.

CORCOS, G. M. & LIN, S. J. 1984 The mixing layer: deterministic models of turbulent flow. Part 2. The origin of three-dimensional motion. *J. Fluid Mech.* **139**, 67.

CORKE, T., KOGA, D., DRUBKA, R. & NAGIB, H. 1977 A new technique for introducing controlled sheets of streaklines in wind tunnels. *IEEE Publication* 77-CH 1251-8 AES.

CRAIK, A. D. D. & CRIMINALE, W. O. 1986 Evolution of wavelike disturbances in shear flows: A class of exact solutions of the Navier–Stokes equations. *Proc. R. Soc. Lond.* A **406**, 13.

EISENLOHR, H. & ECKELMANN, H. 1989 Vortex splitting and its consequences in the vortex street wake of cylinders at low Reynolds number. *Phys. Fluids* A **1**, 189.

GERICH, D. & ECKELMANN, H. 1982 Influence of end plates and free ends on the shedding frequency of circular cylinders. *J. Fluid Mech.* **122**, 109.

GERRARD, J. H. 1978 The wakes of cylindrical bluff bodies at low Reynolds number. *Phil. Trans. R. Soc. Lond.* A **288**, 351.

HAMA, F. R. 1957 Three-dimensional vortex pattern behind a circular cylinder. *J. Aeronaut. Sci.* **24**, 156.

HAMA, F. R. 1963 Progressive deformation of a perturbed line vortex filament. *Phys. Fluids* **6**, 526.

HAMMACHE, M. & GHARIB, M. 1989 A novel method to promote parallel shedding in the wake of circular cylinders. *Phys. Fluids* A **1**, 1611.

HAMMACHE, M. & GHARIB, M. 1991 An experimental study of the parallel and oblique vortex shedding from circular cylinders. *J. Fluid Mech.* **232**, 567.

HENDERSON, R. D. 1994 Unstructured spectral element methods: Parallel algorithms and simulations. PhD. thesis, Princeton University.

HENDERSON, R. D. 1995 Details of the drag curve near the onset of vortex shedding. *Phys. Fluids* **7**, 2102.

HENDERSON, R. D. & BARKLEY, D. 1996 Secondary instability in the wake of a circular cylinder. *Phys. Fluids* **8**, 1683.

HO, C.-M. & HUERRE, P. 1984 Perturbed free shear layers. *Ann. Rev. Fluid Mech.* **16**, 365.

HUANG, L.-S. & HO, C.-M. 1990 Small-scale transition in a plane mixing layer. *J. Fluid Mech.* **210**, 475.

HUERRE, P. & ROSSI, M. 1996 *Hydrodynamic Instabilities in Open Flows*. Cambridge University Press.

KARNIADAKIS, G. E. & TRIANTAFYLLOU, G. S. 1989 Frequency selection and asymptotic states in laminar wakes. *J. Fluid Mech.* **199**, 441.

KARNIADAKIS, G. E. & TRIANTAFYLLOU, G. S. 1992 Three-dimensional dynamics and transition to turbulence in the wake of bluff objects. *J. Fluid Mech.* **238**, 1.

KELVIN, LORD 1880 Vibrations of a columnar vortex. *Phil. Mag.*, **X**, 155.

KOENIG, M., EISENLOHR, H. & ECKELMANN, H. 1990 The fine structure in the *S–Re* relationship of the laminar wake of a circular cylinder. *Phys. Fluids* A **2**, 1607.

KOENIG, M., EISENLOHR, H. & ECKELMANN, H. 1992 Visualisation of the spanwise cellular structure of the laminar wake of wall-bounded circular cylinders. *Phys. Fluids*, A **4**, 869.

KOURTA, A., BOISSON, H. C., CHASSAING, P. & HA MINH, H. 1987 Nonlinear interaction and the transition to turbulence in the wake of a circular cylinder. *J. Fluid Mech.* **181**, 141.

LAGNADO, R. R., PHAN-TIEN, N. & LEAL, L. G. 1984 The stability of two-dimensional linear flows. *Phys. Fluids* **27**, 1094.

LANDMAN, M. J. & SAFFMAN, P. G. 1987 The three-dimensional instability of strained vortices in a viscous fluid. *Phys. Fluids* **30**, 2339.

LASHERAS, J. C. & CHOI, H. 1988 Three-dimensional instability of a plane free shear layer; an experimental study of the formation and evolution of streamwise vortices. *J. Fluid Mech.* **189**, 53.

LASHERAS, J. C. & MEIBURG, E. 1990 Three-dimensional vorticity modes in the wake of a flat plate. *Phys. Fluids* A **2**, 371.

LEWEKE, T. & PROVANSAL, M. 1995 The flow behind rings: bluff body wakes without end effects. *J. Fluid Mech.* **288**, 265.

LEWEKE, T. & WILLIAMSON, C. H. K. 1996*a* Elliptic instability and three-dimensional transition in bluff body wakes. *Phys. Fluids* (submitted).

LEWEKE, T. & WILLIAMSON, C. H. K. 1996*b* Short wave instability of a vortex pair. *J. Fluid Mech.* (submitted).

LIN, J.-C., TOWFIGHI, J. & ROCKWELL, D. 1995*a* Instantaneous structure of near-wake of a cylinder: on the effect of Reynolds number. *J. Fluids Struct.* **9**, 409.

LIN, J.-C., VOROBIEFF, P. & ROCKWELL, D. 1995*b* Three-dimensional patterns of streamwise vorticity in the turbulent near-wake of a cylinder. *J. Fluids Struct.* **9**, 231.

MANSY, H., YANG, P. & WILLIAMS, D. R. 1994 Quantitative measurements of spanwise-periodic three-dimensional structures in the wake of a circular cylinder. *J. Fluid Mech.* **270**, 277.

MARTIN, J. E. & MEIBURG, E. 1991 Numerical investigation of three-dimensionally evolving jets subject to axisymmetric and azimuthal perturbations. *J. Fluid Mech.* **230**, 271.

MEIBURG, E. & LASHERAS, J. C. 1988 Experimental and numerical investigation of the three-dimensional transition in plane wakes. *J. Fluid Mech.* **190**, 1.

MILLER, G. D. & WILLIAMSON, C. H. K. 1994 Control of three-dimensional phase dynamics in a cylinder wake. *Exp. Fluids* **18**, 26.

MITTAL, R. & BALACHANDAR, S. 1995*a* Vortical structures in bluff body wakes. *AIAA 33rd Aerospace Sciences Meeting, Jan 9–12, Reno, Nevada, Paper* 95–0867.

MITTAL, R. & BALACHANDAR, S. 1995*b* Effect of three-dimensionality on the lift and drag of nominally two-dimensional cylinder. *Phys. Fluids* **7**, 1841.

MITTAL, R. & BALACHANDAR, S. 1995*c* Generation of streamwise vortical structures in bluff-body wakes. *Phys. Rev. Lett.* **75**, 1300.

MITTAL, R. & BALACHANDAR, S. 1996 Auto-generation of three-dimensional vortical structure in the near-wake of a circular cylinder. *J. Fluid Mech.* (submitted).

MONKEWITZ, P. A., WILLIAMSON, C. H. K. & MILLER, G. D. 1996 Phase dynamics of Kármán vortices in cylinder wakes. *Phys. Fluids* **8**, 91.

NOACK, B. N. & ECKELMANN, H. 1994 A global stability analysis of the steady and periodic cylinder wake. *J. Fluid Mech.* **270**, 297.

NORBERG, C. 1994 An experimental investigation of the flow around a circular cylinder: influence of aspect ratio. *J. Fluid Mech.* **258**, 287.

NYGAARD, K. J. & GLEZER, A. 1990 Core instability of the spanwise vortices in a plane mixing layer. *Phys. Fluids.* A **2**, 461.

PERSILLON, H. & BRAZA, M. 1996 Three-dimensional transition to turbulence in the cylinder wake by direct numerical simulation. *J. Fluid Mech.* (submitted).

PIERREHUMBERT, R. 1986 A universal short wave instability of two-dimensional eddies in an inviscid fluid. *Phys. Rev. Lett.* **57**, 2157.

PIERREHUMBERT, R. & WIDNALL, S. 1982 The two- and three-dimensional instabilities of a spatially periodic shear layer. *J. Fluid Mech.* **114**, 59.

PRASAD, A. & WILLIAMSON, C. H. K. 1997 The instability of the separated shear layer from a bluff body. *Phys. Fluids* **8**, 1347.

PRASAD, A. & WILLIAMSON, C. H. K. 1997*a* The instability of the shear layer separating from a bluff body. *J. Fluid Mech.* (In press).

PRASAD, A. & WILLIAMSON, C. H. K. 1997*b* Three-dimensional effects on turbulent bluff body wakes at moderate Reynolds numbers. *J. Fluid Mech.* (submitted).

ROGERS, M. M. & MOSER, R. D. 1992 The three-dimensional evolution of a plane mixing layer: the Kelvin–Helmholtz rollup. *J. Fluid Mech.* **243**, 183.

ROSHKO, A. 1954 On the development of turbulent wakes from vortex streets. *NACA Rep.* 1191.

ROSHKO, A. 1993 Perspectives on bluff body aerodynamics. *J. Wind Engng Indust. Aerodyn* **49**, 79.

SHARIFF, K., PULLIAM, T. H. & OTTINO, J. M. 1991 A dynamical systems analysis of kinematics in the time-periodic wake of a circular cylinder. In *Vortex Dynamics and Vortex Methods* (ed. C. R. Anderson & C. Greengard), p. 613. American Math. Soc.

STUART, J, T. 1967 On finite amplitude oscillations in laminar mixing layers. *J. Fluid Mech.* **29**, 417.

THOMANN, H. 1959 Measurements of the recovery temperature in the wake of a cylinder and of a wedge at Mach numbers between 0.5 and 3. *Aero Research Inst. Sweden (FFA) Rep.* 84.

THOMPSON, M., HOURIGAN, K. & SHERIDAN, J. 1994 Three-dimensional instabilities in the cylinder wake. *Intl Colloq. on Jets, Wakes and Shear Layers, Melbourne, 18–20 April, 1994.*

THOMPSON, M., HOURIGAN, K. & SHERIDAN, J. 1966 Three-dimensional instabilities in the wake of a circular cylinder. *Exp. Thermal Fluid Sci.* **12**, 190.

TRITTON, D. J. 1959 Experiments on the flow past a circular cylinder at low Reynolds numbers. *J. Fluid Mech.* **6**, 547.

TRITTON, D. J. 1988 *Physical Fluid Dynamics*, 2nd Edn. Clarendon.

WALEFFE, F. 1990 On the three-dimensional instability of strained vortices. *Phys. Fluids* A **2**, 76.

WEI, T. & SMITH, C. R. 1986 Secondary vortices in the wake of cylinders. *J. Fluid Mech.***169**, 513.

WILLIAMSON, C. H. K. 1987 Three-dimensional transition in the near wake of a cylinder. *Bull. Am. Phys. Soc.* **32**, 2098.

WILLIAMSON, C. H. K. 1988*a* Defining a universal and continuous Strouhal–Reynolds number relationship for the laminar vortex shedding of a circular cylinder. *Phys. Fluids* **31**, 2742.

WILLIAMSON, C. H. K. 1988*b* The existence of two stages in the transition to three-dimensionality of a cylinder wake. *Phys. Fluids* **31**, 3165.

WILLIAMSON, C. H. K. 1989 Oblique and parallel modes of vortex shedding in the wake of a circular cylinder at low Reynolds numbers. *J. Fluid Mech.* **206**, 579.

WILLIAMSON, C. H. K. 1992 The natural and forced formation of spot-like 'vortex dislocations' in the transition of a wake. *J. Fluid Mech.* **243**, 393.

WILLIAMSON, C. H. K. 1996*a* Vortex dynamics in the cylinder wake. *Ann. Rev. Fluid Mech.* **28**, 477.

WILLIAMSON, C. H. K. 1996*b* Mode A secondary instability in wake transition. *Phys. Fluids* **8**, 1680.

WILLIAMSON, C. H. K. & ROSHKO, A. 1990 Measurements of base pressure in the wake of a cylinder at low Reynolds numbers. *Z. Flugwiss Weltraumforsch.* **14**, 38–46.

WILLIAMSON, C. H. K., WU, J. & SHERIDAN, J. 1995 Scaling of streamwise vortices in wakes. *Phys. Fluids* **7**, 2307.

WU, J., SHERIDAN, J., SORIA, J. & WELSH, M. C. 1995 Longitudinal vortex structures in a cylinder wake. *J. Fluids Struct.* (submitted).

WU, J., SHERIDAN, J., WELSH, M. C., HOURIGAN, K. & THOMPSON, M. 1994 Longitudinal vortex structures in a cylinder wake. *Phys. Fluids* **6**, 2883.

YANG, P., MANSY, H. & WILLIAMS, D. R. 1993 Oblique and parallel wave interaction in the near wake of a circular cylinder. *Phys. Fluids* A **5**, 1657.

ZHANG, H., FEY, U., NOACK, B. R., KOENIG, M. & ECKELMANN, H. 1995 On the transition of the cylinder wake. *Phys. Fluids* **7**, 1.